

NORTHWESTERN UNIVERSITY

Materials and Models for Coexisting Metallic Conductivity and Broken Inversion Symmetry

A DISSERTATION

SUBMITTED TO THE GRADUATE SCHOOL

IN PARTIAL FULFILLMENT OF THE REQUIREMENTS

for the degree

DOCTOR OF PHILOSOPHY

Field of Materials Science and Engineering

by

Daniel Timothy Hickox-Young

EVANSTON, ILLINOIS

September 2021

Abstract

Metallic conductivity and broken inversion symmetry were long thought to be contraindicated properties, under the assumption that long-range Coulombic interactions (screened by free charge carriers) were necessary for coordinated polar displacements. Within the past decade, the discovery of polar metals has prompted a rethinking of the relationship between metallicity and inversion-lifting distortions, spurring new research on diverse materials. Recent work has revealed that polar metals are capable of hosting a wide variety of rare and desirable properties, ranging from unconventional superconductivity to enhanced thermopower. Nonetheless, there remains ambiguity regarding the fundamental relationship between the distortion mechanism and the electronic structure, due in part to the many different approaches to uniting the two orders. Thus, despite a large number of so-called “ferroelectric,” “ferroelectric-like,” and “polar” metals, band metals that exhibit an inversion-breaking distortion are still rare.

In this dissertation, I use first principles simulations to investigate the rich landscape of materials that combine long-range polar order with free charge carriers. The lack of clarity in this materials landscape limits our ability to maximize the potential technological impact of polar metals. Therefore, this work 1) classifies and categorizes the diverse methods of uniting broken inversion symmetry with metallic conductivity, 2) investigates the interplay between doped charge carriers and polar distortions, and 3) predicts a new class of polar metals. My efforts demonstrate that the fundamental relationship between conductivity and polar order depends on the materials class

and distortion mechanism, and provides guidelines for the design of polar metals in new materials classes.

Acknowledgements

I would like to begin by thanking my research advisor, James Rondinelli, for both structure and support during the past five years. James provided organization and direction when I needed it most, while also encouraging me to develop my own research and career interests. Above all else, I will value his guidance regarding the communication of science; be it in papers, presentations, or lectures. I know these and countless other interactions have made me a better researcher, mentor, and teacher.

I would also like to thank the members of the Materials Theory and Design group for their advice and companionship. Danilo Puggioni was an especially important mentor to me during my time in the group. He taught me to ask the questions that need to be asked and helped me through the sometimes painful process of improving many papers and presentations. At the same time, he also taught me to trust myself as a scientist and to have confidence in my results. Yongjin Shin, Jaye Harada, and Nicholas Wagner were generous with their time and resources, always willing to answer questions and sharing scripts, input files, and restaurant recommendations. Nathan Koocher was also a valuable mentor and friend, passing along insights into every aspect of life as a graduate student. Richard Saballos was an important friend and colleague, sharing companionship, perspective, and engaging conversation both inside and outside the office. I would also like to thank Nenian Charles, Mingqiang (Kurt) Gu, Liang-Feng Huang, Xuezheng Lu, Mike Waters, Yiqun (Raymond) Wang, Lauren Walters, Kyle Miller, Kathleen Mullin, Alexandru Georgescu, and Sean Koyama for their comraderie and insights.

I am also grateful to have had influential mentors from outside Northwestern. I would like to thank Brian Borovsky for first introducing me to materials science as an undergraduate and continuing to support me in my graduate career ever since. I would also like to thank Geneva

Laurita, who has been the most insightful, collegial, collaborator one could ask for, in addition to modeling clear scientific communication and patient mentorship.

I also need to thank my family, starting with my parents, Jennie Tibben, Sharon Hickox, and Tim Young, and my siblings, Isaac, Jonathan, Grace, Nathan, and Noah, for allowing me to explain my research many many times and for helping me with the many aspects of graduate school that don't fall into the category of research. I also want to thank my partner, Bethany Ketchem, for her understanding, her sense of humor, and for reminding me of the bigger picture. I could name many other friends and family members here who were instrumental in helping me through the past five years. Thank you all for your kindness, companionship, and support.

This research was only made possible through financial support and computational (HPC) resources. I received funding from the Army Research Office (ARO) under Grant No. W911NF-15-1-0017. Calculations were performed using the Quest high-performance computing facility at Northwestern University which is jointly supported by the Office of the Provost, the Office for Research, and Northwestern University Information Technology; the Department of Defense – High Performance Computing Modernization Program (DOD-HPCMP); the National Energy Research Scientific Computing Center (NERSC), a DOE Office of Science User Facility supported by the Office of Science of the U.S. Department of Energy under contract no. DE-AC02-05CH11231; the Extreme Science and Engineering Discovery Environment (XSEDE), which is supported by National Science Foundation grant number ACI-1548562

Contents

Abstract	3
Acknowledgements	5
List of Figures	10
List of Tables	16
1 Introduction	17
1.1 Motivation	17
1.2 Organization	20
2 Methods	23
2.1 Density functional theory	23
2.1.1 Solving the many-body problem of quantum mechanics	23
2.1.2 Simulating condensed matter systems	25
2.2 Assumptions of the background-charge approximation	26
2.2.1 Changes in volume	28
2.2.2 Abrupt changes in conductivity	28
2.2.3 Homogeneous changes to crystallographic and electronic structure	31
3 Clarifying the intersection between acentricity and metallicity	33
3.1 Tensions in terminology: “ferroelectric” “metals”	33
3.1.1 Ferroelectric “metals”	34
3.1.2 “Ferroelectric” metals	40
3.2 Classifying the known metallic noncentrosymmetric materials	44
3.2.1 Suggesting new terminology	44
3.2.2 Materials which challenge the classification scheme	47
4 Persistent polar distortions from covalent interactions in doped BaTiO₃	54
4.1 Introduction	54
4.2 Materials and methods	58

4.2.1	BaTiO ₃ as a model material	58
4.2.2	Density functional theory	58
4.2.3	Carrier doping	59
4.2.4	Lattice dynamics	59
4.2.5	Electronic structure	60
4.3	Results	62
4.3.1	Charge redistribution upon electron and hole doping	62
4.3.2	Doping effects on the polar distortion	65
4.3.3	Electronic structure effects	70
4.3.4	Quantifying changes in bonding	72
4.3.5	Maximally localized Wannier functions (MLWFs)	75
4.4	Discussion	76
4.5	Conclusion	79
5	Transforming a strain-stabilized ferroelectric into an intrinsic polar metal via photodoping	80
5.1	Introduction	80
5.2	Methods	83
5.3	Results	84
5.3.1	Theoretical prediction of a doped ferroelectric	84
5.3.2	Experimental characterization of persistent polarization	86
5.4	Discussion	91
5.5	Conclusion	93
6	Designing an anti-Ruddlesden-Popper polar metal	94
6.1	Introduction	94
6.2	Methods	98
6.3	Results and Discussion	98
6.3.1	Electronic structure	98
6.3.2	Magnetism	101
6.3.3	Lattice dynamics and stability	102
6.3.4	Weak coupling	106
6.4	Conclusion	108
7	Conclusions and Outlook	109
7.1	Summary and conclusions	109
7.2	Frontiers in polar metals research	112
7.2.1	Two-dimensional heterostructures	112
7.2.2	Polar metallic pyrochlore	115

A Clarifying the intersection between acentricity and metallicity	145
B Persistent polar distortions from covalent interactions in doped BaTiO₃	152
C Transforming a strain-stabilized ferroelectric into an intrinsic polar metal via photodoping	159
D Designing an anti-Ruddlesden-Popper polar metal	161
Vita	171

List of Figures

1.1	Citations per year of Anderson and Blount’s 1965 paper on second-order martensitic phase transitions [1]. Note the significant increase in citations after the synthesis of the polar metal LiOsO_3 in 2013 [2]. Data collected from Google Scholar on July 6th, 2021.	18
2.1	(left) Schematic illustration of the difference in optical conductivity response across materials classes. (right) Experimental data from [3] illustrating the evolution of the optical conductivity of $\text{BaTiO}_{(3-\delta)}$ under oxygen vacancy doping at $T \approx 30\text{K}$	29
2.2	Schematic illustration of the effect of doping on the electronic structure under the VCA (top) and under more realistic substitutional doping mechanisms involving the formation of an impurity band (bottom)	30
3.1	Resistivities of a variety of metals, polar metals, and doped semiconductors are compared as a function of temperature. Although the polar metals exhibit electron transport roughly 1-2 orders of magnitude more resistive than “typical” elemental metals, they are still easily identifiable as significantly more conductive than the doped semiconductors (despite a positive slope in resistivity for La:BaTiO_3 throughout the temperature range).	38
3.2	Using crystal symmetry and electron transport as descriptors, the relationship between the various types of acentric conductors is illustrated. The gradient along the conductivity axis is meant to indicate that the line between metals and insulators is somewhat ambiguous in experiment, whereas the solid colors along the crystal symmetry axis indicate that the presence or lack of an inversion center is precisely defined. Transparency of overlapping categories indicates that a material may belong to multiple categories.	48
3.3	(a) Adding correlation to LiOsO_3 via increasing the Hubbard U (applied to Os d states) enhances the amplitude of the polar distortion. (inset) Schematic showing how polar distortion amplitude is defined by the relative long and short distances between Li and Os along the polar axis. (b) Crystal structure of polar ($R3c$) LiOsO_3 . (c) Increasing the degree of correlation in cubic BaTiO_3 (by applied the Hubbard U to the Ti d states) reduces the critical doping concentration to stabilize the soft Γ -point phonon mode of the cubic phase. (inset) The crystal structure of cubic ($Pm\bar{3}m$) BaTiO_3	52

4.1	Phonon dispersions for cubic ($Pm\bar{3}m$) BaTiO ₃ . The Slater mode, responsible for driving the ferroelectric transition to the tetragonal ($P4mm$) phase is circled. (inset) Unit cell for cubic BaTiO ₃ . Green, blue, and red spheres correspond to Ba, Ti, and O atoms.	61
4.2	(a) Electronic density of states (DOS) for tetragonal BaTiO ₃ with a molecular orbital diagram illustrating the covalent bonding between Ti and O. (b) Projected crystal orbital Hamiltonian population (pCOHP) for tetragonal BaTiO ₃ . (c-f) Illustration of the enhanced overlap under polar distortion along the z axis driven by the SOJT effect, shown for both (c,d) π -bonding between Ti $d(xz/yz)$ and O $p(x/y)$ and (e,f) σ -bonding between Ti $d(z^2)$ and O (pz). In the cubic structure, (c,e), the net overlap is 0 by symmetry, but becomes nonzero after the distortion as shown in (d,f).	61
4.3	(a) Wigner-Seitz radius (r_s) calculated on a path through the center of the relaxed BaTiO ₃ unit cell (cubic and tetragonal), along the axial Ti-O bond. The change in r_s along the same path in the tetragonal unit cell under (b) electron and (c) hole doping with the lattice parameters and atomic positions fixed to those of the relaxed (undoped) tetragonal unit cell.	64
4.4	(a) The axial c/a ratio and (b) degree of polar distortion (given by the ratio of the long Ti-O (ℓ) bond to half the lattice parameter along the c axis) of the relaxed tetragonal cell both fixed to the undoped volume and with the volume relaxed as a function of doping. (c) Slater mode (TO1) frequency as calculated for the high-symmetry cubic cell as a function of doping. (inset) Slater mode displacement pattern showing relative motion of Ti and the surrounding O anions.	67
4.5	Evolution of (a) conduction band minimum (CBM), (b) valence band maximum (VBM), and (c) energy differences E_1 and E_2 (defined in the inset) under electron and hole doping in tetragonal BaTiO ₃ , with lattice parameters and atomic positions held constant.	70
4.6	Carrier doping leads to similar responses in both the integration of the projected crystal orbital Hamiltonian population (ICOHP) up to the Fermi level (circles) and the projection of O_{ap} Wannier functions onto Ti states (squares). Both ICOHP and projection Wannier function data are shown for (a,b) π - and (c,d) σ -bonds. The evolution of each quantity under doping is shown for (a,c) the unit cell fixed to the undoped relaxed tetragonal phase and for (b,d) the fully relaxed unit cells (which initially are tetragonal but become cubic under sufficient electron doping).	72
4.7	(a) Two-dimensional slice of the MLWF associated with the Ti- $d(z^2)$ orbital, taken perpendicular to the a axis so that it cuts through the Ti and apical oxygen bond. (b) MLWF amplitude along the apical Ti-O bond. (c) Change in MLWF amplitude as a function of electron doping taken along the same path through the apical Ti-O bond.	75
5.1	a,b) Evolution of the Γ -centered TO1 and TO2 phonon modes for centrosymmetric tetragonal $P4/mmm$ EuTiO ₃ upon (a) increasing the in-plane tensile strain relative to the relaxed cubic lattice parameters and (b) increasing the photodoped-carrier concentration at 1.5% strain. (c) Electronic density of states (DOS) for $P4/mmm$ EuTiO ₃ at 1.5% strain.	85

5.2	Electrical characterization of the doped sample. (a) Resistivity as function of temperature. The behavior is metallic down to 4.2 K. A small upturn in resistivity at low temperatures is associated with strengthening of the FE order. (b) 2D carrier density inferred from the slope of the Hall effect taken at magnetic fields between -0.6 and 0.6 T.	87
5.3	(a) SHG intensity as function of analyzer angle for the doped sample shown for two input polarization geometries. The triangles near zero intensity (center of the figure) are measurements on a centrosymmetric - nonpolar film grown on LSAT. (b) SHG intensity as function of time delay relative to the pump pulse for 1200 nm (1 eV) excitation. Other wavelengths are shown in the inset. (c) Polar plots in the P_{in} geometry as before and after the pump pulse excitation at 1200 nm. (d) Fluence dependence of the SHG intensity ~ 10 ps after the pump pulse excitation at 1200 nm. The dashed line represents the fluence at which the photodoping equals the threshold for stabilization of the nonpolar phase found in our calculations (0.06e/u.c).	88
5.4	(a) Linear pump probe reflectivity at 80 K as function of pump fluence with wavelength of 1200 nm (1 eV). (b) Reflectivity signal at the minima of the pump probe traces shown in (a), the dashed line marks the saturation fluence value for SHG.	89
6.1	Comparison of (a) perovskite and (c) Ruddlesden-Popper structures with their (b,d) anti-structure analogs. In (a,c) the transition metal (Ti) is surrounded by an anion octahedron (O), whereas in (b,d) the anion (Si) is surrounded by a transition metal octahedron (Pt).	96
6.2	(a) Projected density of states (PDOS) and (b) projected crystal orbital Hamilton population (pCOHP) for $I4/mmm$ Ta_4As_2O . (a) Ta d -states dominate at the Fermi level, while As and O bands sit at lower energy. (b) Ta bonding interactions dominate, separating clearly into Ta-Ta, Ta-As, and Ta-O interactions. The Fermi level is located just above the transition from bonding to anti-bonding states, with a modest but non-negligible anti-bonding character at the Fermi level.	100
6.3	(a) Ta_4As_2O $I4mm$ phase, with Zintl clusters highlighted. (b) Total and projected DOS for $I4mm$ Ta_4As_2O . (c-e) Projected DOS for each Zintl cluster highlighted in (a).	101
6.4	(a-c) Phonon dispersions as calculated for (a) $I4/mmm$ Ta_4As_2O , (b) $I4mm$ Ta_4As_2O , and (c) $I4/mmm$ La_4Sb_2O . (d) Distortion modes Γ_1^+ (strain mode, amplitude = 0.36 Å) and Γ_3^- (distortion mode, amplitude = 0.60 Å) relating $I4/mmm$ and $I4mm$ phases of Ta_4As_2O . Arrows denote atomic displacements associated with each distortion mode (amplitude of distortion is exaggerated for clarity). Note that although $I4mm$ Ta_4As_2O is -480 meV/f.u. lower in energy than the $I4/mmm$ phase, there is no Γ point instability in the $I4/mmm$ phase.	104
6.5	The change in energy as a result of applying the symmetry adapted distortion modes describing the relationship between Ta_4As_2O $I4/mmm$ and $I4mm$ phases. The data labelled "I4mm lattice" applies the Γ_3^- distortion relative to an $I4/mmm$ crystal structure with the lattice constants of the $I4mm$ phase (so the 0 eV reference for that plot is an $I4/mmm$ structure with $I4mm$ lattice constants, not the fully relaxed $I4/mmm$ structure).	106
6.6	Projected COHP for the Ta_4As_2O $I4mm$ phase.	107

- 7.1 (a) Single crystal structure of $[\text{Co}(\text{en})_3](\text{CoS})_2 \cdot \text{en}$ where en = ethylenediamine. The [010] view of the orthorhombic unit cell with the $[\text{Co}(\text{en})_3]^{2+}$ octahedral complexes closer to the lower CoS layer by $0.135(5)\text{\AA}$ than they are to the upper CoS layer as indicated by the dashed lines. Hydrogens of C-2H₄-backbone of en left out for clarity. (b-c) Electronic density of states (DOS) for (b) model high symmetry structure with $Pbcn$ symmetry and (c) experimental low symmetry structure with $Pca2_1$ symmetry. Co* denotes the intercalate Co atoms. 114
- 7.2 Comparison of the distortion modes of the solid solution reveals that sulfur substitution not only alters the observed low temperature structure, but additionally changes the nature of the phase transition from (a) proper ferroelectric (FE) in the $x = 0.0$ sample, (b) to improper ferroelectric in the $x = 0.25$ sample, to (c) proper noncentrosymmetric (not ferroelectric) in the $x = 0.7$ sample. 116
- B.1 Theoretical phonon dispersion curves for the different polymorphs of BaTiO₃, after applying the non-analytical correction to account for LO-TO splitting. The panels are presented in order of appearance with decreasing temperature: (a) Cubic ($Pm\bar{3}m$) (b) tetragonal ($P4mm$) (c) orthorhombic ($Amm2$) and (d) rhombohedral ($R\bar{3}m$). After each phase transition, the number of unstable phonon modes decreases. There are three unstable phonon modes in the cubic phase (at least two are always degenerate), two unstable modes in the tetragonal phase, followed by one in the orthorhombic phase and eventually none in the dynamically stable rhombohedral phase. 153
- B.2 Comparison of Wigner-Seitz radius (r_s) along representative bonds in (a) NaCl and (b) ZnO. The bond between Na and Cl (a) is predominantly ionic; the elements involved are best described as exhibiting a transfer rather than a sharing of electrons between ions. This is evident from the large peaks in r_s along the Na-Cl bond, indicative of a significant decrease in the charge density. The short bond between Zn and O (b), however, shows a reduced r_s peak, indicative of electron sharing within a covalent bond. The large peak corresponds to a non-bonding interaction between O and the Zn of the next unit cell. Note that the height of the non-bonding (tall) peak in ZnO is similar to that of the ionic bond in NaCl, whereas the height of the covalent-bonding (short) peak in ZnO is comparable to that of the peak between Ti and O in BaTiO₃ (see Fig. 3a in the main text). As mentioned in the main text, we find r_s to be preferable to charge density for the analysis of changes in bonding character. With charge density, the assignment of charge to a particular point or path in space is somewhat arbitrary. Contour plots avoid this assignment but as a result lead to more qualitative analysis. Wigner-Seitz radius, on the other hand, provides a well-defined quantitative method for examining charge density along paths in real space. It allows for clear comparison of materials with different bonding character (as shown above) and under different doping configurations (as shown in the manuscript). For these reasons, we believe r_s provides a useful qualitative description of bond character. 154

- B.3 (a) Electronic density of states (DOS) for tetragonal BaTiO₃, with partial DOS projected showing the contributions from apical and equatorial oxygen atoms, respectively. Note that in each panel O_{eq} refers to the contribution from a single equatorial oxygen atom, not the combined contribution from the two symmetry-equivalent sites. Although the main text focuses primarily on the role of covalent bonding between Ti and O_{ap}, the Ti - O_{eq} interaction also affects the polar distortion. Panels (b) and (c) show the Crystal Orbital Hamilton Population (COHP) as projected onto (b) the three different Ti-O interactions (long/short Ti-O_{ap} and Ti-O_{eq}) as well as (c) the dominant orbital interactions between Ti and O_{eq} in particular. Note, only the contribution from a single Ti-O_{eq} interaction is shown, highlighting that while the combined Ti-O_{ap} degree of hybridization is certainly of greater magnitude than a single Ti-O_{eq} interaction, the combined effect of both equatorial oxygen sites will produce a comparable contribution. 155
- B.4 Evolution of (a) self force constants (SFCs) and (b) interatomic force constants (IFCs) under electron and hole doping in fully relaxed cubic BaTiO₃. Red shading indicates the displacement is more energetically favorable, whereas blue shading indicates enhanced stability of the the high symmetry structure. These trends occur with opposite signs for SFCs and IFCs. However, it should be noted that neither SFCs nor IFCs explicitly describe the degree of bonding, nor does an unstable element of the force constant matrix necessarily imply that a polar distortion is favorable (that can only be determined by considering the full force constant matrix, from which a phonon dispersion can be derived). Despite these limitations, the force constants of BaTiO₃ provide insight into the relative strength of driving forces behind the polar distortion and illustrate a sign-dependent perturbation of the Ti-O bond strength under doping. As we might expect from the Slater mode displacement pattern, the most unstable SFC is Ti, while the most unstable IFC describes the relative motion of Ti and O_{ap} (apical O atom). Similarly, these are the elements most affected (both strongly stabilized) by electron doping. Hole doping also has a strong stabilizing effect but, as with our findings from the phonon mode analysis, the stabilization is more gradual than in the *n*-type case and the results are also impacted by volume relaxation. This behavior is clearly discernible for the Ti SFC. Meanwhile, the other SFCs and IFCs are both more stable and exhibit only modest changes with doping. These sites are not expected to contribute strongly based on the first principles prediction of the pattern of local off-centering reflected by the Slater mode. They are likewise expected not to be greatly affected by doping since the strength of their out-of-plane interaction does not involve electronic states near the Fermi level. 156
- B.5 (a) Two-dimensional slice of the MLWF associated with the O_{ap}-*p*(*z*) orbital, taken perpendicular to the *a* axis so that it cuts through the Ti and apical oxygen bond. (b) MLWF amplitude along the apical Ti-O bond. (c) Change in MLWF amplitude as a function of electron doping taken along the same path through the apical Ti-O bond. Similar to the patterns seen for Ti-*d*(*z*²) in Fig. 8 of the main text, we see that electron doping appears to result in a net shift of the orbital lobes away from Ti and towards O. 157

B.6	Electronic band structure for undoped tetragonal ($P4mm$) BaTiO ₃ highlighting the projection of the maximally localized Wannier function (MLWF) associated with the $O_{ap-p}(z)$ orbital. Although the vast majority of bands with $O_{ap-p}(z)$ character are located in the valence band, some of the states traditionally associated with the Ti- $d(e_g)$ orbitals exhibit non-negligible $O_{ap-p}(z)$, evidence of the hybridization (bonding state) between Ti and O_{ap} . To generate the Wannier function projection data for Fig. 7 in the main text, we integrated the projection of $O_{ap-p}(z)$ onto the Ti- $d(e_g)$ states (as shown here) at each doping level.	158
C.1	Mode character projections were performed at each strain level by performing a dot product of the calculated eigendisplacement vector (mass-reduced and normalized) with the canonical perovskite displacement patterns from [4].	159
C.2	The two lowest-lying Γ -centered transverse optical modes for high symmetry $P4/mmm$ EuTiO ₃ at 1.5% strain under added electrons compensated by a neutralizing background charge (i.e. no hole generation).	160
D.1	Projected density of states for the $I4/mmm$ phase of (a) La ₄ P ₂ O (b) La ₄ As ₂ O and (c) La ₄ Sb ₂ O.	162
D.2	Projected density of states for the $I4/mmm$ phase of (a) Au ₄ As ₂ O (b) Au ₄ P ₂ O (c) Pt ₄ As ₂ O and (d) Pt ₄ P ₂ O.	163
D.3	Projected density of states for the $I4/mmm$ phase of (a) Ir ₄ As ₂ O (b) Ir ₄ P ₂ O (c) Os ₄ As ₂ O and (d) Os ₄ P ₂ O.	164
D.4	Projected density of states for the $I4/mmm$ phase of (a) Re ₄ As ₂ O (b) Re ₄ P ₂ O (c) W ₄ As ₂ O and (d) W ₄ P ₂ O.	165
D.5	Projected density of states for the $I4/mmm$ phase of Ta ₄ P ₂ O.	166
D.6	Projected density of states for the $I4/mmm$ phase of (a) Pt ₄ La ₂ Si and (b) Pt ₄ Ce ₂ Si. Ce f states are not shown because VASP struggles to project f states accurately. f orbitals in other PDOS plots are projected using LOBSTER. However, this requires running a DFT calculation with no symmetry, under which conditions the Pt ₄ Ce ₂ Si simulation struggles to converge. However, the total DOS near E_F can reasonably be expected to be dominated by Ce f states.	166
D.7	Phonon dispersions as calculated for $I4/mmm$ (a) Au ₄ As ₂ O (b) Au ₄ P ₂ O (c) Pt ₄ As ₂ O and (d) Pt ₄ P ₂ O	167
D.8	Phonon dispersions as calculated for $I4/mmm$ (a) Ir ₄ As ₂ O (b) Ir ₄ P ₂ O (c) Os ₄ As ₂ O and (d) Os ₄ P ₂ O	168
D.9	Phonon dispersions as calculated for $I4/mmm$ (a) Re ₄ As ₂ O (b) Re ₄ P ₂ O (c) W ₄ As ₂ O and (d) W ₄ P ₂ O	169
D.10	Phonon dispersions as calculated for $I4/mmm$ (a) Pt ₄ La ₂ Si (b) Ta ₄ P ₂ O (c) La ₄ As ₂ O and (d) La ₄ P ₂ O. Phonon dispersion for Pt ₄ Ce ₂ Si is not included, due to challenges converging simulations of the low-symmetry structural modulations required for the frozen-phonon method. However, structural relaxations in candidate ground state space groups were successfully performed, identifying $Ama2$ as the likely ground state structure.	170

List of Tables

- 3.1 Comparing plasma frequency and resistivity magnitudes as measured at room temperature between band metals (top) and doped semiconductors (bottom). 37
- 4.1 A comparison of several methods (both simulation and experiment) as applied to the study of cubic BaTiO₃, where a is the lattice parameter, V is the volume, E_g is the band gap, and the remaining columns are Γ -point phonon frequencies in cm⁻¹. LDA, PBE, and SCAN refer to the local-density approximation, Perdew-Burke-Ernzerhof, and strongly constrained and appropriately normed density functionals, respectively. 57
- 6.1 Candidate ground state symmetries as determined by relaxation along symmetry paths defined by lattice instabilities. Computed for A₄B₂X chemistries. The energy of each candidate ground state phase relative to the high symmetry $I4/mmm$ reference is also reported. 105
- A.1 Table of all published polar compounds exhibiting metallic conductivity. Columns denote space group (SG), presence of a polar structural phase transition (T_c), presence of a superconducting transition (T_{sc}), and presence of a magnetic ordering transition (T_N), respectively. Under SG: * = only the point group is known; “unknown” = the specific symmetry elements are unknown but there is evidence of broken inversion symmetry. Under T_c : P = compound is predicted but has not yet been synthesized. Under Class, the following abbreviations are in use: FE=ferroelectric; E=extrinsic; D=distortive; and A=anisotropic. 146

Chapter 1: Introduction

1.1 Motivation

In 1965, Anderson and Blount hypothesized that V_3Si might be capable of hosting both metallicity and a second-order inversion-symmetry-lifting structural phase transition [1]. The phase transition in V_3Si was subsequently shown to be a first-order, strain-driven transition, which did not break inversion symmetry [5–7], and for decades no other promising candidates would emerge.

The dearth of metals exhibiting a polar transition (i.e. polar metals) supported an intuitive understanding of polar distortion mechanisms, namely that polar displacements must be stabilized by long-range dipole-dipole interactions. In the absence of such interactions, short-range elastic repulsions would dominate, favoring centrosymmetry [8]. Introduction of free charge carriers, by virtue of Gauss’s Law, should lead to the screening of internal dipoles, thereby prohibiting long-range Coulomb interactions. Under this framework, all metals should be non-polar. Although, in 2005, metallic $Ca_3Ru_2O_7$ (CRO) was characterized in a noncentrosymmetric space group ($Bb2_1m$) [9], inversion symmetry in CRO is broken by non-polar RuO_6 rotations [10]. CRO does not exhibit a high-to-low symmetry phase transition and therefore no dipolar symmetry-lifting mechanism occurs, leaving the prevailing model of polar phase transitions intact.

This “long-range vs short-range” model for ferroelectric (FE) displacive transitions, and the

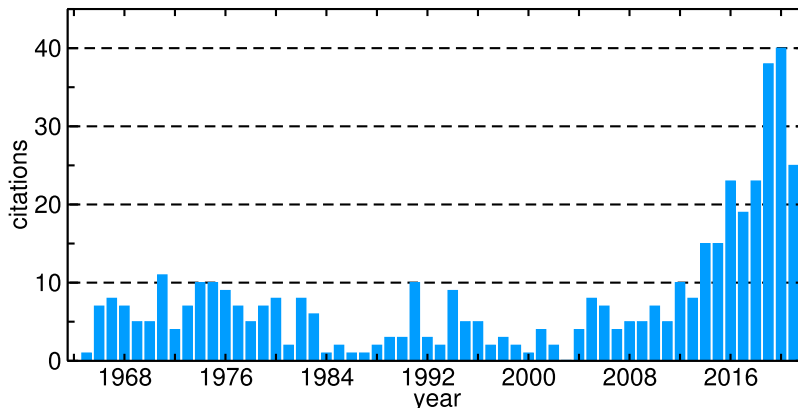


FIGURE 1.1: Citations per year of Anderson and Blount’s 1965 paper on second-order martensitic phase transitions [1]. Note the significant increase in citations after the synthesis of the polar metal LiOsO_3 in 2013 [2]. Data collected from Google Scholar on July 6th, 2021.

perceived absence of polar metals, would persist until 2013, when Shi et al. first observed a displacive transition in metallic LiOsO_3 . This discovery not only introduced a new class of materials, it also challenged decades of intuition surrounding relatively well-known ferroelectrics. Since 2013, interest in the combination of metallicity and broken inversion symmetry has skyrocketed (Figure 1.1). This includes both predictions and measurements of now polar metals as well as studies revisiting the driving forces of ferroelectrics (FEs) [10–14].

Amid the surge in recent interest, Puggioni and Rondinelli returned to the first prediction by Anderson and Blount and noted that one of their original observations applied to the polar metals being discovered 50 years later. Namely, that “while free electrons screen out the electric field [in materials] completely, they do not interact very strongly with the transverse optical phonons and the Lorentz local fields [that] lead to ferroelectricity, since umklapp processes are forbidden as $k \rightarrow 0$ [1].” They recast this observation as a design principle, formulating the so-called “weak-coupling hypothesis,” which states that a polar instability and metallic conductivity may coexist in the presence of weak-coupling between the inversion-lifting mechanism and the Fermi level, and used it to successfully design a new polar metal [10].

As our collective understanding of the interplay between conductivity and broken inversion improves, polar metals have taken on additional significance as promising technological materials. Although the academic interest in materials which combine contraindicated properties is substantial, the recent surge in research on polar metals is driven by the observation of a variety of properties—some more intuitive than others. As might be expected from polar materials with no depolarizing field (again, a consequence of Gauss’s law), polar metals have been shown to retain their polar structure down to single-layer thin films, well below the limit for their insulating ferroelectric counterparts [15], enabling the design of smaller switchable device architectures. As with all polar materials, polar metals demonstrate a non-linear optical (NLO) response, in some cases orders of magnitude beyond traditional NLO materials [16]. Some polar metals have also been shown to exhibit favorable thermoelectric properties, perhaps due to the weak coupling between electronic and crystallographic structures [10, 17, 18]. However, more surprisingly, a large number of polar metals have been shown to exhibit unconventional superconductivity [19–23]. This relationship appears more than coincidental, as evidenced by the correlation between polar instability and T_c in SrTiO₃ [22, 24] as well as the recent discovery of superconductivity in isostructural KTaO₃ [25, 26]. Beyond these well-established properties, polar metals have also been shown to be capable of hosting magnetoelectricity as well as non-trivial topological states [16, 27, 28].

The sudden increased interest in polar metals has, nonetheless, been accompanied by several opportunities for further development: (1) The synthesis of polar metals calls into question long-standing assumptions regarding the interplay between charge carriers and polar displacements in doped FEs (i.e. the “long-range vs short-range” model). Revisiting these systems is necessary both to clarify the distortion mechanism and to observe changes in the distortion pattern in the presence of a tunable free charge concentration. (2) The surge in research has been accompanied by a variety

of new terminology. Some of this has been useful, but some has also been confusing or misleading, often obfuscating important differences between distinct classes of materials. There is a need for consistent terminology and clarification of the many diverse subclasses of materials that combine polar order and metallic conductivity. (3) Our fundamental understanding of when the two orders may unite is still imperfect. Of the many materials classes known to host FEs, not all have been shown to also host polar metals, and it remains unclear whether this is due to a lack of study or a fundamental difference in distortion mechanism. Similarly, although the weak-coupling hypothesis appears to be valid in all synthesized polar metals, is the weak-coupling hypothesis always true? At least one possible counter-example has been predicted [12], although it has yet to be synthesized. In addition, the surprising coincidence of polar instability and superconductivity in SrTiO_3 – along with the many other polar superconductors – would imply that there is an important relationship between the structural distortion and the Fermi level.

In this dissertation, I use first principles density functional theory simulations to explore each of the above directions. In particular, I perform a detailed exploration of multiple doped FE systems, probing the impact of small changes at the Fermi level on lattice instabilities, displacement patterns, bond strengths, and electronic structure. I also work to clarify and categorize known and predicted polar metals. Finally, I use a combination of crystal-chemistry principles and electronic structure calculations to design a new family of polar metals.

1.2 Organization

This thesis is organized as follows:

- In Chapter 2, I provide the current status of the field of polar metals research, highlighting ongoing challenges and opportunities as well as summarizing and classifying the diverse known methods for combining metallic conductivity and broken inversion symmetry.
- In Chapter 3, I describe the methods employed in this investigation. First, I cover the basics of first principles density functional theory. Then I discuss specific considerations for accurate simulation of polar metallic materials and our approach to studying these compounds.
- In Chapter 4, I investigate the relationship between doped charge carriers and the polar structural instability in ferroelectric BaTiO_3 . Using a displacive, covalent bonding-driven model, I demonstrate the importance of short-range interactions in stabilizing polar distortions and shed new light on the role of coupling between the electronic structure and lattice instabilities as a predictor of compatibility between metallicity and broken inversion in doped proper ferroelectrics.
- In Chapter 5, I explore another doped ferroelectric system, strained EuTiO_3 thin films deposited on DyScO_3 . I use a photodoping approximation to demonstrate that photodoping eliminates the second-order Jahn-Teller (SOJT) instability, just as in BaTiO_3 . However, by comparing to experimental results I show that a SOJT model is insufficient to describe the lattice dynamics of this material and explain how strained EuTiO_3 undergoes a change in distortion character under photodoping, allowing for polar metallic behavior.
- In Chapter 6, I predict a new class of polar metals using the anti-Ruddlesden-Popper (anti-RP) structure type to design metallic compounds with inversion-lifting lattice instabilities. Only a handful of anti-RP compounds have been synthesized, but all of them have been insulating ferroelectrics. I discuss my design process and evaluate the electronic structure

and lattice instabilities of candidate high and low-symmetry phases in addition to searching for ground states. Finally, I assess how this new family of polar metals relates to the existing polar metal landscape and provide recommendations for experimental synthesis.

- In Chapter 7, I summarize my findings and suggest promising avenues for future research enabled by this work.

Chapter 2: Methods

This chapter provides a brief overview of *ab initio* electronic structure theory as implemented in density functional theory (DFT), which is the primary research tool used in this dissertation. I also provide specific considerations regarding the background-charge approach for simulating doped ferroelectrics (FE)—a method frequently employed both in this work and in literature—highlighting several considerations to be aware of with regard to how it does or does not emulate experimental doping conditions.

2.1 Density functional theory

2.1.1 Solving the many-body problem of quantum mechanics

At atomic or subatomic length scales (i.e. 10^{-10} m), a classical model of matter fails to accurately predict the interactions between particles. Whereas several empirical interatomic potentials exist (Lennard-Jones, Morse, etc.) [29–31], their applications are limited to predicting structural features and properties, and even this is not achieved without taking into consideration experimental measurements. Thus the empirical, semi-classical, approach is limited in scope with regard both to the properties described and in its ability to predict new compounds. Therefore, it is desirable that we model systems without requiring experimentally-informed parameters and instead use only the

details of the chemical species and their positions. In this manner, it is desirable that simulations be from “first principles” or *ab initio*. Such an approach is only possible with quantum mechanics.

One of the fundamental principles of quantum mechanics is that matter at subatomic length scales is not well described by rigid bodies, but rather by a probability distribution derived from its wavefunction. The form of that wavefunction is derived in simplest form using the time-independent Schrödinger equation

$$\hat{H}\Psi = E\Psi \tag{2.1}$$

which relates the Hamiltonian, H (more or less analogous to an effective energy potential), to the wavefunction, ψ , and the total energy of the system, E .

We can solve this equation explicitly for an electron whose wavefunction is shaped by some potential energy surface, perhaps the surface defined by a positively charged nucleus. This is possible with 2 interacting electrons as well. However, when we want to describe a real material, we generally need at least 3 electrons—if not tens or hundreds of electrons. And, unfortunately, solving the Schrödinger equation for 3 or more interactions bodies is analytically impossible, presenting the so-called “many-body problem.” Whereas this would seem to prevent the realization of first principles materials simulation, it is in fact possible to circumvent this barrier by treating N interacting electrons instead as an electron density $\rho(\mathbf{r})$, where ρ is the electron density defined as a function of position in real space \mathbf{r} . Hohenberg and Kohn proved that the total energy (E) of a system is uniquely determined by ρ , and that minimizing E with respect to ρ allows one to obtain the ground state charge distribution and the ground state energy E_0 [32]. Kohn and Sham further built on these proofs to show that the many-body interaction term can be replaced by an

independent-particle term of non-interacting electrons [33]. Through this combined effort, one then defines the total energy as

$$E[\rho] = \int d\mathbf{r} \rho(\mathbf{r}) V_n(\mathbf{r}) + \frac{1}{2} \int d\mathbf{r} d\mathbf{r}' \frac{\rho(\mathbf{r})\rho(\mathbf{r}')}{|\mathbf{r} - \mathbf{r}'|} - \sum_i \int d\mathbf{r} \phi_i^*(\mathbf{r}) \frac{\nabla^2}{2} \phi_i(\mathbf{r}) + E_{XC}[\rho(\mathbf{r})], \quad (2.2)$$

where ϕ is the single-particle wave function, V_n is the external potential, and E_{XC} is the exchange-correlation functional. Note this relationship is constructed such that the total energy depends on the value of another function (i.e. $\rho(\mathbf{r})$). This type of construct—a function of a function—is termed a functional, hence the name “Density Functional Theory”.

2.1.2 Simulating condensed matter systems

Equation 2.2 contains everything we know about the interactions in a material. The first term describes the contribution of the potential energy surface (i.e. the positions of the atomic nuclei, an applied electric field, etc.). The second term contains the electron-electron interactions and the third term describes the kinetic energy. As shown above, these first three terms all have exact formulations. However, one of the consequences of the Kohn-Sham non-interacting particles approximation is that some of the many body-complexity is shifted to a fourth term, E_{XC} , or the exchange-correlation functional. The exact form of E_{XC} is unknown. It contains a correction for the self-interaction energy (otherwise term 2 double counts an electron interacting with itself) as well as the exchange and correlation energies. These are quantum mechanical in nature, and are related to the fermionic exchange (i.e. Pauli exclusion) and a tendency for each electron’s location and movement to be “correlated” with the location and motion of other electrons. Since there

is no exact expression, approximations must be used. These vary considerably in their level of sophistication and accuracy, but in this dissertation I will almost exclusively use the generalized gradient approximation (GGA) as implemented by Perdew, Burke, and Ernzerhof and revised for solids (PBEsol) [34].

To treat wavefunctions, we take advantage of the periodicity of crystalline systems. Bloch's Theorem states that solutions to the Schrödinger equation take the form of plane waves modulated by a periodic function [35]. If we choose a sufficient number of plane waves, we can replicate any periodic wavefunction. In order to make practical use of DFT, you may observe that while we have described the method for converting between ρ and E , we do not have a way of *a priori* solving for the charge distribution ρ_0 that leads to E_0 . Therefore, DFT codes function by iteratively solving Equation 2.2, starting with an initial guess for ρ and mixing the new density with the prior density until the energy difference between iterations is below a pre-defined convergence threshold. Using this so-called self-consistent field (SCF) method, along with approximations for E_{XC} and a plane-wave approximation for wavefunctions, we can make robust predictions of the ground state properties of periodic systems ranging from lattice constants and mechanical properties to electronic structure and magnetism.

2.2 Assumptions of the background-charge approximation

The background charge approach has become the de-facto tool for use in studying the effects of electrostatic doping on solid state materials [13, 36–39]. This method works by changing the number of electrons present in a simulation of a material's electronic structure, while providing an additional homogeneous background charge to maintain charge-balance. The background charge approximation has become popular in doping simulations because it allows one to use smaller unit

cells than in substitutional or vacancy-doping simulation and because it allows one to isolate the effects of changes in electronic structure independent of the distortions resulting from real chemical dopants. This is an especially attractive combination of attributes when studying the interplay between free charge carriers and the polar distortion of ferroelectrics. The background-charge method is frequently used both to investigate fundamental relationships and to design possible polar metals [13, 36, 39, 40]. However, as will be discussed below, this approximation has consequences which don't always translate to physical systems. These include, but are not limited to:

- i) Changes in volume
- ii) Abrupt changes in conductivity
- iii) Homogeneous changes to electronic and crystallographic structure

Some of these problems are linked to the use of DFT as a simulation method in general (e.g. (iii) can be challenging to avoid while using periodic boundary conditions), and all them have been previously observed, but their shortcomings have been amplified through the application of the background charge technique to doped FEs.

Despite its limitations, the background-charge approximation remains an extremely valuable method of exploring the effects of doping on electronic and crystallographic structure. However, the consequences of using this approximation instead of more realistic substitution or vacancy-based doping simulations should be acknowledged to avoid arriving at inappropriate conclusions about the effect of doping in semiconductors, and in doped ferroelectrics in particular.

2.2.1 Changes in volume

The homogeneous background charge introduced in electrostatic doping simulations produces unintended consequences for the volume of the semiconductor being studied. The effective ‘pressure’ resulting from the additional electrons and associated background is ill-defined, resulting in inconsistent approaches depending on the choice of DFT software [38]. It follows naturally that this arbitrary treatment of volume leads to results that deviate significantly from experiment. For example, Iwazaki et al. showed that volume increase due to electrostatic doping simulations via the background charge method in BaTiO₃ dramatically overpredicted volume changes as compared to experimental substitutional doping [41]. Volume discrepancies dramatically impact properties, including the stability of the crystal structure, as volume is closely tied to phonon frequency. Simulations of soft phonon modes in BaTiO₃ under electrostatic doping with and without volume relaxation produce significantly different critical doping thresholds [37]. If the volume difference between polar and non-polar phases is substantial, then the volume changes induced by the VCA will intrinsically favor high or low symmetry structures depending on the relative volume [13, 41], obfuscating the changes induced by doping. Therefore, it is recommended that electrostatic doping via the compensating background charge approximation be performed with fixed volume. Volume relaxation should only be used when simulating substitutional, interstitial, or vacancy-based doping.

2.2.2 Abrupt changes in conductivity

In the pristine case, ferroelectric insulators are easily differentiated from metals, both computationally (i.e. gapped band structure) and experimentally (optical conductivity approaches zero as $\omega \rightarrow 0$, where ω is the photon frequency). Next, the addition of charge carriers can be achieved

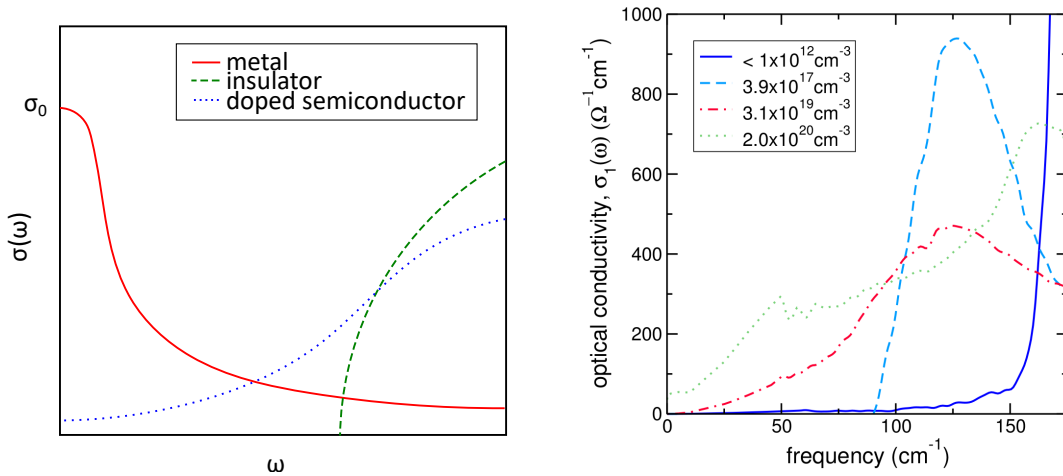


FIGURE 2.1: (left) Schematic illustration of the difference in optical conductivity response across materials classes. (right) Experimental data from [3] illustrating the evolution of the optical conductivity of BaTiO_(3-δ) under oxygen vacancy doping at T ≈ 30K

through chemical means (dopants) or electrostatic gating. Upon chemical substitution, defect states are introduced into the electronic structure of a semiconductor, allowing for modest conductivity thanks to thermally excited charge carriers occupying the defect states. This may lead to the material exhibiting metal-like resistivity vs temperature behavior (i.e. positive slope) away from 0 K, but as temperature is reduced the thermally activated charge carriers are frozen out and resistivity increases. This is reflected in the optical conductivity (σ_0), which still heads to 0 at low temperature (Figure 2.1).

Under additional doping an impurity band may form, transforming a degenerately doped semiconductor into a bad metal with low mobility from impurity scattering [42, 43], as shown schematically in Figure 2.2. In this case, the material will exhibit exclusively metallic characteristics, as the impurity band produces a finite σ_0 as $\omega \rightarrow 0$ below E_g , which can lead to the apparent closure of the gap with sufficient doping as low frequency spectra weight appears (Figure 2.1).

This gradual evolution in conductivity under doping, accompanied by the formation of an impurity band, is not well-described using the background charge method for doping approximation.

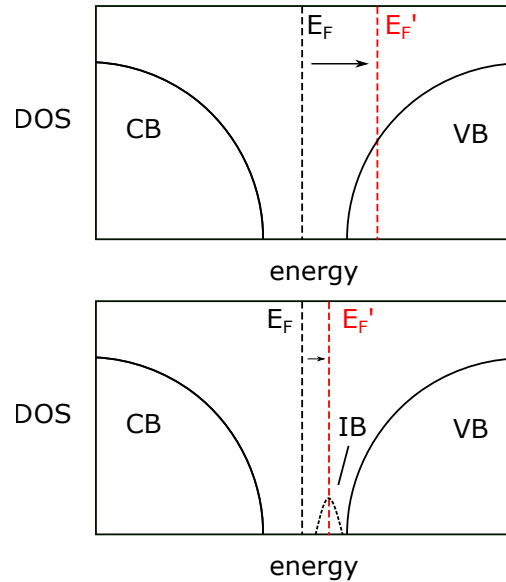


FIGURE 2.2: Schematic illustration of the effect of doping on the electronic structure under the VCA (top) and under more realistic substitutional doping mechanisms involving the formation of an impurity band (bottom)

In real semiconductors, the Fermi level before doping lies somewhere in the middle of the band gap (as opposed to at the top of the valence band, as it is traditionally reported in theoretical literature) and the addition of small concentrations of dopants to the system drives the Fermi level up or down within the band gap, but not to a degree sufficient to push the Fermi level into either the valence or conduction band (Figure 2.2).

Under the background charge method, even the slightest concentration of additional electrons (or holes) is sufficient to place the Fermi level within a band, making the system metallic far below even the electron concentration given by the Mott criterion ($n_c^{1/3} a_0 \approx 0.25$) for free electrons. Furthermore, the undoped band structure remains more or less intact, precluding the possibility of changes to the electronic structure due to impurity bands or polaron formation (Figure 2.2). This simplification obscures the complex reality of changes to the electronic structure which accompany the addition or subtraction of charge carriers in a material.

These changes are highly dependent on choice of starting material and the method of doping (substitution, vacancy, electrostatic, etc...). The critical charge carrier concentration (n^*) for conductivity in BaTiO_3 alone varies considerably across several doping mechanisms [44–46], all of which are significantly higher than n^* for SrTiO_3 [47]. The background charge method is not able to account for these differences, and therefore may lead to misleading conclusions about the ease of altering the conductivity of a material. It may come closest to approximating electrostatic gating, as this isn't typically associated with impurity band formation and so the consistent band structure may be a valid approximation. However, it still ignores charge localization mechanisms, as will be discussed in the next section.

2.2.3 Homogeneous changes to crystallographic and electronic structure

Below the impurity band formation limit, or under electrostatic gating, the carriers will either be homogeneously or inhomogeneously distributed at the nanoscale. At present, nearly all DFT calculations make the assumption that carriers are homogeneously distributed, and by construction the simulations result in a metallic electronic structure. Whether or not this model accurately captures the experimental situation requires attention, as recent extensions of semiconductor doping principles to transition metal compounds show that homogeneous distributions are often the exception rather than the rule [48].

For the inhomogeneous case, we anticipate nanoscale phase segregation to occur in close analogy to what happens across metal-insulator phase transitions in complex oxides, e.g., VO_2 [49]. Here doping then leads to domains that are either metallic or insulating and local structures that are centric and noncentrosymmetric, respectively. In other words, the regions that are metallic recover inversion while inversion symmetry remains lifted in the insulating regions. This electronic- and

parity-symmetry phase separation is supported by recent studies on BaTiO_3 and SrTiO_3 [44, 47]. Indeed, BaTiO_3 is much more difficult to make metallic than SrTiO_3 [47] with the key difference being the lattice dynamical properties; BaTiO_3 is a soft-mode semiconducting ferroelectric whereas SrTiO_3 is an incipient ferroelectric with a highly dilute superconducting transition. In practice this means that long range order quickly breaks down in doped BaTiO_3 , as the driving force for local off-centering persists leading to a network of disordered insulating octahedra separated by centrosymmetric metallic clusters hosting psuedo-localized free charge carriers. By contrast, under similar doping conditions, the more regular octahedra of SrTiO_3 enter a metallic—and subsequently superconducting—state. SrTiO_3 is not immune to nanodomain formation [50], but charge does not localize as easily. This highlights that experimental structure may exhibit heterogeneity in real-space with regard to electronic structure, crystal structure, or both.

Meanwhile, nearly all DFT calculations assume homogeneous doping. This is unavoidable to a certain extent, due to the prohibitive cost of simulating the large supercells necessary to capture nanodomain structures on the mesoscale. However, the background charge method further enforces uniformity, as the added charge carriers are distributed among the bands closest to the Fermi level while a homogeneous compensating background charge is added for charge balance. This makes it very challenging to simulate localization or polaron formation, let alone account for multiple phases.

Chapter 3: Clarifying the intersection between acentricity and metallicity

As the field of polar metals expands, it has become clear that the number of different methods for uniting free charge carriers and broken inversion symmetry has outpaced our terminology. In this chapter, I provide an overview of the challenges at play in striving to appropriately name and categorize the diverse known polar metallic compounds and present how they might be classified using clear descriptors.

3.1 Tensions in terminology: “ferroelectric” “metals”

Between the realms of theory and experiment, communication is critical in order to foster a productive relationship. Since communication is built on having a common vocabulary, this makes the terminology we use of utmost importance in seeking to advance the current understanding of our field. However, in the field of polar metals, some classifiers that seem obvious in theory are less well-defined in experiment, and the result has been confusing and at times misleading terminology. I present here a few examples of the two most common sources of dissonance between theoretical and experimental labels and suggest some methods for relieving said tension.

3.1.1 Ferroelectric “metals”

How to define metallicity?—The question of how one defines a ‘metal’ carries significance for many disciplines, but the distinction bears considerable weight when evaluating doped ferroelectrics (FEs), especially as a large number of reports describe doping FEs to achieve polar or “ferroelectric” metals. At what point does a doped ferroelectric become a polar metal? Is there an important fundamental difference between a polar structure with intrinsic charge carriers or extrinsic charge carriers? To answer these questions, let us consider the fundamental definitions of conductivity.

Electron transport considerations can, in principle, be used to quite clearly separate metals from insulators (dielectrics). According to Mott, “. . . a metal conducts, and a non-metal doesn’t” [51,52]. This statement is strictly true at $T = 0$ K and is often used as the discriminating factor between a metal and an insulator (or semiconductor) such that:

$$\lim_{T \rightarrow 0} \sigma(T) = \begin{cases} 0 & \text{insulator} \\ \sigma & \text{metal} \end{cases} \quad (3.1)$$

where σ corresponds to the electrical conductivity of the material. Within this definition, the distinction between a metal and an insulator can be understood using a single-electron band structure such that the electron chemical potential (or, rather, the Fermi level at 0 K) is located within a band for a metal. For an insulator the Fermi level is not well-defined, but it nominally resides within an energy gap. Importantly, the value of σ at room-temperature does not matter; thus, although the definition is mathematically well defined, experimental conditions ($T \neq 0$ K) can make the differentiation challenging, especially when the carrier density of a semiconductor is sufficiently high at room temperature. This may occur from intrinsic carriers in narrow gap semiconductors

or in the degenerate doping regime, such that the material is conductive through extensive doping [45,46,53,54]. These compounds are polar, and for reasonably large temperature ranges there is a positive correlation between resistivity and temperature, even though (strictly speaking) they tend to exhibit nonzero resistivity at 0 K. This fact may be why the boundary between semiconductors and metals is frequently blurred by experiment, despite the clear theoretical distinction [55–57].

Drude definition—Although the DC conductivity would appear to be the natural way to separate metals from insulators, in practice assessing the frequency dependent free-carrier response of the materials allows ones to treat metals, doped-semiconductors, and insulators on more equal footing [58]. For a perfect crystalline material with non-interacting electrons, the optical conductivity σ relates the electric current density due to a spatially uniform transverse electric field as

$$\sigma(\omega) = \frac{ne^2\tau}{m(1 - i\omega\tau)},$$

where m is the mass of the carrier (free electron mass or band renormalized mass) and n is the density of carriers (electrons or holes). Figure 2.1a shows that for an ideal metal the dc conductivity $\sigma_0 = ne^2\tau/m$ appears as a local maximum of $\sigma(\omega)$ at zero frequency (Drude peak) and then decays with a Lorentzian form due to finite relaxation time τ . In contrast, $\sigma(\omega) = 0$ for $0 \leq \omega \leq E_g$ in insulators with an optical gap E_g . This Drude definition would squarely categorize some doped FEs with very modest room temperature conductivity as fundamentally closer to insulators, providing some clarity. In addition, the nature of the optical conductivity may vary with temperature [59], allowing the metal-insulator classification to change with temperature—thereby accounting for metal-insulator transitions. However, sufficient doping of a ferroelectric can still lead to optical conductivities that remain nonzero as $\omega \rightarrow 0$, but do not reach a local maximum

at $\omega = 0$ (Figure 2.1), which presents a somewhat ambiguous case.

Another low-frequency dynamical property which is of relevance to distinguishing between metals and insulators is the non-adiabatic Born effective charge (naBEC) [60]. Whereas Born effective charges are typically only well-defined in insulators (as measurements of changes in polarization as a function of atomic displacement), naBECs are measurable in metals by considering the current generated in response to atomic motion. Atomic motion in this case is produced optically in a regime such that ω is much greater than the inverse carrier lifetime ($1/\tau$) while still being much smaller than interband resonances. Effectively (for materials with long carrier lifetimes) this amounts to $\omega \rightarrow 0$. As ω heads to 0, the naBECs stabilize as the “Drude weight”, or density of free charge carriers available for conduction. As with optical conductivity, this heads to 0 in insulators but reaches a non-zero value in metals. naBECs as an analog to BECs are also advantageous, as it allows for characterization of polarizability in metals despite polarization itself not being well-defined.

Order of Magnitude—Although for low-frequencies the optical properties of (doped) semiconductors are qualitatively similar ($\sigma \neq 0$), they are quantitatively different, because of the difference in carrier masses and densities. At high-frequencies, semiconductors and metals both absorb – as expected for an insulator with available conduction band states – owing to interband processes that give rise to finite $\sigma(\omega)$. The frequency crossover at which the behaviors change is given by the plasma frequency ω_p , corresponding to a zero in the real part of the dielectric function. Neglecting any damping effects, the plasma frequency can be expressed as $\omega_p^2 = ne^2/\epsilon\epsilon_0m$, where $\epsilon = \epsilon_\infty$ for a metal in that it includes only electronic contributions from (high energy) interband transitions while an insulator includes both electronic and ionic (static) polarization contributions, such that $\epsilon = \epsilon_\infty + \epsilon_{\text{ionic}}$ and $\epsilon_{\text{ionic}} > \epsilon_\infty$. As the carrier density increases, the plasma frequency increases:

Material	$\omega_p(\text{cm}^{-1})$	Resistivity ($10^{-6}\Omega\text{-m}$)
Al	1.19×10^5	2.82×10^{-2}
Cu	6.38×10^4	1.70×10^{-2}
Au	7.25×10^4	2.44×10^{-2}
Pb	6.20×10^4	2.20×10^{-1}
Ag	7.25×10^4	1.59×10^{-2}
n-GaAs	4.94×10^2	$\sim 10^3$
n-Si	1.76×10^3	10.7
p-Si	2.28×10^3	6.4
n-InSb	$\sim 2.1 \times 10^2$	$10^3\text{--}10^4$

TABLE 3.1: Comparing plasma frequency and resistivity magnitudes as measured at room temperature between band metals (top) and doped semiconductors (bottom).

in conventional metals ω_p is in the UV region which gives rise to the UV reflectivity edge (light of frequency $\omega < \omega_p$ is reflected). (In practice, this edge can be difficult to assess experimentally due to interband transitions and in some cases can be found just below visible frequencies.) In contrast, the carrier density in doped semiconductors places ω_p in the 100s of meV (5-30 μm range) as in *n*-InSb (Table 3.1) and is highly tunable [61].

Table 3.1 also illustrates the order of magnitude gap in resistivity between doped semiconductors and band metals (as does Figure 3.1). The order of magnitude not only distinguishes between metals and doped semiconductors but also leads to their use in vastly different applications. This distinction should be treated just as intentionally when comparing polar metals and doped FEs. However, it is worth noting that some materials would be mislabelled if one uses the order of magnitude of the plasma frequency or resistivity alone. Doped SrTiO₃ exhibits extremely low resistivity (including a superconducting transition) but the plasma frequency, even at low temperature, is in line with other doped semiconductors ($\sim 1.5 \times 10^3 \text{cm}^{-1}$) [62]. Meanwhile, many polar metals actually exhibit relatively poor conductivity (Figure 3.1), belonging to the so-called class of “bad metals” (e.g., LiOsO₃ has a room temperature resistivity of $15 \times 10^{-6} \Omega\text{-m}$ and a plasma frequency

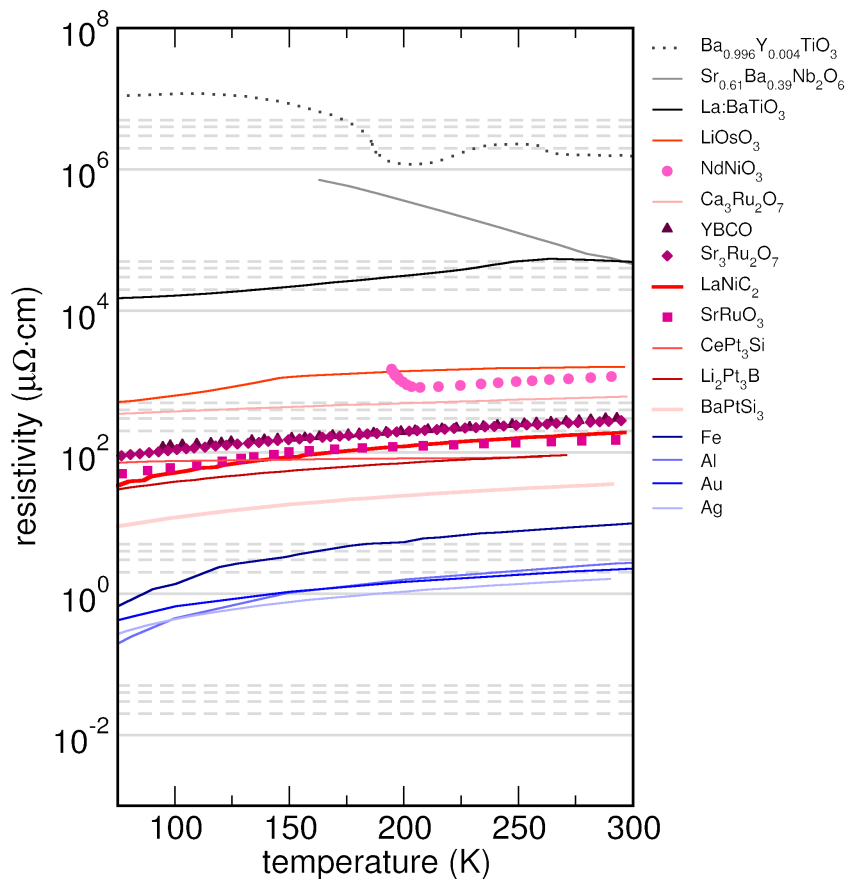


FIGURE 3.1: Resistivities of a variety of metals, polar metals, and doped semiconductors are compared as a function of temperature. Although the polar metals exhibit electron transport roughly 1-2 orders of magnitude more resistive than “typical” elemental metals, they are still easily identifiable as significantly more conductive than the doped semiconductors (despite a positive slope in resistivity for La:BaTiO₃ throughout the temperature range).

on the order of $\sim 10^2 \text{cm}^{-1}$) [2, 63].

Doping as perturbation—Although in many cases the descriptors above may be sufficient to clearly differentiate between polar metals and doped FEs, greater clarity may be achieved by considering doping as a perturbation to the initial state of a material and evaluating whether that perturbation has been sufficient to change the material’s classification. We consider two perturbative effects: electronic and crystallographic structure. The impact of doping on electronic structure is direct and immediately distinguishes intrinsic conductivity from extrinsic conductivity. Doping shifts the

Fermi level, which in most metals (i.e., excluding semi-metals) has little effect on the effective mass or concentration of the free charge carriers. In FE insulators, doping has an immediate impact, shifting the Fermi level toward a band edge and often inducing defect states, dramatically altering the conduction mechanism. This distinction has practical considerations, in that the transport properties of doped FEs will be more sensitive to changes in chemical potential than those of polar metals.

Predicting the effect of doping on crystal structure is less direct and requires an understanding of the structural driving forces. In the case of polar metals or doped FEs, the primary structural concern is the impact of doping on the inversion-lifting mechanism. Once again, different classes of materials will respond differently to doping as a perturbation. In doped proper FEs, the asymmetric structure is stabilized by a combination of dipole-dipole interactions and covalent bonding which act in competition with short-range repulsive forces which favor a higher symmetry structure [37,64,65]. Although the addition of charge carriers is not necessarily incompatible with the persistence of broken symmetry, it cannot help but reduce and eventually eliminate the influence of long range dipole-dipole interactions (due to the reduction of the screening length) and may also interfere with bonding, depending on the electronic structure of the material. By contrast, long-range interactions in polar metals are always screened and the atoms providing states at the Fermi level typically display weak coupling with the atoms active in the soft phonon(s) driving the symmetry-breaking distortion [66]. Thus, changes in the Fermi level of doped proper FEs will almost always eventually affect the ground state crystal structure whereas similar changes in the Fermi level of polar metals are more likely to leave the crystal structure unaltered.

As is true with each of the other above descriptors, some materials do not separate neatly into these two categories (perturbed and not-perturbed). For example, there are some ferroelectrics

which display persistent or enhanced polar displacements under doping [40]. However, I believe this combination of descriptors provides a framework for differentiating between true polar metals and a variety of degenerately doped ferroelectrics with persistent polarization under doping.

3.1.2 “Ferroelectric” metals

Contraindicated properties—Whereas long-range coordinated off-centering and metallic conductivity were long thought to be fundamentally incompatible only to be shown otherwise, the switchable polarization of a ferroelectric is, in principle, incapable of coexisting with free charge carriers. A ferroelectric phase is defined as “one in which the spontaneous electric polarization can be reoriented between possible equilibrium directions (determined by the crystallography of the system) by a realizable, appropriately oriented electric field” [67]. Unlike some of the conductivity definitions above, ferroelectricity is an engineering definition; whether a material is ferroelectric can only be confirmed via experimental verification of two criteria: (1) That the polar order occurs at zero electric field (i.e. *spontaneous* ordering) and (2) the polarization may be *switched* via external electric field according to the symmetry of the crystal structure. These two criteria lead to the appearance of domain microstructure, a well-known feature of ferroic properties which separates ferroelectrics from other noncentrosymmetric materials. Gauss’s Law prevents the generation of an internal electric field in a metal, thereby screening any attempt to switch the polarization of a polar metal via external electric field. However, this has not prevented the widespread use of the term “ferroelectric” or “ferroelectric-like” metal [11,12,18,45]. In this section I dissect what is and is not meant by this label and when it should be applied.

Ferroelasticity—Another ferroic order which I discuss in this section is ferroelasticity. The mechanical analog of ferroelectricity, a ferroelastic material exhibits two or more domains exhibiting

a spontaneous strain, the direction of which may be switched by applied external stress [67,68]. While ferroelectric and ferroelastic transitions are often accompanied by one another (as is the case in BaTiO₃), they may also occur independently, since all that is required for a ferroelastic transition is a change in unit cell shape, which may occur either with or without loss of inversion symmetry (for example, sodium trihydrogen selenite [69] and lithium niobate [70,71] both exhibit nonferroelastic ferroelectric phase transitions). Since ferroelasticity is defined without regard to electric field or charge carriers, there is no fundamental incompatibility between metallicity and ferroelasticity, therefore ferroelastic metals are an allowed class of materials. However, since they do not necessarily break inversion, I will only discuss ferroelastic metals in the context of coupling to a polar displacement.

Ferroelectric bananas—Electrical hysteresis measurements assess the change in charge Q on a pair of electrodes in contact with a dielectric material upon reversal of the applied bias, such that

$$Q = 2P_r A + \sigma E A t \quad (3.2)$$

where P_r , A , t , and E are the remnant electric polarization, area of the electrode contact, thickness of the dielectric, and the applied field, respectively, and σ is the conductivity. For either a degenerately doped ferroelectric or a polar metal, $\sigma \neq 0$ and thus the charge that switches is not due to an electric polarization but the finite conductivity of the material, which is well-understood to be dielectric loss as $P_r \rightarrow 0$ [72]. Nonetheless, some reports from the literature have claimed both to have synthesized a polar metal and to have measured a polarization [73,74]. However, we find these hysteresis loop reported in [73] to be consistent with examples from [72] demonstrating that even definitively non-polarizable materials (e.g., bananas) can still exhibit electrical hysteresis. Indeed,

the classification of a material as a metal is fundamentally incompatible with a bulk polarization within the adiabatic regime, as demonstrated by [57]. For these reasons, in principle one should not on the one hand call a material a polar metal and then report an electric polarization for it.

However, it is still possible to experimentally characterize the displacements of polar metals. The optical conductivity of noncentrosymmetric metals is used to evaluate the effect and magnitude of correlation effects [63, 75], but analysis of the spectral weights produced in those measurements can be used to derive non-adiabatic Born effective charges (naBECs), which provide insight into the role of various ions with regard to the inversion-breaking mechanism [60].

Switchable polar metals—However, recently a number of materials have emerged which use low-dimensionality, anisotropy, or ferroelasticity to demonstrate switchable polar metals [15, 75, 76]. It is still difficult to define a polarization ($\sigma \neq 0$) for these compounds, but nonetheless it is possible to reverse the direction of the polarization. Perhaps the most widely applicable switching mechanism is ferroelasticity. Although free charges screen external electric fields, strain fields experience no such screening. Although not all polar metals exhibit ferroelectric domains, a change in lattice parameters often accompanies polar distortions, making ferroelastic switching perhaps the most frequently viable switching pathway as demonstrated by Lei et al. [75].

Switching the polar displacement via electric field was only achieved recently within two-dimensional polar metals that exhibit anisotropic conductivity [15, 76]. With the polar axis oriented perpendicular to the plane, the minimal thickness of the conducting layer limits the number of free charges available to screen an applied electric field. This approach skirts the fundamental contradiction between metallicity and switchable polarization by compromising the conductivity of the polar metal along the polar axis. We might argue that the ferroelectric properties associated with these compounds are not intrinsic to the materials themselves but rather a product of the

architecture and dimensionality of their synthesis.

I should note that although they have yet to be realized in experiment, there is a third proposed mechanism toward switching a polar metal. Namely, a thin polar metal film is deposited on a FE with low lattice mismatch. An external electric field switches the FE substrate and the resulting strain switches the polar metal [12, 77]. This approach might be considered a variation of the ferroelastic switching mechanism, as both approaches use the unscreened strain field to switch polarization.

“*Ferroelectric-like*”—“Ferroelectric-like” or “ferroelectric” (in quotes) terminology has been used to describe structural phase transitions in polar metals since the first report of its kind in 2013 [2], with many other studies since following suit with this naming convention, either in reference to the material itself or to the inversion-lifting transition (e.g. [11, 12, 18, 45]). Despite the history of this convention, describing something as “ferroelectric-like” is inherently ambiguous, as it leaves unclear which aspect(s) of ferroelectricity are being replicated. The comparison to FEs implies that the polarization is switchable, which—as noted above—is only true in very specific cases. The intended FE attribute being referred to is the presence of a second-order, structural phase transition that removes the operation of inversion. Given the possibility for confusion, more precise terminology is recommended.

Piezoelectric metals—Piezoelectricity is defined as a change in polarization in response to a mechanical stress, the only prerequisite for which is a lack of an inversion center. However, as was observed when discussing “ferroelectric” metals, polarization in a metal is ill-defined. Nonetheless, the Berry curvature effects observed in noncentrosymmetric insulators give rise to analogous properties in metals. Although a static polarization has no meaning in a conductive material, changes in electric polarization are instead measurable as a bulk current, making piezoelectric metals a

meaningful designation. Varjas et al. also demonstrated that noncentrosymmetric metals with broken time reversal symmetry should exhibit a magnetopiezoelectric effect (MPE) [27], as was observed recently in antiferromagnetic EuMnBi_2 [78]. It is noteworthy that while all ferroelectrics by definition must exhibit piezoelectricity, not all piezoelectrics will be ferroelectric. This distinction is especially significant in metallic systems as the vast majority of polar metallic systems are not switchable, making “piezoelectric metal” a more accurate and more frequently applicable label than “ferroelectric metal”.

3.2 Classifying the known metallic noncentrosymmetric materials

3.2.1 Suggesting new terminology

Summarizing the above considerations and descriptors, I have identified the following unique categories of polar conductors:

1. *Polar metal*: A polar metal exhibits a polar crystal structure, identifiable via structural characterization techniques, such as X-Ray diffraction, neutron diffraction, or the observation of properties associated with broken inversion symmetry (i.e., second harmonic generation). A polar metal should also conduct electricity, as determined via a local maximum in its optical conductivity as $\omega \rightarrow 0$. Finally, the inversion-lifting mechanism and electron transport should be more or less unaffected by small perturbations to the Fermi level. Restated, to be considered a polar metal, the polar distortion and metallicity should not be contraindicated. Examples include LiOsO_3 [2], $\text{Ca}_3\text{Ru}_2\text{O}_7$ [9, 75], and CePt_3Si [79].
2. *Distortive polar metal*: A distortive polar metal is a sub-category of polar metal, meeting all of the above criteria while also exhibiting an inversion-symmetry lifting phase transition.

This eliminates the need for misleading “ferroelectric-like” terminology and its derivatives by highlighting the intended comparison to ferroelectric phase transitions. This category also separates polar metals exhibiting phase transitions from polar metals in which inversion is lifted via compositional order. This is a meaningful distinction, both from a fundamental physics perspective as well as an application-driven perspective, as the presence of a phase transition implies opportunities to tune that transition not necessarily available to polar metals which do not undergo a phase transition. Structural phase transitions in polar metals have been experimentally observed via second-order discontinuities in electronic transport, heat capacity, magnetic susceptibility, dielectric response, second harmonic generation, and of course structural features from scattering and diffraction techniques [2, 3, 24, 45, 80, 81]. Within distortive polar metals—as is true with ferroelectrics—the phase transition may be displacive, order-disorder, or exhibit elements of both characters. Examples of distortive polar metals include LiOsO_3 (primarily order-disorder) [2, 81–83] and $\text{Pb}_2\text{CoOsO}_6$ (primarily displacive) [80]. Examples of non-distortive or compositional polar metals include CePt_3Si [79] and ErPdBi [84].

3. *Anisotropic ferroelectric metal*: An anisotropic ferroelectric metal meets the structural criteria for a distortive polar metal but exhibits limited conductivity along the polar axis, allowing for observable switching of the polar displacement direction via external electric field. “Anisotropic” is meant to call attention to the fact that is it the anisotropic geometry of the device architecture which enables one to sidestep the fundamentally contraindicated relationship between field-switchable polarization and conductivity. Ferroelectricity is not, and by definition cannot, be an intrinsic property of a metal, but low-dimensional design strategies are able to anisotropically modify the metallic behavior of polar metals such that the

polarization becomes switchable by external electric field. Examples include WTe [15] and $\text{Bi}_5\text{Ti}_5\text{O}_{17}$ [76]. NOTE: polar metals whose polar order is switched via strain are not classified as anisotropic ferroelectric metals, as this switching mechanism does not require limiting the fundamental relationship between external electric field and free charge carriers.

4. *Extrinsic polar metal*: An extrinsic polar metal must meet each of the structural and electronic criteria of a polar metal (i.e., polar structure, metallic optical conductivity, robust polar distortion in the presence of perturbations to the Fermi level). However, a polar metal is deemed extrinsic if the metallic electron transport is a result of perturbations to the pristine state of the material. The number of charge carriers or conductivity of an extrinsic polar metal is sensitive to doping mechanisms, such as chemical substitution, interstitials, vacancies, photodoping, and electrostatic gating. This distinction has consequences for application contexts in which sensitivity to small changes in chemical potential either positively or detrimentally impacts performance. Examples include Nb-doped PbTiO_3 [40] and doped SrTiO_3 [85, 86].
5. *Degenerately doped ferroelectric*: A degenerately doped ferroelectric meets the same structural criteria as the other categories, but the structural transition is detrimentally impacted by perturbations to the Fermi level from a pristine insulating state. In such a material, the polar order and the conduction mechanism are contraindicated, which both implies a fundamentally different relationship between the polar structure and the conduction mechanism than in the above categories and impacts the applications of degenerately doped ferroelectrics. If degenerately doping a ferroelectric is seen as a pathway to accessing the many desirable properties of a polar metal, it should be performed in a context where careful control of

the chemical potential is possible and practical. The conductivity threshold required to be deemed “degenerately doped” rather than “metallic” is somewhat ambiguous, but a minimum criteria should be $\sigma \neq 0$ as $\omega \rightarrow 0$. The primary example of a degenerately doped ferroelectric is doped BaTiO_3 [3, 37, 46].

The relationship between these different categories is summarized in Figure 3.2. Surveying the known metallic and acentric compounds in the literature as of the August 2021, I have categorized each according to this scheme in a table available in Appendix A.

3.2.2 Materials which challenge the classification scheme

Changing classification—Despite the consideration put into the above classification scheme, there remain materials which prove difficult to categorize. The majority of such cases involve materials which undergo significant changes in conductivity or displacive mode dynamics as a result of changes in their environment. In most cases, it is simplest to describe a material as moving between categories as a function of some perturbation. For example, a polar material exhibiting a metal-insulator transition would simply transition from being a polar metal to being a ferroelectric. Similarly, strained EuTiO_3 initially exhibits degenerately doped ferroelectric-type behavior under photodoping, as the amplitude of the polar displacement decreases with the first excited charge carriers. However, under greater fluences this decrease in amplitude plateaus at more than 80% the initial displacement and persists at this value. Therefore we would say that strained EuTiO_3 transitions from a degenerately doped ferroelectric to an extrinsically metallic polar metal under photodoping (see Chapter 5).

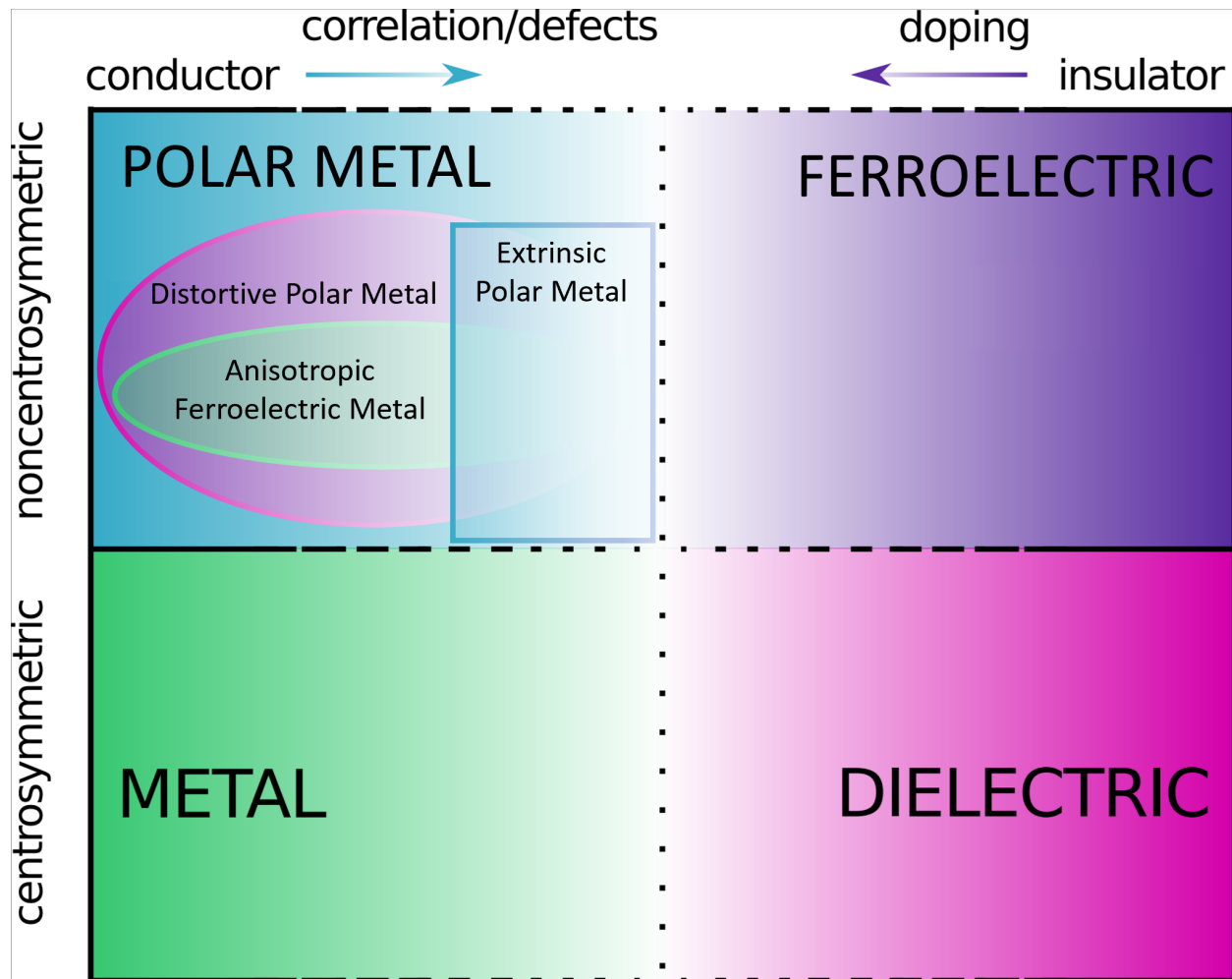


FIGURE 3.2: Using crystal symmetry and electron transport as descriptors, the relationship between the various types of acentric conductors is illustrated. The gradient along the conductivity axis is meant to indicate that the line between metals and insulators is somewhat ambiguous in experiment, whereas the solid colors along the crystal symmetry axis indicate that the presence or lack of an inversion center is precisely defined. Transparency of overlapping categories indicates that a material may belong to multiple categories.

Constructive coupling between polar distortion and charge carriers—Another interesting case is doped $\text{Sr}_3\text{Sn}_2\text{O}_7$, which is predicted to exhibit a polar displacement that is enhanced as a consequence of doping an initially insulating material [87]. Strictly speaking, assuming doping occurs at such level so as to pass the Drude criterion for conductivity, it would be tempting to categorize $\text{Sr}_3\text{Sn}_2\text{O}_7$ as a degenerately doped ferroelectric, since the polar distortion is sensitive to changes at

the Fermi level and the pristine state is ferroelectric. However, since polar order and conductivity are clearly not fundamentally contraindicated in this compound, it may be wise to reclassify as an extrinsically metallic polar metal. Such a classification would be made easier if the polar mode amplitude plateaus under doping to reach a steady state, relatively insensitive to changes at the Fermi level. It is also worth noting that the material has not yet been synthesized and characterized in experiment and we may discover that the real material behaves differently than anticipated.

Distortive polar metals and domain structures—In differentiating between polar metals that exhibit a structural phase transition and those that do not, a key feature with technological applications in distortive polar metals is their domain structure. Metallic domain walls in ferroelectrics like BiFeO_3 [88] and YMnO_3 [89] are currently being investigated for use as non-destructive resistance-based memory devices [90]. Similarly, in $\text{Ca}_3\text{Ru}_2\text{O}_7$, both charged and uncharged domain walls were shown to exist—each associated with different electrical conductivity—implying potential application in charge-mediated memory devices as well [91]. However, under the current classification scheme, $\text{Ca}_3\text{Ru}_2\text{O}_7$ would not be classified as a distortive polar metal because the temperature at which it would undergo a structural phase transition to recover centrosymmetry is above the temperature at which this chemistry exists in the solid state.

And yet a polar metal with a clear local ordering mechanism, as is the case in $\text{Ca}_3\text{Ru}_2\text{O}_7$, should be considered meaningfully distinct from compositionally-ordered polar metals like half-Heulser alloys—as was discussed by Puggioni and Rondinelli in [10]. One distinguishing characteristic should be the domain structure and the possibility of domain wall motion. When there is a structural origin to the local off-centering, domain walls are clearly defined structurally and there is at least a potential pathway to domain wall motion via external perturbation (most likely mechanical stress, as in [75]), whereas the domain walls in compositionally-ordered polar metals would be

defined by regions of ordered and disordered site occupancy. Similarly, although in a non-distortive polar metal the high symmetry reference is never actually achieved, modulation of temperature affects compositionally-ordered polar metals differently from those with a local-ordering mechanism. Whereas temperature tunes the magnitude of the atomic displacements relative to a theoretical high symmetry structure in locally-distortive polar metals, there are no displacements to tune in compositionally-ordered polar metals and the high symmetry reference is defined by disordered site occupancy.

New potential subcategories—There are other subcategories across polar metals classes which may warrant their own subsection, of which I will discuss three: (1) magnetic materials, (2) correlated materials, and (3) violations of weak-coupling. Beginning with magnetic polar metals, there are many known acentric conductors with magnetic ordering temperature (across all of the above categories), including the following: en-CoS [92], $\text{Pb}_2\text{CoOsO}_6$ [80], $\text{Pb}_2\text{NiOsO}_6$ [93], tri-color superlattices $\text{BaTiO}_3/\text{SrTiO}_3/\text{LaTiO}_3$ [94], $\text{Ca}_3\text{Ru}_2\text{O}_7$ [9], and more. The relationship between magnetic ordering in these materials and their designation as polar metals varies. For example, Jiao et al. describe separating polar metals with magnetic ordering temperatures into “type-I” and “type-II” categories depending on the strength of the coupling between magnetic and polar orders, with $\text{Pb}_2\text{CoOsO}_6$ being an example of a “type-II” magnetic polar metal [80]. By contrast, the magnetic ordering predicted in $\text{SrCaRu}_2\text{O}_6$ is not expected to couple to the inversion-lifting distortion [10], or one might look at the insensitivity of the polar transition in doped SrTiO_3 to the presence of magnetic doping and isovalent substitution as an example of “type-I” behavior [95]. Still we may describe other categories, including magnetically-driven metal-insulator transitions in $\text{Pb}_2\text{CaOsO}_6$ [96] and B-site substituted $\text{Ca}_3\text{Ru}_2\text{O}_7$ [97–99] (in which case the magnetic and transport properties are highly sensitive to dilute concentrations and dependent on the substituting species—Mn, Ti, or

Fe). Such sub-categorization according to magnetic properties helps describe fundamentally different physical phenomena, but may be well-suited to more detailed investigations which may coexist with the classification scheme presented above.

Correlation also plays a significant role, both in the realization of polar metals generally and in the potential to drive metal insulator phase transitions, often in concert with magnetic ordering. Evidence of the former is found in the number of polar metals which exhibit “bad”, correlated behavior (Figure 3.1). Although it is now well-established that short-range interactions play a dominant role in driving local off-centering in polar metals, reduction of the screening length via correlation may enable longer-range interactions to further enhance the displacement magnitude, or at least allow for long-range coordination of local displacements. Regardless, it was shown in [100] that the polar displacement of the predicted polar metal $\text{SrEuMo}_2\text{O}_6$ is enhanced by introduction of additional correlation via the Hubbard U . A similar effect is observed when plotting the effective polar amplitude in LiOsO_3 vs U (Figure 3.3a). However, just as correlation may help to stabilize or enhance polar displacements, when coupled with magnetic ordering it may also drive Mott-type metal insulator transitions, as shown in $\text{LiOsO}_3/\text{LiNbO}_3$ superlattices [101]. The effect of correlation on a system is also highly dependent on the distortion mechanism. In the absence of magnetism, correlation was shown to reduce the critical free carrier concentration in doped BaTiO_3 (Figure 3.3c). The more highly correlated Ti d states exhibited weaker covalent bonding with O p states, favoring the high symmetry structure. Previous studies of correlation in polar metals implied that correlation should assist in decoupling free charges from the symmetry-lowering transition, but the result of BaTiO_3 illustrates that the impact of correlation is highly dependent on the driving force behind local off-centering.

Finally, if polar metals exhibiting strong coupling between the Fermi level and the structural

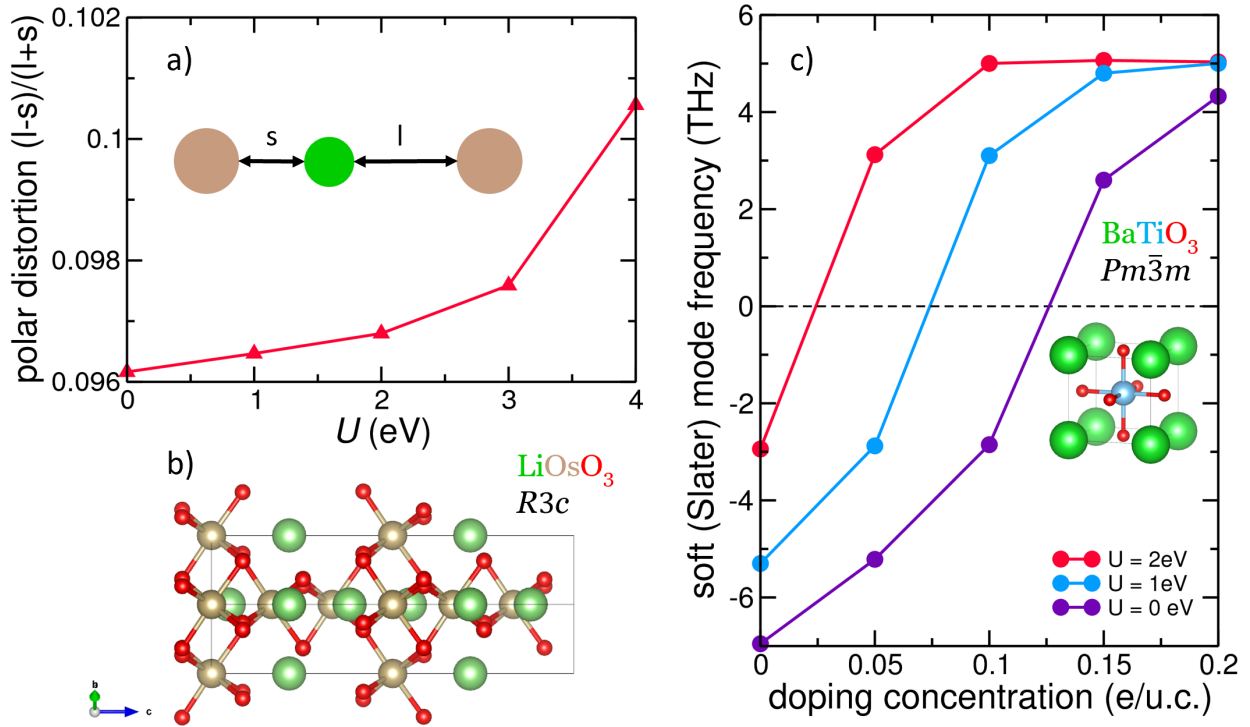


FIGURE 3.3: (a) Adding correlation to LiOsO_3 via increasing the Hubbard U (applied to Os d states) enhances the amplitude of the polar distortion. (inset) Schematic showing how polar distortion amplitude is defined by the relative long and short distances between Li and Os along the polar axis. (b) Crystal structure of polar ($R3c$) LiOsO_3 . (c) Increasing the degree of correlation in cubic BaTiO_3 (by applied the Hubbard U to the Ti d states) reduces the critical doping concentration to stabilize the soft Γ -point phonon mode of the cubic phase. (inset) The crystal structure of cubic ($Pm\bar{3}m$) BaTiO_3 .

distortion were to be discovered, they may deserve separate categorization as well. Although TiGaO_3 has been predicted as a compound that might violate the weak-coupling hypothesis [12], it would be hasty to separately categorize such a material prior to experimental synthesis and characterization. In fact, I recently computed the decomposition enthalpy of TiGaO_3 to be about -1eV/f.u. , making it unlikely to be realized in experiment. Studying a series of related ABO_3 compounds ($A=\text{Ti,Zr}$; $B=\text{Al,Ga,In}$) revealed that while each demonstrated a dynamically stable polar phase driven by displacements of the A-site cation (which also contributed to the Fermi level), none exhibited a decomposition enthalpy smaller in magnitude than -0.8eV/f.u. As was

the case with $\text{Sr}_3\text{Sn}_2\text{O}_7$, it seems prudent to primarily concern ourselves with the classification of known compounds, as the synthesis of exotic predicted compounds may reveal features that aid in their classification. Alternatively, we may yet discover factors that prevent the synthesis of acentric conductors that challenge our classification scheme. In the mean time, it is incumbent on theoretical and computational materials scientists to examine the stability of their predicted compounds before sharing their results [102].

Chapter 4: Persistent polar distortions from covalent interactions in doped BaTiO₃

Reprinted with permission from [103].

4.1 Introduction

The traditional framework for understanding polar displacements pitted long-range dipole-dipole interactions (which favor coordinated off-centering, active in dielectrics) against short-range repulsive forces (which favor high-symmetry structures) [8]. This framework is consistent with a large body of experimental and theoretical literature [36, 44, 47, 65], confirming the importance of long-range interactions in stabilizing polar distortions. Such a model implies that high electrical conductivity should be fundamentally incompatible with polar structures, since the free charges screen long-range Coulombic interactions. Indeed, this appeared to be the case until the synthesis of the first polar metal, LiOsO₃, in 2013 [2].

Although the existence of polar metals was hypothesized as early as 1965 [1], interest in such materials did not begin in earnest until after 2013. Since then, many additional polar metals were proposed and discovered [10, 12, 75, 104, 105], leading to a reexamination of the prototypical proper

ferroelectric BaTiO₃ under doping as a means to study the interplay between polarization and carrier-controlled metallicity. Considered a prime example, *n*-type doping has consistently been shown to stabilize the cubic phase of BaTiO₃ [36, 44, 46, 47]. However, recent work suggests that this preservation of inversion symmetry occurs above the threshold required to screen long-range dipole-dipole interactions [45, 46, 106, 107], implying a more complex relationship among the charge carriers, the electronic bands they occupy, and the microscopic structural distortion mechanisms leading to inversion lifting in *d*⁰ compounds.

In this work, we present a first-principles analysis of the polar distortions in BaTiO₃ under *n*- and *p*-type doping. Although long-range dipole-dipole interactions are clearly important for stabilizing cooperative displacements over the nanoscale and micronscale lengths that result in long-range polar order, we focus on the local off-centering mechanisms within a TiO₆ octahedron. We consider the impact of electrostatic doping through its influence on the second-order term of an expansion of the total energy *E* of a material with respect to distortions *Q* from a high-symmetry (cubic) configuration, otherwise known as the second-order Jahn-Teller effect (SOJT) [64, 108, 109]:

$$\begin{aligned}
 E &= E^{(0)} + \langle 0 | \mathcal{H}^{(1)} | 0 \rangle Q \\
 &+ \frac{1}{2} \left[\langle 0 | \mathcal{H}^{(2)} | 0 \rangle - 2 \sum_n \frac{\langle 0 | \mathcal{H}^{(1)} | n \rangle^2}{E^{(n)} - E^{(0)}} \right] Q^2 + \dots
 \end{aligned}
 \tag{4.1}$$

The $|0\rangle$ and $|n\rangle$ refer to the ground and excited states, respectively. The first-order term, $\langle 0 | \mathcal{H}^{(1)} | 0 \rangle Q$, describes the first-order Jahn-Teller effect (FOJT) and is driven by orbital degeneracy. This term is reduced to 0 in *d*⁰ compounds and will not be the focus of our discussion. In the second-order term, $\langle 0 | \mathcal{H}^{(2)} | 0 \rangle$ is a diagonal matrix element referring to a coordinated displacement in unit cells

throughout the crystal, akin to an elastic restoring force. This term (also described as the non-vibronic coupling term) is always greater than zero, and therefore always repulsive, stabilizing the high symmetry structure ($Q = 0$). The summation in Equation 4.1 describes the mixing of ground and excited states (covalent interactions). It is exclusively a short-range interaction and favors off-centering ($Q \neq 0$), provided the symmetry of the low-lying energy states is appropriate so that $\langle 0 | \mathcal{H}^{(1)} | n \rangle$ is non-zero. It is this second-order term which provides the framework for our analysis.

Rather than calculate the second-order term directly (by calculating the Hamiltonian matrix at several distortion amplitudes for each doping level and using finite differences to find the first and second derivatives of each element of the Hamiltonian), we pursue a less labor-intensive approach that can be broadly applied to more complex (multi-band) materials. We examine the evolution of several atomic- and electronic-structure-level metrics under carrier doping, defined below, that approximate the components of the second-order term. Namely, we use the Wigner-Seitz radius (r_s), force-constant matrix, band edge energy differences, and crystal orbital Hamiltonian population (COHP) analysis. These metrics can be computed with relatively low human effort and with minimal computational resources (especially since all but the force constants can be computed using the output of a single point total energy calculation, e.g., a density functional theory calculation). In addition, each metric relates intuitively to the changes in chemical bonding, and we expect them to transfer to the study of the local bonding environment in other materials, such as polar metals, where delocalized descriptions are used and the features of dielectrics can be difficult to transfer. We also validate findings obtained with these metrics by comparing to results derived from computing maximally localized Wannier functions (MLWFs), which provide accurate local descriptions of electronic structure in both metals and insulators using a different basis (i.e. Wannier functions) than our density functional theory calculations (which use a planewave basis) [110].

TABLE 4.1: A comparison of several methods (both simulation and experiment) as applied to the study of cubic BaTiO₃, where a is the lattice parameter, V is the volume, E_g is the band gap, and the remaining columns are Γ -point phonon frequencies in cm⁻¹. LDA, PBE, and SCAN refer to the local-density approximation, Perdew-Burke-Ernzerhof, and strongly constrained and appropriately normed density functionals, respectively.

Method	$a(\text{\AA})$	$V(\text{\AA}^3)$	$E_g(\text{eV})$	$T_{1u}(\text{TO1})$	$T_{1u}(\text{TO2})$	$T_{2u}(\text{silent})$	$T_{1u}(\text{TO3})$
Experiment [111]	4.01	64.29	3.2 [112]	soft [113]	182 [113]	306 [113]	482 [113]
DFT-LDA [65]	3.94	61.16	1.84	113 <i>i</i>	184	288	481
DFT-PBE [114]	4.04	65.74	1.9	240 <i>i</i>	175	290	460
DFT-SCAN [115]	4.003	64.14	2.13*	220 <i>i</i>	183	290	476
DFT-PBEsol [103]	3.98	63.25	1.79	201 <i>i</i>	178	288	465

*reported only for the tetragonal phase, which tends to exhibit band gaps 0.1-0.2 eV larger than the cubic phase

Applying this suite of metrics to BaTiO₃, we find that under n -type doping we populate the Ti d orbitals, shifting the configuration from d^0 to d^x where $0 < x < 1$. As the Ti d orbital occupation becomes nonzero, the orbital overlap decreases, reducing the strength of the covalent bond and the magnitude of the SOJT effect [116]. This reduction in orbital overlap is a gradual process, not taking place until surpassing a carrier density associated with modest electrical conductivity, in line with recent experiments [45, 46, 106]. Meanwhile, under p -type doping, we find that the states near the valence band edge do not participate in the covalent bond, and so the polar distortion persists more or less unaffected (if not slightly enhanced). This circumstance is much more difficult to achieve through chemical substitution or interstitial defects than electron doping, and so is unlikely to be realized in experiment, but the contrast with electron doping helps support this analysis and may lead to fruitful comparisons to other systems. In addition to the impact of doping on the orbital overlap (which we view as the dominant effect controlling the persistence of the polar distortion under doping), we observe a charge self-regulation effect driven by an increase in the band gap. This increase in energy difference $E^{(n)} - E^{(0)}$ (the denominator of the covalent bonding term in Equation 4.1) has a minimal effect on the magnitude of the SOJT effect but serves to

explain the organization of charge in the unit cell upon doping.

4.2 Materials and methods

4.2.1 BaTiO₃ as a model material

BaTiO₃ undergoes a series of ferroelectric transitions. Beginning with the high temperature cubic perovskite ($Pm\bar{3}m$) phase, the Ti cation off-centers upon cooling to produce the tetragonal ($P4mm$), orthorhombic ($Amm2$), and rhombohedral ($R3m$) phases in succession [117]. In this study, we are concerned with the mechanisms which lift inversion symmetry, so we focus exclusively on the cubic-tetragonal transition which exhibits the fewest atomic displacements necessary to break parity. This transition occurs at ≈ 400 K. The tetragonal-orthorhombic transition occurs around 280 K, which makes the tetragonal $P4mm$ phase stable at room temperature.

4.2.2 Density functional theory

We perform first principles calculations using density functional theory (DFT) as implemented in the Vienna Ab initio Simulation Package (VASP) [118, 119] using a planewave basis set with a 800 eV energy cutoff. The Perdew-Burke-Ernzerhof (PBE) exchange-correlation functional revised for solids (PBEsol) [34] was used, along with the projector-augmented wave (PAW) method to treat the separation of the core and valence electrons [120]. Lattice parameters, volume, and atomic positions were relaxed in various combinations (as specified), such that the forces and stress tensor were converged to 5×10^{-4} eV \AA^{-1} and 2×10^{-3} eV \AA^{-2} , respectively. The Brillouin zone was sampled using a $7 \times 7 \times 7$ Monkhorst-Pack mesh and the tetrahedron method. Using these

parameters, we find our relaxed structures are in good agreement with both experiment and other choices of density functionals (Table 4.1).

4.2.3 Carrier doping

We assess the evolution of the inversion symmetry-breaking transition with changes in carrier type and density by artificially varying the number of electrons in the system (by fractional amounts) while applying a compensating background charge to retain charge neutrality. This approach allows us to change the orbital filling without introduction of additional chemical species that would introduce secondary atomic distortions. This also allows us to simulate dilute levels of doping without increasing the size of the unit cell, as would be required for modeling heterovalent substitution of A^{3+} or A^{1+} cations on the Ba sublattice [39]. Though not without its drawbacks, this method is frequently used to simulate doped FEs [36, 40, 107], and shown to provide accurate structure-property descriptions. Carrier concentrations were examined in a range from 0.05 electrons (or holes) per unit cell (u.c.) to 0.20 electrons (or holes) per u.c., which correspond to $7.9 \times 10^{20} \text{ cm}^{-3}$ and $3.2 \times 10^{21} \text{ cm}^{-3}$ respectively.

4.2.4 Lattice dynamics

Phonon frequencies were computed using the frozen phonon method after relaxation of the atomic positions, cell shape (*i.e.*, the degree of tetragonality), and sometimes volume (as indicated below). Phonon calculations were prepared and analyzed using the PHONOPY software package [121]. We find that our calculations of the Γ -centered phonon modes are consistent with both previous computational and experimental studies (Table 4.1), and that their dispersions throughout the Brillouin zone match previous studies (Figure 4.1). Evidence of each of the 3 successive ferroelectric

phase transitions is apparent when assessing the lattice dynamical stability of the cubic phase. However, we focus on the dynamics of the Slater mode at Γ (circled in Figure 4.1), which drives the transition to the tetragonal phase. Evidence of the stabilization of soft modes throughout the Brillouin zone under each phase transition is provided in Appendix B.

Force constants are computed using density functional perturbation theory, generating an $3N \times 3N$ matrix where N is the number of atoms in the unit cell. Force constants are calculated using the expression

$$\phi_{ij} = \frac{\delta^2 E}{\delta u_i \delta u_j}, \quad (4.2)$$

where E is total energy, $\delta u_{i,j}$ are small atomic displacements ($\approx 0.015 \text{ \AA}$), and ϕ_{ij} are the resulting force constants for the relative motion of atoms i and j . The elements of the force constant matrix on the diagonal ($i = j$) are the self-force constants (SFC), corresponding to the second derivative of the energy with respect to the displacement of the atom. Thus a negative (positive) value of the SFC along the diagonal indicates an energy gain (cost) upon displacement of the atom. Off-diagonal elements ($i \neq j$) correspond to the energy derivative with respect to the relative motion of two different atoms, equivalent to an effective spring constant and termed the interatomic force constants (IFC). Because the motion of the atoms is relative to one another, δu_i and δu_j have opposite sign. Thus, a negative (positive) IFC indicates an energy cost (gain) when those atoms displace relative to one another.

4.2.5 Electronic structure

Our calculations of the electronic structure for $P4mm$ BaTiO₃ demonstrate the expected insulating behavior, featuring a valence band (dominated by O $2p$ orbitals) separated from a conduction band (dominated by Ti $3d$ states) by a band gap of about 1.8 eV (Figure 4.2). This is consistent with

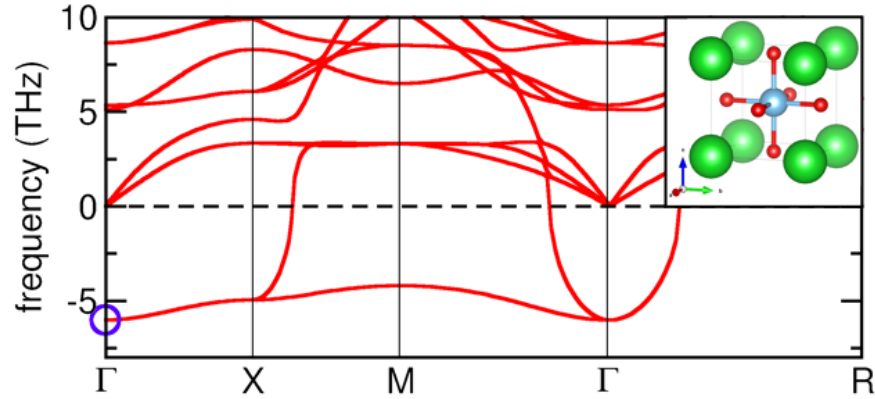


FIGURE 4.1: Phonon dispersions for cubic ($Pm\bar{3}m$) BaTiO_3 . The Slater mode, responsible for driving the ferroelectric transition to the tetragonal ($P4mm$) phase is circled. (inset) Unit cell for cubic BaTiO_3 . Green, blue, and red spheres correspond to Ba, Ti, and O atoms.

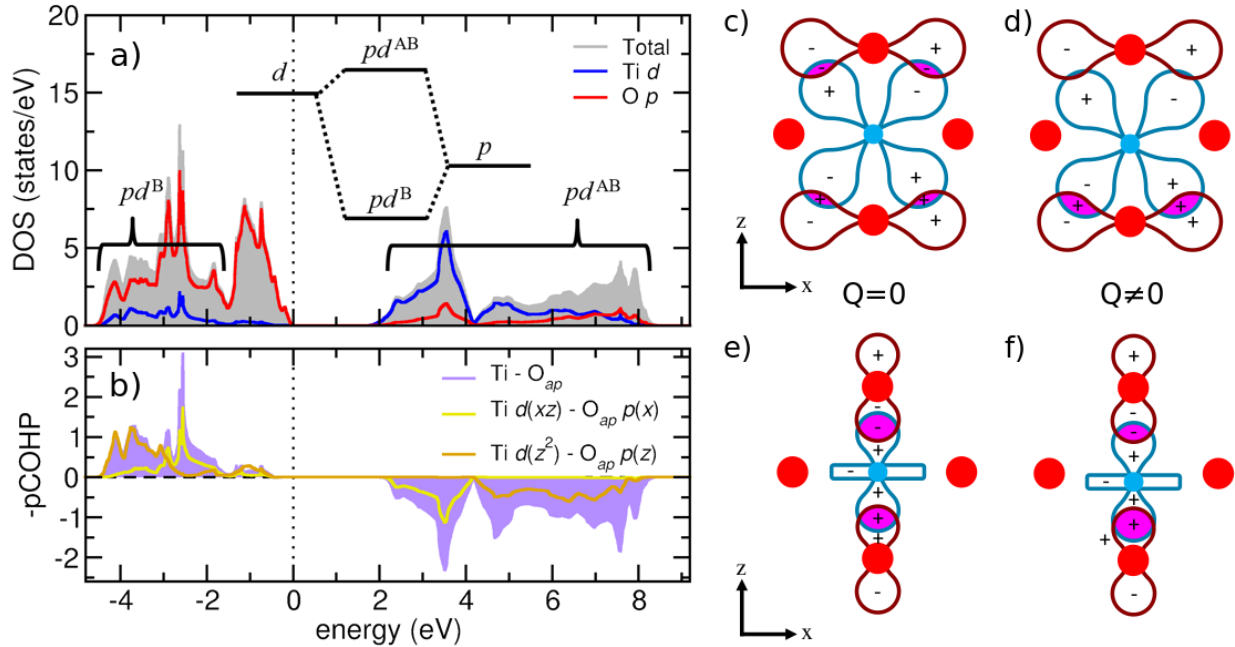


FIGURE 4.2: (a) Electronic density of states (DOS) for tetragonal BaTiO_3 with a molecular orbital diagram illustrating the covalent bonding between Ti and O. (b) Projected crystal orbital Hamiltonian population (pCOHP) for tetragonal BaTiO_3 . (c-f) Illustration of the enhanced overlap under polar distortion along the z axis driven by the SOJT effect, shown for both (c,d) π -bonding between Ti $d(xz/yz)$ and O $p(x/y)$ and (e,f) σ -bonding between Ti $d(z^2)$ and O (pz). In the cubic structure, (c,e), the net overlap is 0 by symmetry, but becomes nonzero after the distortion as shown in (d,f).

previous theoretical studies in that it underestimates the band gap by ≈ 1.4 eV (Table 4.1). Although we expect some pd hybridization from ligand-field theory, as found from the projected density-of-states (DOS) shown in Figure 4.2a, we further quantify this interaction by computing the crystal orbital Hamiltonian population (COHP). The COHP is determined by weighting the electronic density-of-states (DOS) by the Hamiltonian elements corresponding to orbital overlap, which we perform using the LOBSTER code [122–125]. The result is a method of energy partitioning the DOS into bonding, nonbonding, and antibonding regions. These are generally identified by plotting the COHP projected onto a particular atomic (or orbital) pair (pCOHP). The convention is to plot the negative pCOHP ($-p\text{COHP}$, which is unitless) so that bonding interactions are positive while antibonding interactions are negative. Figure 4.2 confirms our expectation and provides significantly more detail, allowing us to differentiate between π -bonding (overlap of Ti $d(xz)$ and $\text{O}_{ap}p(x)$, which drives the transition) and σ -bonding (Ti $d(z^2)$ and $\text{O}_{ap}p(z)$, also strengthened under the transition), which will be exploited below in our analysis.

Maximally localized Wannier functions represent an alternative route to quantifying changes in chemical bonding. Using the Wannier90 code [126], we compute the evolution in the real-space wavefunctions of BaTiO_3 under electron doping. In particular, we use the VASP-Wannier90 interface [127], choosing to project onto the O $2p$ and Ti $3d$ orbitals.

4.3 Results

4.3.1 Charge redistribution upon electron and hole doping

Here we focus on the bond between the Ti and O, described by the covalent bonding term in Equation 4.1, upon adding charge carriers into tetragonal BaTiO_3 . To track the charge associated

with a path in real-space between Ti and O, we use the Wigner-Seitz radius, defined as

$$r_s = [3/(4\pi n)]^{1/3}, \quad (4.3)$$

which corresponds to the radius of a sphere whose volume contains one electron of charge, obtained from our DFT charge density. Large values of r_s indicate low density regions, typically in interstitial sites between atoms where little chemical bonding occurs. Small values of r_s occur near atomic sites or along more covalent bonds. We prefer r_s to charge density in this analysis because r_s provides a rigorously defined method of attributing charge to a path in real space and allows us to quantitatively compare materials and doping configurations. Further evidence of the utility of this technique is provided in Appendix B.

Without any additional carriers in tetragonal BaTiO₃, we find a smaller peak along the shorter Ti-O bond (Figure 4.3a) than along the long bond, indicating stronger and weaker covalent bonding, respectively. This enhanced bonding of the shorter Ti-O bond is driven by orbital overlap (Fig. 4.2c-f) as described by the SOJT effect. Both σ and π bonds contribute here, though it is the π bond which dominates (due to the smaller energy difference between bonding states) and acts to stabilize the breaking of inversion symmetry by Ti off-centering. To understand how doping affects the charge distribution, we first plot Δr_s as a function of doping in tetragonal BaTiO₃ with the volume and atomic positions held constant. We keep fixed the Ti-O bond length to separate the role of dielectric screening from electronic screening. Here we find an asymmetry between electron and hole doping in terms of the changes in local bonding. Whereas under electron doping we find a clear increase in r_s (decrease in charge density) near Ti and decrease (increase in charge density) near O along both bonds, under hole doping the trend is much less continuous and appears to both occur

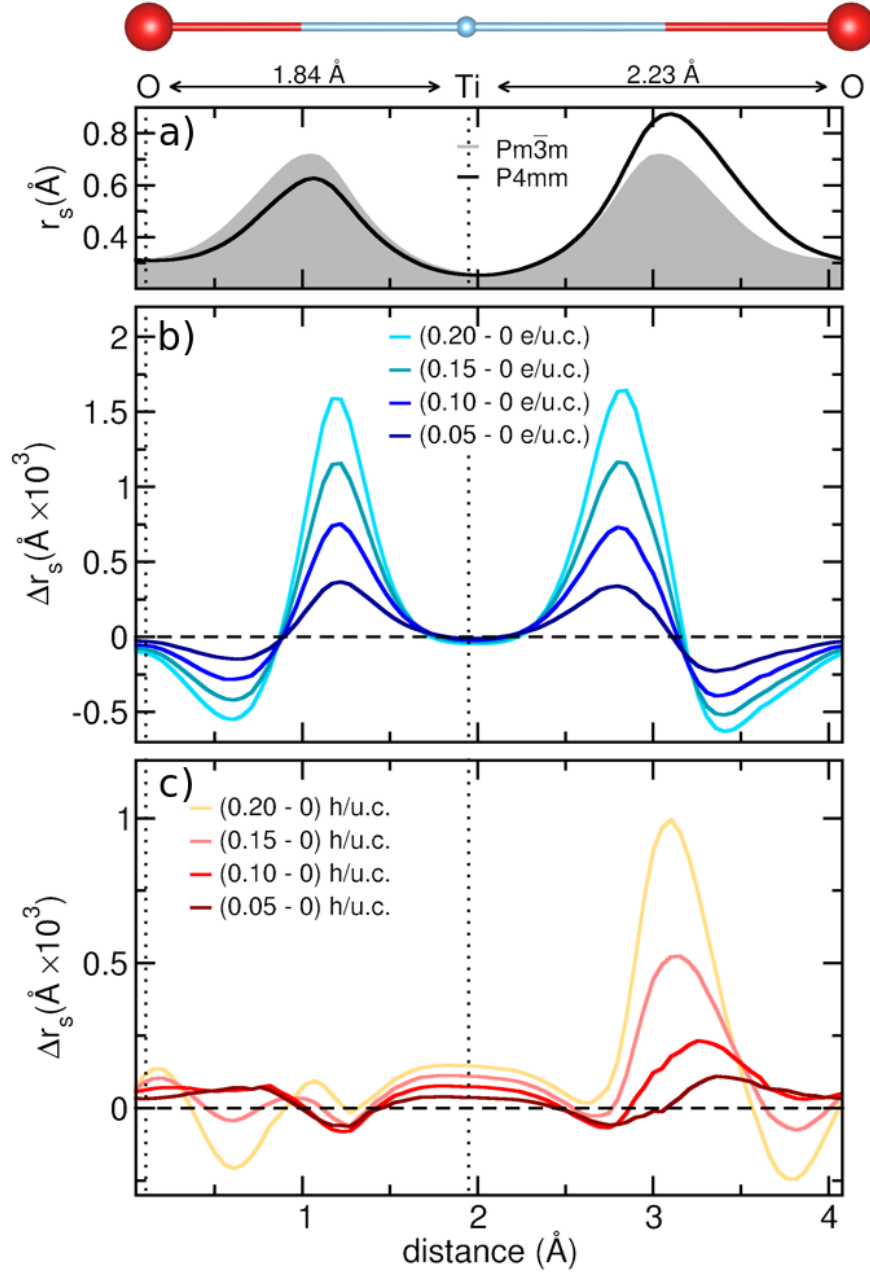


FIGURE 4.3: (a) Wigner-Seitz radius (r_s) calculated on a path through the center of the relaxed BaTiO_3 unit cell (cubic and tetragonal), along the axial Ti-O bond. The change in r_s along the same path in the tetragonal unit cell under (b) electron and (c) hole doping with the lattice parameters and atomic positions fixed to those of the relaxed (undoped) tetragonal unit cell.

only along the long Ti-O bond and with smaller magnitude ($\approx 1 \times 10^{-3} \text{Å}$ vs $\approx 1.5 \times 10^{-3} \text{Å}$). We attribute this difference in response to the difference in the bonding character of the dopant states (Fig. 4.2b). *n*-type doping immediately begins to populate anti-bonding states, directly impacting states related to the hybridization between Ti and O, while *p*-type doping initially empties non-bonding states, thus having a minimal effect on the sharing of electrons along the Ti-O bond.

In both cases, however, there appears to be a net motion of charge away from Ti and towards O. Although this might appear counter-intuitive, a similar transfer of charge has been proposed to occur upon doping oxide semiconductors; it is described as charge self-regulation [128]. The addition of electrons (holes) shifts the conduction band to higher energy (valence band; lower energy), causing the predominantly empty cation states to take on greater anti-bonding character while the filled anion states take on greater bonding character. Since the bonding states are filled and the anti-bonding states are only partially occupied, this results in an effective increase in the number of electrons associated with the anions. We appear to observe a similar effect; the addition of electrons (holes) into the Ti-dominated conduction band (O-dominated; valence band) results in a shift of electronic charge away from Ti and toward O. As mentioned above, however, the effect is more pronounced under electron doping, since *n*-type carriers immediately populate states that participate in the Ti-O bond whereas *p*-type carriers do not. If electrons and holes affect the Ti-O bond (the driving force behind the SOJT effect) in different ways, we should expect that the response of the polar distortion under electron and hole doping will be asymmetric as well.

4.3.2 Doping effects on the polar distortion

To evaluate the consequences of this charge distribution on the crystal structure, we consider both structural metrics and quantitative assessments of the driving force towards the polar distortion

itself. The evolution of the polar distortion under electron doping has been studied previously computationally and experimentally, finding that the high symmetry phase is stabilized with a carrier concentration of $\sim 1.7 \times 10^{21} \text{e/cm}^3$ (0.11 e/u.c.) [36, 46]. This contraindication between electron charge carriers and broken inversion symmetry is consistent with traditional frameworks describing the stabilization of polar modes via long-range Coulombic interactions. However, the traditional framework begins to break down when you compare the threshold for stabilization to the threshold for metallic conductivity [45, 46], achieved at $\sim 10^{20} \text{cm}^{-3}$ (as determined by the carrier concentration required to make $\delta\rho/\delta T > 0$). The experimental value aligns well with the Mott criterion for conductivity ($n_c^{1/3} a_0 \approx 0.25$), a carrier concentration of approximately $2.4 \times 10^{20} \text{cm}^{-3}$.

It appears that *n*-type dopants induce metallicity at a concentration one order of magnitude lower than that required to turn off the polar distortion. Attempts have been made to argue that “metallicity” is achieved prior to the necessary reduction in screening length [36], but this has been refuted by recent theoretical work [107]. In addition, a screening length argument fails to account for the differences under hole doping.

When doping with holes, the stabilization occurs much more gradually; counter-intuitively, the polar distortion is enhanced for small hole concentrations (Figure 4.4). This difference in behavior depending on the sign of the charge carriers has been observed via theoretical methods before [107], although to our knowledge never observed in experiment owing to the challenges in hole-doping BaTiO₃. If long-range, Coulomb-type interactions were the sole stabilizing mechanism in polar materials, we would expect a comparable carrier density to produce a similar screening effect, regardless of the sign of the charge. The divergent behavior of the two regimes (especially at low concentrations) indicates that the stabilizing effect of short-range off-centering mechanisms must

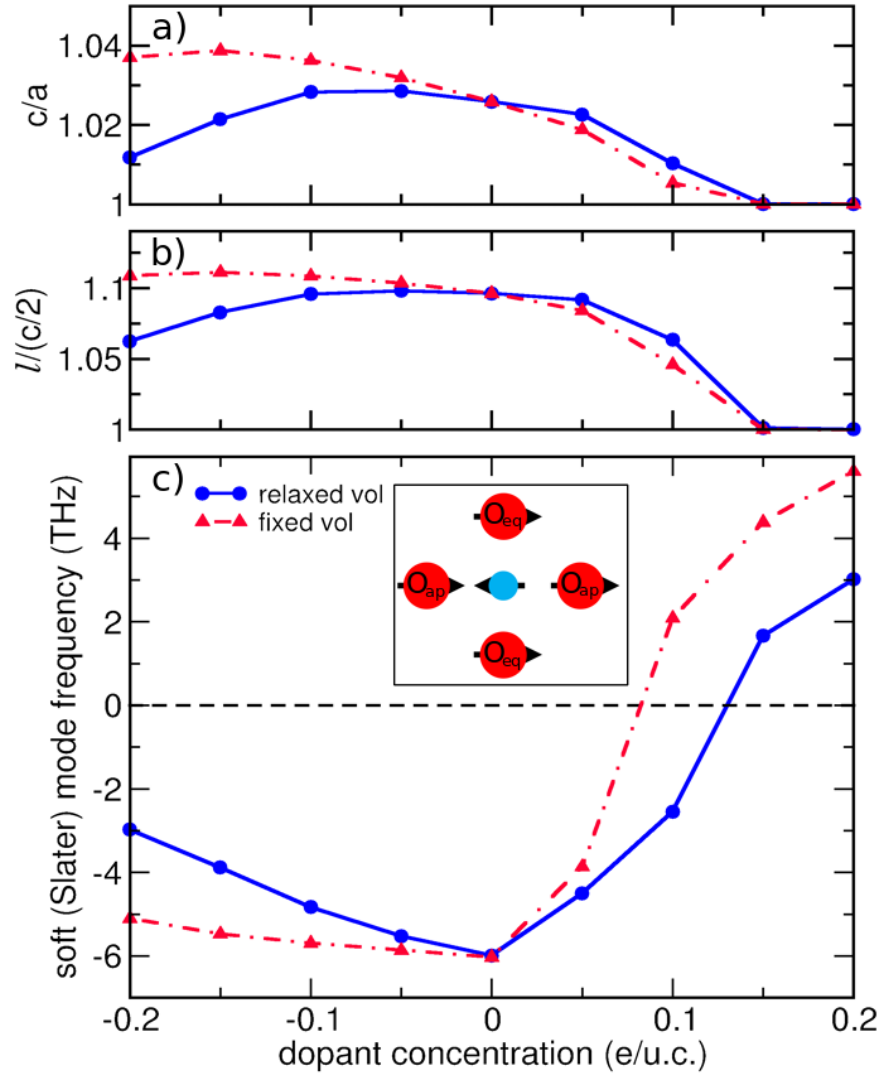


FIGURE 4.4: (a) The axial c/a ratio and (b) degree of polar distortion (given by the ratio of the long Ti-O (l) bond to half the lattice parameter along the c axis) of the relaxed tetragonal cell both fixed to the undoped volume and with the volume relaxed as a function of doping. (c) Slater mode (TO1) frequency as calculated for the high-symmetry cubic cell as a function of doping. (inset) Slater mode displacement pattern showing relative motion of Ti and the surrounding O anions.

also be accounted for, if not prioritized, when examining how metallicity and acentricity interact.

These results support the use of the SOJT effect as a framework for our analysis and provide preliminary insight into the impact of doping, as the magnitude of the polar distortion is closely related to the distortion magnitude Q from Equation 4.1. The sign of the coefficient of the second order term (the value in square brackets) determines whether this distortion is energetically favorable, resulting from the competition between covalent bonding and the rigidity of the lattice. If the distortion amplitude is greater than zero under doping then the covalent term remains dominant.

What microscopic mechanisms control this term? Using soft-mode theory, we can approximate the magnitude of the resulting driving force and identify the atoms that play the largest role in stabilizing the distortion. To that end, we next assess the lattice dynamical properties, focusing on the soft Slater mode. Consistent with previous work [8, 36, 65], we find that the cubic ($Pm\bar{3}m$) phase exhibits an unstable transverse optical phonon mode known as the Slater mode (Figure 4.1). The atomic distortion pattern for this phonon mode (inset to Figure 4.4c) breaks the symmetry elements required to drive the transition to the tetragonal phase ($P4mm$), and is dominated by the displacement of Ti and O atoms in opposite directions along one of the three crystallographic axes.

Under doping, the difference in the Slater mode response between electron and hole doping is again evident but not as stark as the evolution of the distortion magnitude itself (there is no enhancement of the instability under hole-doping). The fully relaxed structure in particular exhibits a surprisingly large shift in frequency under hole doping, but comparison with the fixed volume case reveals that this is largely due to volume effects. Hole (electron) doping reduces (increases) the volume, thereby disfavoring (favoring) the polar distortion. Focusing on the fixed volume case, we see that, as before, hole-doping has a muted effect on the soft mode, whereas electron doping rapidly

stabilizes the phonon mode. This corroborates our analysis of the relaxed tetragonal structure, confirming that the driving force for displacement responds differently to electron and hole doping.

There remains a subtle difference between the Slater mode evolution and the polar distortion magnitude (the Slater mode frequency increases monotonically under hole doping whereas $\ell/(c/2)$ increases then decreases) for which we do not have a conclusive explanation. However, we hypothesize that this arises from changes in the DOS at the valence band edge. In the cubic structure, all oxygen sites are related by symmetry and their p -states are degenerate. Thus in the cubic phase p -type doping affects all O sites equally, whereas in the tetragonal phase the O_{ap} sites are shifted to lower energy (see Appendix B) so that p -type doping initially affects only the O_{eq} sites, which do not participate in the short bond supporting the SOJT effect. The polar distortion itself also enhances the degree of covalency, further shifting the bonding states to lower energy. These shifts in energy are small, but may be enough to subtly alter the impact of hole doping in the cubic and tetragonal structures.

In order to more directly probe the changing dynamical contributions from individual atoms, we also analyzed the force constants under both electron and hole doping (as shown in Appendix B). We found that the force constants describing the local off-centering of Ti and relative displacement of Ti and O_{ap} (apical O atom) saw the greatest change, rapidly stiffening under electron doping and hardening more gradually under hole doping, following the pattern in Figure 4.1. This result supports our assessment that changes in the local environment of Ti and O_{ap} are responsible for the stabilization of the cubic structure as well as the differences in the response of the structure under electron and hole doping.

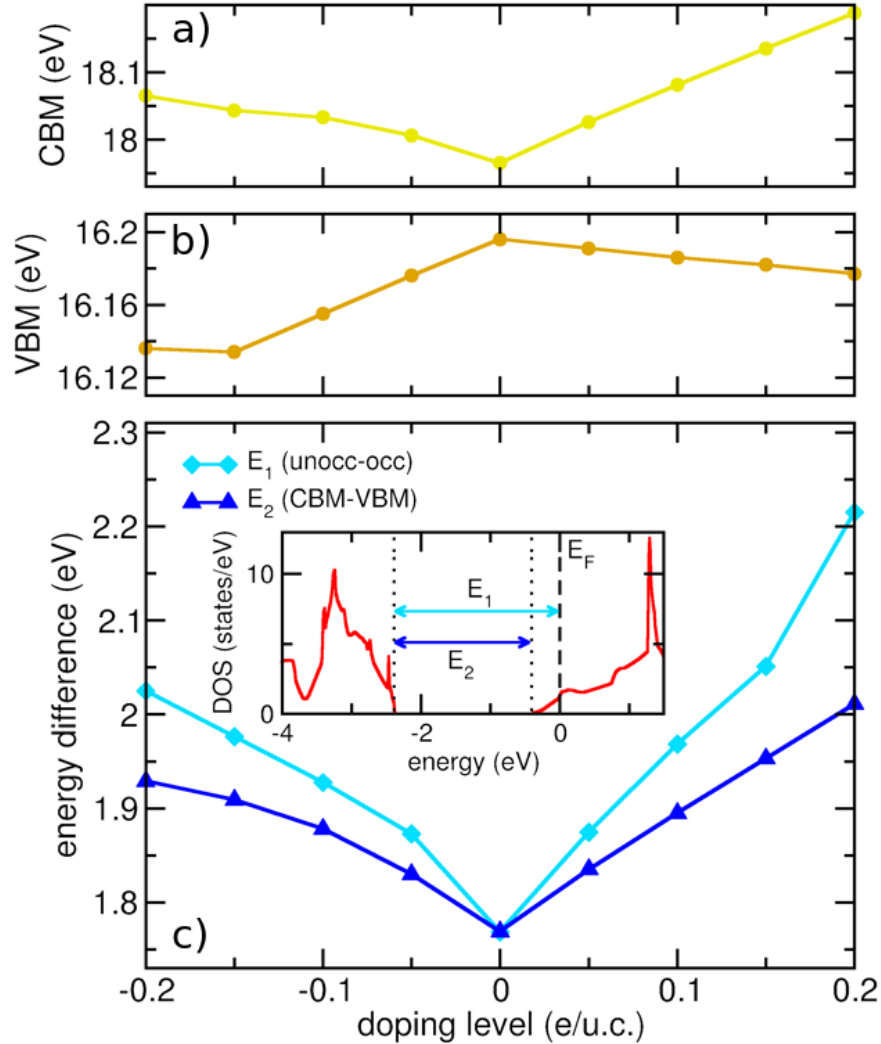


FIGURE 4.5: Evolution of (a) conduction band minimum (CBM), (b) valence band maximum (VBM), and (c) energy differences E_1 and E_2 (defined in the inset) under electron and hole doping in tetragonal BaTiO₃, with lattice parameters and atomic positions held constant.

4.3.3 Electronic structure effects

The band structure of pristine BaTiO₃ exhibits a valence band consisting of O-dominated bonding states and a conduction band of Ti-dominated antibonding states, separated by a gap of about 1.9 eV at the DFT-GGA level. The energies of these states appear in the denominator of the covalent bonding term in Equation 4.1, specifically the energy difference between the ground and

excited states.

We next assess the evolution of this energy difference by calculating the electronic structure of BaTiO₃ under doping (Figure 4.5). To account for changes in the absolute energy caused by altering the number of charge carriers (and the corresponding neutralizing background charge) the listed band edge energies are determined relative to the O 2*s* semicore-level states. Here we find evidence of the charge self-regulation effect. The conduction band edge shifts to higher energy under electron doping, while the valence band edge shifts to lower energy under hole doping (Figure 4.5). This shift in the energy of Ti and O states, respectively, leads to a change in character of the resulting molecular orbitals. The antibonding states acquire greater Ti character while the bonding states take on greater O character. Since the bonding states are much more occupied than the antibonding states, charge effectively moves from the Ti site to the ligands, consistent with our observations of Δr_s (Figure 4.3).

We also plot the energy difference between the highest occupied O *p*-states and lowest unoccupied Ti *d*-states (E_1) as well as the band gap (E_2) under doping (Figure 4.5). We find a significant increase in both differences under both doping directions, which can largely be attributed to charge-self-regulation. The changes in E_1 and E_2 exhibit a slight asymmetry in favor of electron doping, but the response under hole doping comes closer to mirroring the electron case than in any of our other metrics. This energy shift induced by doping drives an increase in the denominator of the covalent bonding term in Equation 4.1 (indicated by E_1), reducing the stabilization of the polar displacement by mixing ground and excited states (represented in the numerator). However, the magnitude of this effect is small if not negligible, since the energy-difference increase under hole doping does not seem to significantly impact the magnitude of the polar distortion (Figure 4.2). The underestimation of the band gap by DFT at the GGA level also artificially magnifies the relative

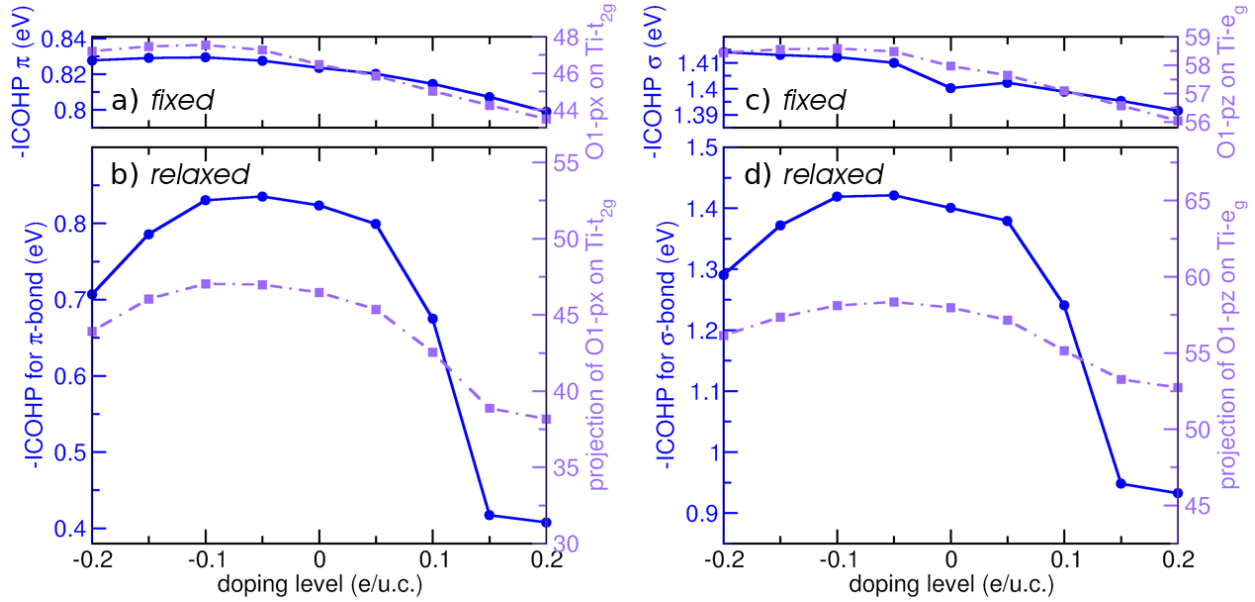


FIGURE 4.6: Carrier doping leads to similar responses in both the integration of the projected crystal orbital Hamiltonian population (ICOHP) up to the Fermi level (circles) and the projection of O_{ap} Wannier functions onto Ti states (squares). Both ICOHP and projection Wannier function data are shown for (a,b) π - and (c,d) σ -bonds. The evolution of each quantity under doping is shown for (a,c) the unit cell fixed to the undoped relaxed tetragonal phase and for (b,d) the fully relaxed unit cells (which initially are tetragonal but become cubic under sufficient electron doping).

change in energy differences, further reducing the expected impact of changing energy differences on the polar instability in experimental BaTiO_3 samples. Meanwhile, as will be shown below, the changes in the magnitude of the polar distortion correlate well with changes in the degree of orbital overlap, implying that the covalent bonding term in Equation 4.1 overwhelmingly drives the off-centering mechanism.

4.3.4 Quantifying changes in bonding

To examine changes in covalent bonding more directly, we performed crystal orbital Hamiltonian population (COHP) analysis of the Ti-O_{ap} interaction under doping. Since the COHP is calculated using elements of the Hamiltonian corresponding to orbital overlaps, it gives us an approximation of the $\langle 0 | \mathcal{H}^{(1)} | n \rangle$ term in Equation 4.1. Although the focus of this work is on the Ti-O_{ap} interaction, we

find evidence that the Ti-O_{eq} interaction is non-negligible, and may be worthy of further study (as shown in Appendix B). By comparing the COHP to the electronic DOS, we find the Ti-dominated conduction band (CB) is indeed primarily antibonding character, while the O-dominated valence band (VB) is primarily bonding character, consistent with previous work [129] and expected from our molecular orbital analysis (Figure 4.2).

Upon electron doping into the CB, we find that even dilute concentrations result in the population of antibonding states. The presence of antibonding states below the Fermi level is an unfavorable configuration, already indicating that electron doping may disrupt the stability of the Ti-O_{ap} bond. At the VB edge, the O-states at the top of the band are of nonbonding character, predominately associated with the equatorial O atoms, meaning that a much greater concentration of holes is required to shift the Fermi level into the bonding regime than electrons were required to enter the antibonding regime. This analysis provides some insight as to the asymmetrical response of BaTiO₃ under electron and hole doping, as it appears that hole-doped states (at least initially) do not affect the Ti-O interaction. We can discern this behavior more quantitatively by plotting the integrated COHP, summarizing the bonding character by integrating the -pCOHP from low energy up to the Fermi level (Figure 4.6). We perform this analysis for both the π -bond between Ti $d(xz)$ and O_{ap} $p(x)$ orbitals (related by symmetry to a second π -bond between $d(xy)$ and $p(y)$ orbitals) and the σ -bond between Ti $d(z^2)$ and O_{ap} $p(z)$ orbitals, which represent the $n = 1$ and $n = 2$ interactions in Equation 4.1 respectively. Note that because we are plotting overlap data for only one of the π -bonds contributing to the distortion, one should apply a factor of two prior to comparison with the σ -bond data.

Under electron doping, we find the anticipated decrease in bonding character while under hole doping there appears to be a slight strengthening of the Ti-O_{ap} bond, consistent with the

enhancement of the distortion shown in Figure 4.4. This broad trend is found in both the π and σ bonds, but the two exhibit notable differences when the volume and positions are held constant to the relaxed, undoped tetragonal phase. Low levels of n -type doping appear to slightly enhance the orbital overlap for the σ -bond when the structure is fixed to the undoped tetragonal phase. This change fails to match any of our previous observations, nor does it align with the response of the π -bond orbital overlap, which immediately and continuously decreases. The σ -bond overlap under p -type doping (again in the fixed case) also increases more starkly and more monotonically than our other metrics for changes in bonding. These differences imply that the π -bond exerts a much greater influence on the SOJT effect and the resulting distortion than the σ -bond. This interpretation is corroborated by the energy level of these two interactions, as well as their change in magnitude when relaxed under doping. π -antibonding states form the conduction band edge, and are the first to be occupied by electron doping. σ -antibonding states are located at higher energy, reducing the strength of the interaction and moving them beyond the range of n -type doping. The magnitude of the change in overlap for the two types of bonds under doping of relaxed structure appears similar, but recall that we only show overlap data for one of two identical π -bonds making the overall change much greater in both absolute and proportional terms.

Thus, we conclude that electron doping shifts the Fermi level into an antibonding regime, which immediately disrupts the Ti-O_{ap} bond and reduces the orbital interaction term in Equation 4.1. Hole-doping initially has little to no effect as the Fermi level passes through nonbonding states until eventually the bonding states are impacted and the covalent bond is again weakened. In particular, we note that, while both σ and π bonds contribute, it is the π -bonding interaction which exerts the dominant influence on the polar distortion, a conclusion consistent with previous work on the SOJT effect in BaTiO₃ [116].

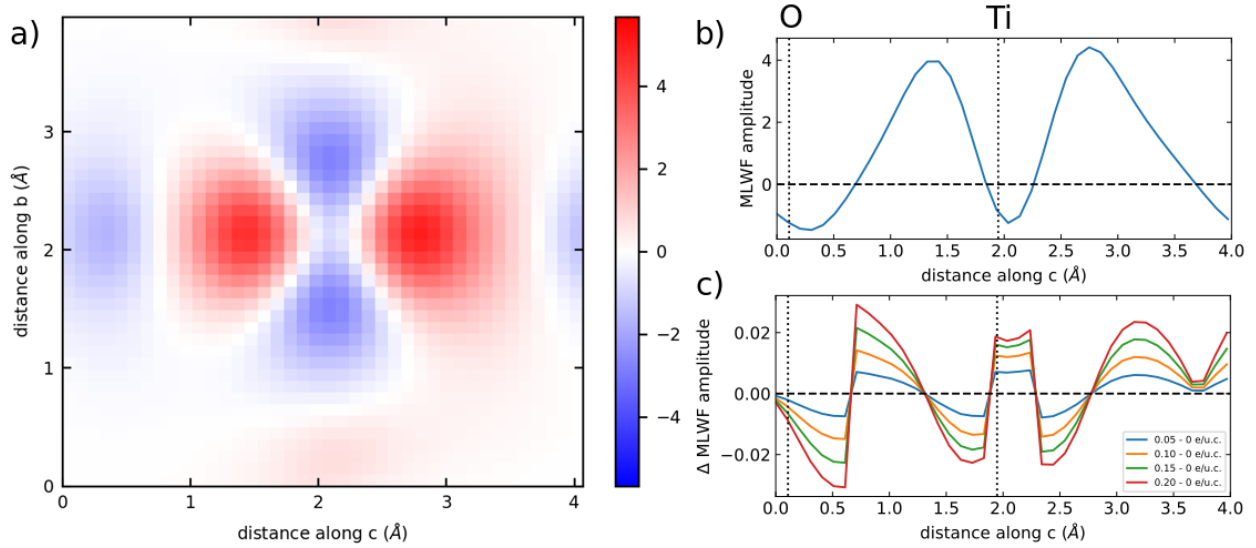


FIGURE 4.7: (a) Two-dimensional slice of the MLWF associated with the Ti- $d(z^2)$ orbital, taken perpendicular to the a axis so that it cuts through the Ti and apical oxygen bond. (b) MLWF amplitude along the apical Ti-O bond. (c) Change in MLWF amplitude as a function of electron doping taken along the same path through the apical Ti-O bond.

4.3.5 Maximally localized Wannier functions (MLWFs)

We next examine changes in the amplitude of the maximally localized Wannier functions (MLWFs), frequently used to describe chemical bonding, focusing on the MLWF associated with the Ti- $d(z^2)$ orbital (primarily responsible for bonding with the O_{ap} - $p(z)$ orbital). Although we previously established that the π -bond contributes more to the off-centering of Ti, it is non-trivial to determine a path in real space for analyzing the movement of charge along the π -bonds. We have instead chosen an orbital that lies along the polar axis as an example for comparing to our previous observations of charge redistribution using r_s as a metric.

Similar to the r_s evolution, we find a shift of the amplitude away from the Ti center and towards O_{ap} , as indicated by shifts in the lobes of the orbital as well as increases in amplitude near oxygen, especially along the long bond (Figure 4.7c). Similar shifts are observed in the MLWF associated with the O_{ap} - $p(z)$ orbital, as shown in Appendix B. As with the Δr_s analysis, we attribute this

response in part to the charge self-regulation effect.

We can also use MLWFs to approximate the strength of the Ti-O_{ap} covalent bond by computing the projection of MLWFs associated with different O *p* orbitals onto Ti states. As with the ICOHP analysis, we do this for both the π (O_{ap} *p*(*x*) projected onto Ti-*e_g* states) and σ (O_{ap} *p*(*z*) projected onto Ti-*t_{2g}* states) interactions (Figure 4.6). An example of this projection process is shown in Appendix B. Similar to the evolution of the ICOHP, we find that electron doping decreases the magnitude of the projection, while hole doping has a small enhancing effect. This result supports our previous conclusions regarding the impact of doping on the bonding between Ti and the apical oxygen. Unlike the ICOHP data, the trends for the σ and π bonds are almost identical, supporting the idea that σ -bonding plays a key role in stabilizing the distortion. However, the same considerations regarding the absolute and proportional magnitudes of the changes under doping still apply, as these are both much greater for the π -bonding interactions. The differences between the ICOHP data and MLWF projections can likely be attributed to a subtle difference in what they measure; ICOHP data uses the Hamiltonian element associated with orbital overlap to weight the DOS by bonding character, while the MLWF projection is more directly an estimate of the degree of hybridization. Despite their differences, the two methods agree with our main findings; the strength of the covalent bond is the primary driving force behind local off-centering, and the change in this bond strength under doping directly controls the change in off-centering via the SOJT effect.

4.4 Discussion

Each of the metrics employed herein demonstrates the same asymmetric response under electron and hole doping, consistent with the assessment that short-range interactions must be responsible

(or at least essential) for local off-centering. Such an assessment is further corroborated by the growing evidence that polar distortions persist beyond a modest threshold for conductivity [45, 46, 106]. A similar observation was made in Ref. [107], not just for BaTiO_3 , but for a variety of ferroelectrics, where the short-range interaction was explained using a new concept introduced by the authors as “meta-screening.” We restate the concept here succinctly: When a perovskite-structured ferroelectric is doped with free charge carriers, those free charges rapidly distribute themselves in opposition to the local dipole moment generated by Ti off-centering relative to the oxygen octahedron. The reorganization of free charges so as to generate a depolarizing field leads to a high concentration of negative charge carriers near the positively charged Ti^{4+} ion, and a similar concentration of positive charge carriers near the negatively charged O^{2-} ions.

While this description of the “meta-screening” phenomenon appears to correctly predict the surprising persistence of polar distortions in a metallic environment, we propose an alternative and more intuitive approach. Rather than construct new physics, we explain the same phenomenon by considering the impact of additional charge carriers on the strength of the covalent bonding between the atoms responsible for driving the local distortion (namely Ti and O in BaTiO_3). Conveniently, the covalent bonding approach also predicts an increased concentration of electrons along the shortened Ti-O bond near the positively charged Ti side of the dipole and a corresponding decrease along the long bond closer to the distorted oxygen octahedron (Figure 4.3).

This approach draws on previous analysis of the dominant (and entirely short-range) nature of the SOJT effect. In developing the theory, Polinger et al. observed that while force constants can be decomposed into a strongly negative, long-range component and a strongly positive, short-range component, the SOJT effect accounts for more than 70% of the so-called “long-range” contribution [116]. Under this framework, the persistence of local off-centering despite metallic screening is

unsurprising. Even with a small level of n -type carriers, the polar distortion enhances covalency, reducing the energy of the occupied O_{ap} p orbitals in accordance with Equation 4.1.

Why, then, does electron doping eventually favor the high symmetry state? This occurs through the disruption of the SOJT mechanism. As previously noted in the literature, d^1 perovskites are incapable of exhibiting SOJT-driven distortions due to the differing spin multiplicity between ground and excited states, reducing $\langle 0 | \mathcal{H}^{(1)} | n \rangle$ to zero [40, 64, 116]. As electrons are added to the d^0 system in BaTiO₃, the nonzero occupancy of the Ti d orbitals reduces the magnitude of the enhanced covalency. This eventually changes the sign of the second-order term in Equation 4.1 as the rigidity of the lattice (i.e. the elastic, non-vibronic coupling term $\langle 0 | \mathcal{H}^{(2)} | 0 \rangle$) dominates and the high symmetry structure is restored.

In addition to returning to more familiar physical arguments, we believe the SOJT approach allows us to more precisely accommodate the difference in responses upon electron and hole doping. Electron doping begins to populate antibonding states at the conduction band edge, leading to charge self-regulation, increased band gap, and most importantly disrupting the orbital overlap related to the π bonding between Ti and O, eventually quenching the polar distortion. Hole doping initially populates only non-bonding states, and although we see a modest charge self-regulation effect and opening of the band gap here as well, the strength of the covalent bond is relatively unchanged if not slightly enhanced. This leads to a slight increase in the polar distortion which only wanes once the p -type carriers reach a sufficient concentration to depopulate bonding states and decrease the strength of the bond.

Finally, whereas the “meta-screening” model provides a sufficient explanation for doped conventional ferroelectrics, we expect that modeling the effect of charge carriers on bonding interactions will be more transferable to discussions of other contexts where the polar distortion mechanism

is decoupled from the presence of free charges (e.g., improper ferroelectrics or polar metals). Our analysis is consistent with the so-called “weak-coupling hypothesis” proposed in Ref. [10], which has been extensively utilized to understand the stability of polar metals. Under electron doping, conductivity and asymmetry are fundamentally contraindicated, as electrons fill states directly coupled to the off-centering mechanism (namely, the SOJT effect). Under hole doping, initially the dopants enter non-bonding states, leaving the distortion mostly unperturbed until the Fermi level shifts into the bonding states.

4.5 Conclusion

We find an asymmetry in the response of the polar distortion in BaTiO_3 under electron and hole doping. We proposed a set of analyses to understand the microscopic origin of the behavior and, consistent with previous work, find short-range interactions play a central role in governing local ion off-centering when polarization and metallicity coexist. Specifically, the short range interaction responsible for driving local off-centering (namely, the SOJT) is disrupted by electrostatic doping via reduction in the magnitude of orbital overlap by changing the occupation of states involved in the covalent bond. Electrostatic doping also results in charge self-regulation, shifting charge from the B site to the ligands and opening the band gap. Coulombic interactions are still critical to the stabilization of long-range coordinated off-centering in proper ferroelectrics, however the local off-centering is primarily stabilized by short-range chemical bonding as described by the SOJT effect. Lastly, although much of the analysis in this work is particular to SOJT-driven doped ferroelectrics, we anticipate that the metrics developed here may apply well to other materials. In particular, we expect the concept to extend to polar metals, perhaps allowing for greater clarity in comparing and contrasting the different mechanisms for combining polar symmetry and metallicity more generally.

Chapter 5: Transforming a strain-stabilized ferroelectric into an intrinsic polar metal via photodoping

This work was done in collaboration with the following individuals: Dr. Alon Ron (Tel-Aviv University) and Mr. Omar Mehio and Dr. David Hsieh (California Institute of Technology), who came to us with the second-harmonic generation, reflectivity, and transport data under optical excitation and assisted in writing the manuscript. Dr. Kevah Ahadi and Dr. Susanne Stemmer (University of California, Santa Barbara) grew the thin films and aided in the interpretation of the results. Dr. Danilo Puggioni (Northwestern University) provided guidance in deriving the theoretical photodoping approximation and constructing a model for the polar distortion.

5.1 Introduction

Metallic conductivity and long range polar order were long thought to be fundamentally incompatible, due to the screening of electric dipoles by free charges. However in 1965, Anderson and Blount suggested their possible coexistence [1], a suggestion later validated by Shi et al. in the 2013 synthesis of the first polar metal, LiOsO_3 [2]. Rondinelli and Puggioni subsequently built on Anderson and Blount's work to successfully design and implement an operational principle termed

the “weak-coupling hypothesis” [10], namely that in order for metallic conductivity to coexist with coordinated polar displacements the two orders must be decoupled from one another, to identify and discover polar metals.

Consequently, polar metals are distinct from doped ferroelectrics, particularly second-order Jahn-Teller (SOJT) driven proper ferroelectrics such as BaTiO_3 . Both may exhibit regimes that combine modest conductivity with acentricity [2, 107]. Polar metals, however, obey the weak-coupling hypothesis while the polar order in doped ferroelectrics tends to be highly sensitive to and fundamentally incompatible with additional charge carriers at the Fermi level. In the example of SOJT-driven compounds, additional electrons occupy empty d -orbitals in the conduction band, perturbing the electronic states responsible for covalent bonding between the transition metal site and the surrounding ligands. This disrupts the driving force for the polar order, thereby violating the weak-coupling hypothesis, and under sufficient doping leads to stabilization of the high symmetry structure, as was demonstrated in BaTiO_3 [103].

Unstrained EuTiO_3 is an antiferromagnetic (AFM) paraelectric (PE) insulator. However, Fennie et al. calculated that a large (2.9%) compressive strain will drive EuTiO_3 into a SOJT-driven polar phase exhibiting both ferroelectric (FE) and ferromagnetic (FM) character [130]. This compressive strain was too large to achieve experimentally, leading Lee et al. to extend their work to include tensile strain [131]. Through a combination of first principles calculations and experiments, they showed that the application of tensile epitaxial strain greater than 1% likewise drives EuTiO_3 into a multiferroic FE-FM insulating state with transition temperatures of approximately 250 K (FE) and 4.2 K (FM).

Both transitions—from AFM to FM and from PE to FE—are driven by the position of the Ti ion inside its octahedral O cage. In the unstrained case, EuTiO_3 has a cubic $Pm\bar{3}m$ structure and

the undistorted cage provides a single well potential for the Ti with its minima at the center of the cage. When tensile epitaxial strain is applied, the lower symmetry and elongated in-plane lattice parameters transform the single well potential into a double well. The Ti ion seeks to optimize its local bonding environment and displaces away from the center of the unit cell into either of the two degenerate minima, providing the conditions for a FE phase with $mm2$ point symmetry [131]. This off-centering perturbs a fine balance between AFM and FM exchange interactions. In the centrosymmetric unstrained case, the combined effect of third nearest neighbor AFM interaction (Eu-O-Ti-O-Eu across the cube diagonal) and an extra superexchange (Eu-Ti-Eu) contribution to the nearest neighbors exchange work to favor AFM ordering [132]. The strain-modulated displacement of the Ti ion away from the center of the unit cell alters these contributions and allows nearest-neighbor interactions to dominate, turning tensile strained EuTiO_3 into a ferromagnet.

The strain-induced polar phase of EuTiO_3 is an attractive candidate for exploring the intersection of metallic conductivity and broken inversion symmetry. Although, as a SOJT-driven FE, we would expect additional charge carriers to fundamentally disrupt the polar order, EuTiO_3 may be distinguished from prototypical SOJT-driven ferroelectrics by the presence of Eu f -states which both form the valence band and lead to FM ordering.

Here, we probe the interplay between additional charge carriers and the polar order of strain-induced multiferroic EuTiO_3 using experimental and computational methods. We find that the strained samples exhibit a ferroelectric-like reduction in its polar distortion amplitude under low levels of chemical doping and photodoping, consistent with predictions from DFT. At higher levels of doping, however, we find that this reduction in polar amplitude saturates at $\sim 84\%$ of its original magnitude, indicating a decoupling of the structural distortion from the Fermi level akin to a polar metal. Photodoping acts to transform a ferroelectric into a polar metal. We offer several hypotheses

to explain this change in character, including a possible change in the driving mechanism of the displacive distortion induced via photodoping.

5.2 Methods

To investigate and isolate the competing influences of strain and additional charge carriers, we use first principles calculations. Our first principles calculations use density functional theory (DFT) as implemented in the Vienna Ab initio Simulation Package (VASP) [118, 119] using a planewave basis set with a 750 eV energy cutoff and the Perdew-Burke-Ernzerhof (PBE) exchange-correlation functional revised for solids (PBEsol) [34]. The projector-augmented wave (PAW) method is used to treat the separation of the core and valence electrons [120] with Eu $5s$, $5p$, $4f$ and $6s$ electrons, Ti $3p$, $3d$ and $4s$ electrons and O $2s$ and $2p$ electrons treated as valence states. In all calculations an on-site Coulomb interaction ($+U$) was added to the Eu $4f$ orbitals with $U = 6.2$ eV and exchange $J = 1.0$ eV as implemented in the Liechtenstein *et al.* method [133]. In all cases, Eu-Eu spin interactions are ferromagnetic (FM) because EuTiO₃ on DyScO₃ is expected to undergo an antiferromagnetic (AFM) to FM transition at low temperature [134]. Treatment with AFM ordering for key calculations did not significantly impact the results. Lattice parameters, volume, and atomic positions were relaxed such that the forces were converged to 5×10^{-4} eV Å⁻¹. The relaxed lattice parameters of the cubic ($Pm\bar{3}m$) structure (3.88 Å) underestimate the experimental lattice parameters (3.905 Å) by about 0.5%.

The Brillouin zone was sampled using an $11 \times 11 \times 11$ Γ -centered mesh and the tetrahedron method for undoped relaxations and density of states calculations. Phonons for doped and undoped structures were computed using density functional perturbation theory and Gaussian smearing (0.05 eV width). In order to approximate photodoping, we first performed static self-consistent

calculations with added electrons compensated by a neutralizing background charge (using Gaussian smearing). For each concentration level we then constrained the occupancy of the valence band edge at each k-point to compensate for the additional electrons in the conduction band, preserving charge neutrality as well as guaranteeing equal electron and hole concentrations. These fixed partial occupancies were then used to relax the out of plane lattice parameter and compute lattice dynamical properties.

5.3 Results

5.3.1 Theoretical prediction of a doped ferroelectric

We begin by computing the in-plane tensile strain dependence of the Γ -point phonon modes while relaxing the out-of-plane lattice parameter. The model structure initially exhibits cubic ($Pm\bar{3}m$) symmetry, but immediately adopts $P4/mmm$ symmetry as tetragonality is enforced by the in-plane strain. Consistent with previous experimental and theoretical work [130,135], a polar instability arises as indicated by softening of the transverse optical TO1 mode at the Γ -point (Figure 5.1a). The resulting two-fold degenerate polar mode exhibits predominantly Slater character [136], which is enhanced by strain as shown in Appendix C. To investigate whether strain modulates the mixing between modes of different character—namely the TO1 (Slater) and TO2 (Last) modes—we also plotted the evolution of the TO2 mode. However, the strain-dependent dispersion of the TO2 mode is largely decoupled from changes in the TO1 mode. In addition, the frequency difference between the modes does not directly correspond to changes in mode character (Appendix C). Allowing the structure to distort following the displacement pattern of the TO1 mode results in a structure with the anticipated $mm2$ point group symmetry observed in experiment [131].

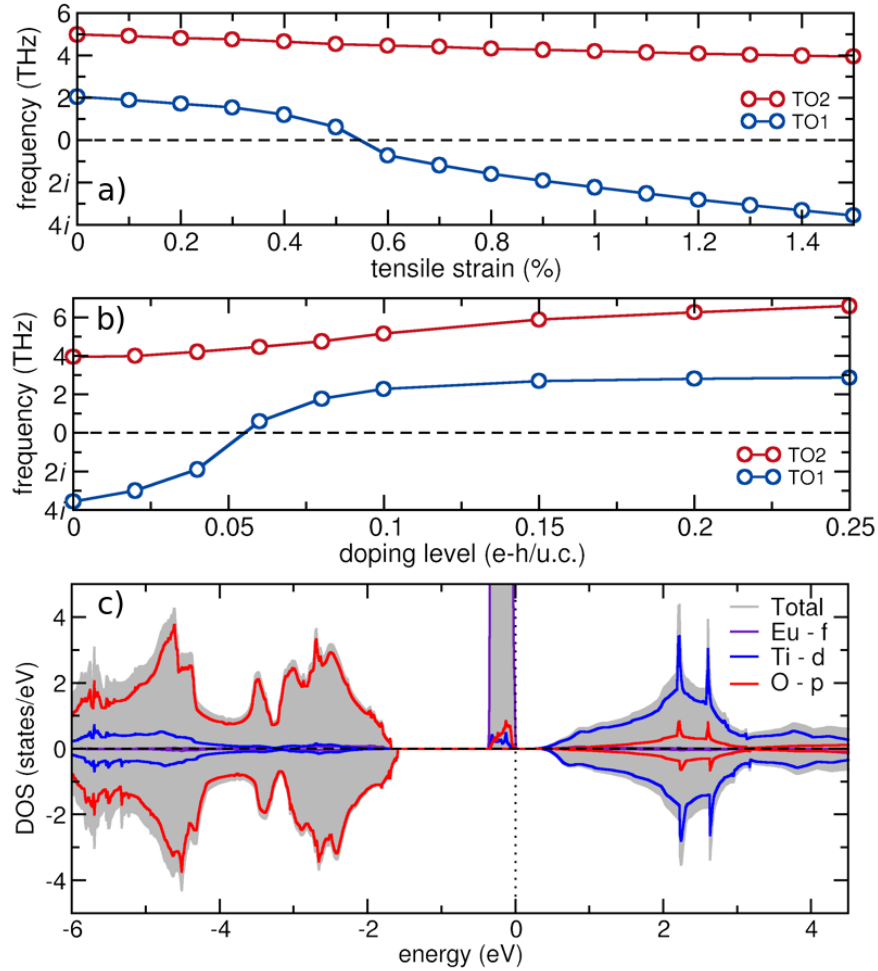


FIGURE 5.1: a,b) Evolution of the Γ -centered TO1 and TO2 phonon modes for centrosymmetric tetragonal $P4/mmm$ EuTiO_3 upon (a) increasing the in-plane tensile strain relative to the relaxed cubic lattice parameters and (b) increasing the photodoped-carrier concentration at 1.5% strain. (c) Electronic density of states (DOS) for $P4/mmm$ EuTiO_3 at 1.5% strain.

We next examine the evolution of the polar distortion under photodoping at 1.5% tensile strain (3.946 \AA), which is within the FE region of the previously calculated strain phase diagram [130,135] and nearly equivalent to the experimental pseudocubic lattice parameter of DyScO_3 (3.944 \AA). The soft TO1 mode initially persists under photodoping before quickly stabilizing at a dopant concentration of approximately 0.06 electrons per unit cell (e/u.c.) or $\approx 10^{21} \text{ cm}^{-3}$ (Figure 5.1b). This stabilization of the high symmetry phase matches our expectation of doped FEs. The nonzero

occupancy of the Ti d -orbitals, which form the conduction band (Figure 5.1c), disrupts the Ti-O covalent bonding which drives local off-centering via the SOJT effect [64, 103]. As with our observations under strain, whereas the TO1 mode undergoes significant changes, the TO2 mode is relatively unperturbed. This is consistent with their displacement patterns, since the TO1 (Slater) mode is dominated by Ti displacing relative to the oxygen octahedron while in the TO2 (Last) mode, Ti and O displace in the same direction and therefore are not driven by Ti-O bonding [4]. Similar calculations with electron doping alone led to a nearly identical critical concentration (see Appendix C), indicating electrons in the conduction band are responsible for impeding the polar distortion (as opposed to the holes in the valence band), again in line with expectations for a SOJT-drive FE.

5.3.2 Experimental characterization of persistent polarization

We also pursued experimental chemical and optical doping strategies. Substitution of Eu with Sm was performed following the example of Ahadi et al. [137]. The substitution results in static electronic occupation of the Ti t_{2g} orbitals thereby driving an insulator-to-metal transition (Figure 5.2). Previously, the metallic $\text{Eu}_{1-x}\text{Sm}_x\text{TiO}_3$ films were deposited on $(\text{LaAlO}_3)_{0.3}(\text{Sr}_2\text{TaAlO}_6)_{0.7}$ (LSAT), where the epitaxial strain is compressive so the film was not in a FE state. Here, we grew $\text{Eu}_{1-x}\text{Sm}_x\text{TiO}_3$ 20 nm thin films with $x = 0$ (undoped) and $x = 0.015$ (doped) by oxide molecular beam epitaxy on DyScO_3 substrates. Growth conditions are described in Ref. [138]. The metallic properties of the doped sample were characterized by resistivity and Hall effect measurements, using the Van Der Pauw configuration, in a ^4He cryostat in magnetic fields between -0.6 and 0.6 T.

The FE order is noncentrosymmetric for which a typical probe is optical second harmonic generation (SHG) [139]. SHG measurements were performed by shining 1.5 eV photons from a

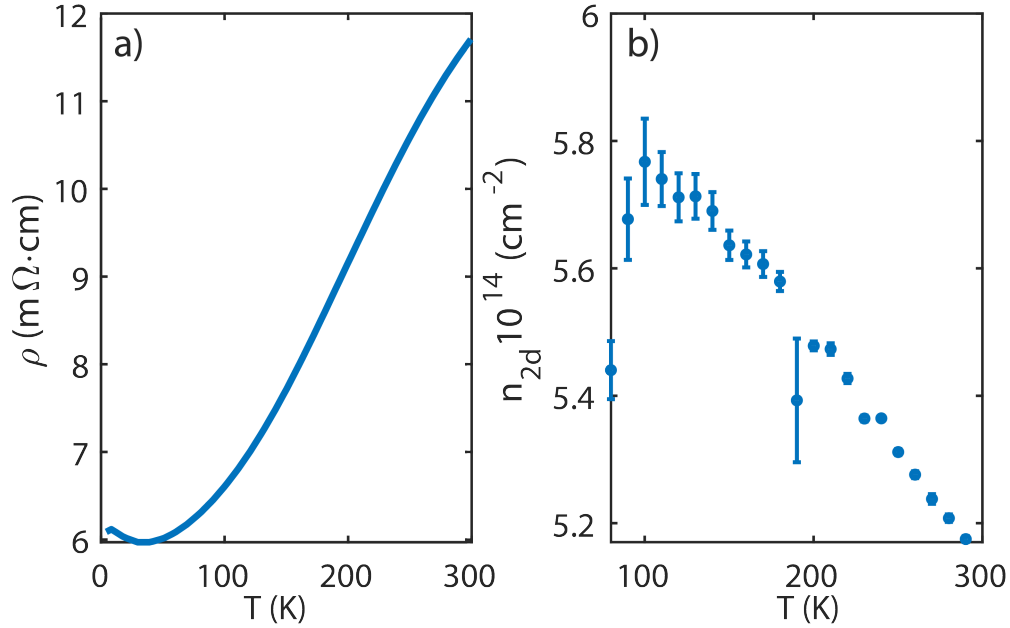


FIGURE 5.2: Electrical characterization of the doped sample. (a) Resistivity as function of temperature. The behavior is metallic down to 4.2 K. A small upturn in resistivity at low temperatures is associated with strengthening of the FE order. (b) 2D carrier density inferred from the slope of the Hall effect taken at magnetic fields between -0.6 and 0.6 T.

100 KHz Ti:Sapphire amplifier at an oblique angle of 10° relative to the sample surface with S- or P-polarization. The reflected beam at 1.5 eV was filtered out using color filters and the second harmonic at an energy of 3 eV was analyzed by rotating a linear polarizer. All data were acquired at 80 K (below the FE transition temperature [131]). Figure 5.3(a) shows the SHG intensity obtained from the doped film as function of the analyzer angle. For both P and S polarization configurations a strong SHG signal in agreement with point group $mm2$ is observed, indicative of the polar nature of the film. This is consistent with our first principles results, which indicate that this level of Sm doping ($x = 0.015$) should be well below the critical threshold for stabilizing the centrosymmetric structure ($x \sim 0.06$). For comparison, a similar measurement was performed on an unstrained film grown on an LSAT substrate (triangles on the same plot) and shows the absence of polar order in agreement with reference [131].

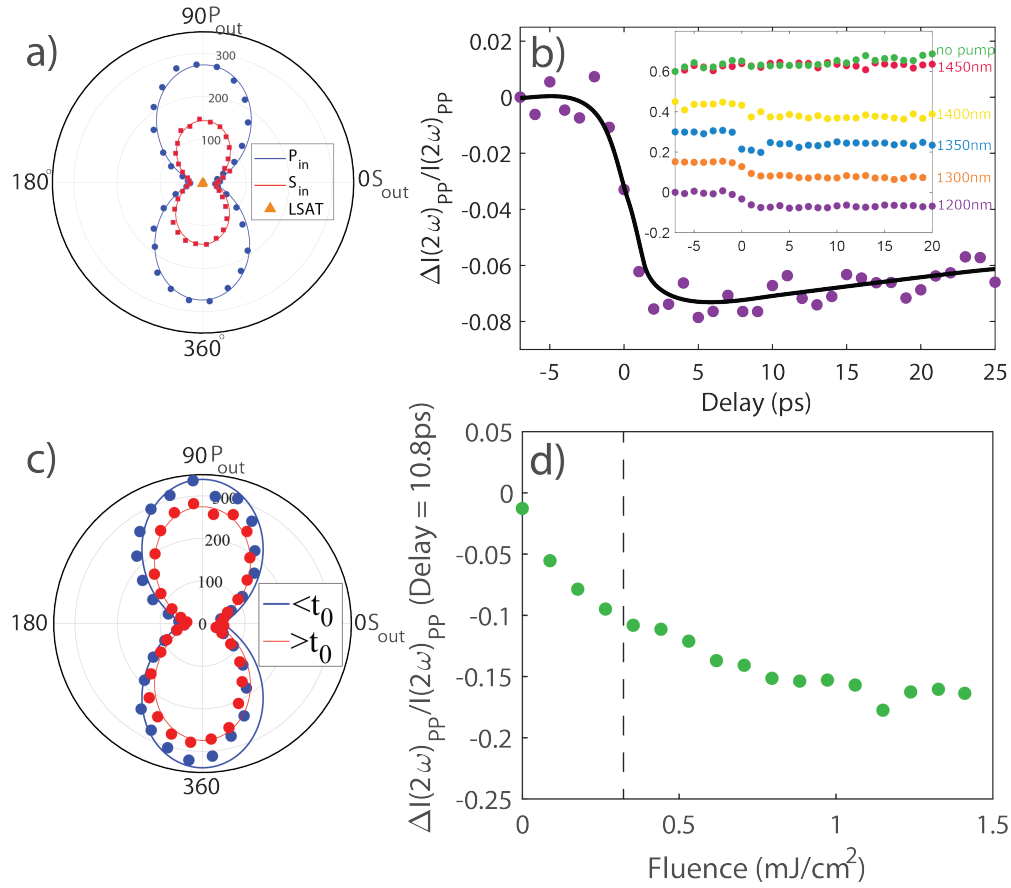


FIGURE 5.3: (a) SHG intensity as function of analyzer angle for the doped sample shown for two input polarization geometries. The triangles near zero intensity (center of the figure) are measurements on a centrosymmetric - nonpolar film grown on LSAT. (b) SHG intensity as function of time delay relative to the pump pulse for 1200 nm (1 eV) excitation. Other wavelengths are shown in the inset. (c) Polar plots in the P_{in} geometry as before and after the pump pulse excitation at 1200 nm. (d) Fluence dependence of the SHG intensity ~ 10 ps after the pump pulse excitation at 1200 nm. The dashed line represents the fluence at which the photodoping equals the threshold for stabilization of the nonpolar phase found in our calculations (0.06e/u.c).

To achieve higher doping levels than possible through chemical doping, we also performed a time-resolved SHG-probe photodoping experiment on a tensile strained EuTiO_3 sample grown on DyScO_3 . The SHG signal was collected as function of delay time relative to a pump pulse excitation from an optical parametric amplifier. The optical band gap of EuTiO_3 is ~ 0.9 eV (1378 nm) [90]. As shown in Figure 5.3b, when the pump and probe pulses synchronously overlap on the sample surface (delay = 0) a drop in the SHG signal is observed only for photon energies which exceed

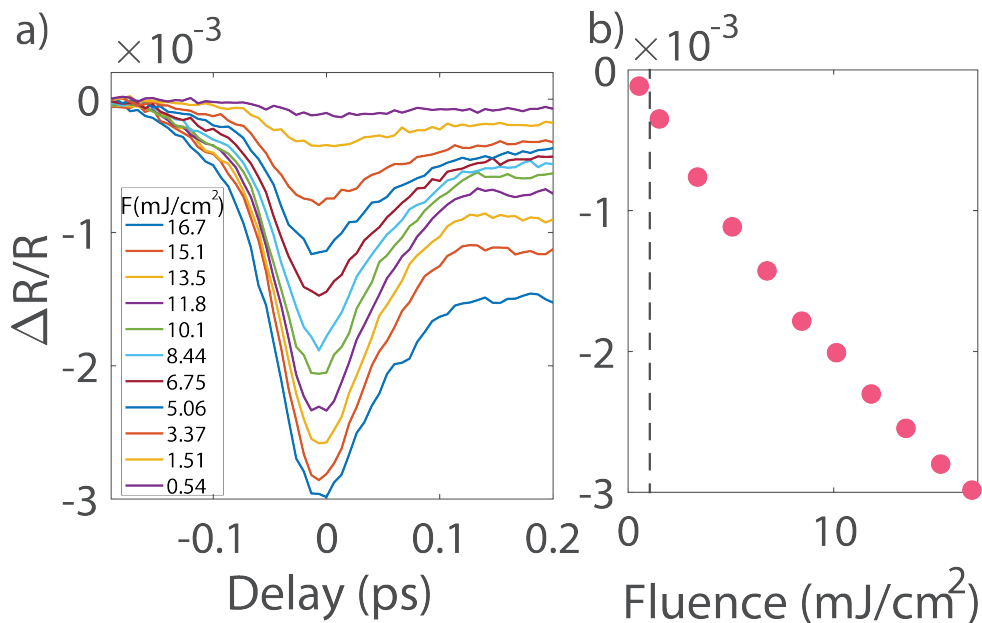


FIGURE 5.4: (a) Linear pump probe reflectivity at 80 K as function of pump fluence with wavelength of 1200 nm (1 eV). (b) Reflectivity signal at the minima of the pump probe traces shown in (a), the dashed line marks the saturation fluence value for SHG.

the energy gap. This drop is then followed by a slow (many picosecond long) relaxation time. Figure 5.3c shows SHG anisotropy plots before and after the pump excitation with 1 eV photon energy. The weakening of the SHG signal does not change the symmetry of the film and indicates that the FE order is weakened but not completely quenched. In an attempt to fully quench the FE order by photodoping, we increase the pump pulse fluence well beyond the threshold predicted by DFT ($x \sim 0.06$ marked by a dashed line) while keeping the photon energy constant to 1 eV, as shown in Figure 5.3d.

In contrast with the DFT results, we find the SHG signal saturates at the higher end of the fluence range (Figure 5.3d). Saturation in optical experiments is expected when the laser excitation is strong enough to either deplete the band from which electrons are excited or completely fill the band to which they are transferred, in our case the Eu 4*f* band near the fermi energy or the Ti 3*d* bands above the gap. This is known as photo-bleaching and is the physical principle standing in the

basis of stimulated emission depletion microscopy [140]. In case of full quenching of the FE order, one should expect the SHG signal to saturate to zero in this regime. Since the signal saturates to $\sim -16\%$ of its equilibrium value, we find the broken-inversion symmetry persists and should be stabilized, by an alternative non-SOJT mechanism.

In order to test whether a bleaching mechanism is at play, we perform linear optical pump-probe reflectivity measurements on the same undoped EuTiO_3 sample as a function of pump fluence with pump photon energy of 1 eV, namely the same conditions used in the SHG experiment. As shown in Figure 5.4a, following the pump-pulse excitation, a drop in the reflectivity of the probe beam is observed followed by a ~ 100 fs recovery to a lower value than in equilibrium. Figure 5.4b shows the reflectivity dynamics as a function of pump fluence. The reflectivity response to the pump excitation grows monotonically with fluence, as can be seen by the increasing magnitude of the pump probe signal. Moreover, the signal remains in the linear-response regime even for fluences far greater than those used in the SHG experiment, as seen in Figure 5.4b. As the same pump conditions were used for both the SHG and reflectivity experiments, we deduce that the origin for the saturation in the former is not due to photo bleaching as it should have caused a saturation in both experiments.

A simple explanation for the decrease in SHG signal as a result of the pump pulse is laser-induced heating. Since the measurements were performed at 80 K, well below the FE transition temperature (250 K), an increase in temperature will result in decreasing the signal. While consistent with our wavelength dependent measurement (Figure 5.3a, inset) showing a decrease of the SHG signal only above the energy gap of EuTiO_3 , it is inconsistent with our saturating fluence dependence. If heating caused the reduction of the FE order, saturation would have been expected only for complete quenching of the order due to heating above the transition temperature and not

to the finite $\sim 16\%$, similar to ultrafast demagnetization observed in ferromagnets heated by a pump pulse above their Curie temperature [141]. Any saturation to a nonzero value is therefore caused by some other mechanism, namely, the occupation of Ti t_{2g} states responsible for SOJT effect driving the distortion.

The DFT prediction of high symmetry stabilization under photodoping stands in stark contrast with the experimental evidence of persistent polar order ($\sim 84\%$ of the undoped distortion magnitude) despite carriers concentrations well beyond the 10^{21} cm^{-3} threshold predicted by DFT. Surprisingly, EuTiO_3 on DyScO_3 appears to change character under photodoping. Initially, the material behaves like a doped SOJT-driven ferroelectric as new charge carriers correspondingly reduce the magnitude of the polar distortion. Yet under increased photodoping, this reduction saturates to the point that the structural distortion appears fully decoupled from the Fermi level, a behavior associated with polar metals. What causes this change in character and why do our first principles models miss the interaction?

5.4 Discussion

With regard to our simulations, we note that the assumptions of a uniform distribution of dopants and long-range cooperative displacements are likely not realized in experiment. This observation leads us to propose several hypotheses which may explain the observed change in character. First, it has been shown that even relatively low concentrations of free charge carriers are sufficient to screen long-range Coulombic interactions in ferroelectrics [13]. In the absence of these interactions, the impetus for dipoles to align with one another decreases, allowing for the formation of nanodomains. Inversion symmetry is still broken locally over the laser probe spot size and the SOJT effect persists. Thus, the SHG response is finite and may still display $mm2$ symmetry. Such nanodomains have

been observed in isoelectronic and isostructural SrTiO₃ [142]. Furthermore, EuTiO₃ itself has been shown to exhibit several nearly degenerate polymorphs in the unstrained case, many of which remain close in energy under strain [135]. Thus one possible explanation is that the shallow energy surface of EuTiO₃ facilitates the formation of nanodomains which persist despite screening sufficient to prevent long-range ordering. However, nanodomain scenarios are unlikely since the probe diameter used is 25 microns and the effects from the much smaller nanodomains are expected to average out over our probe size.

We also suspect that doping could occur inhomogeneously within the film. This was previously observed in BaTiO₃ powders, where doping with oxygen vacancies led to the formation of two competing phases: one polar and insulating and the other centrosymmetric and metallic [143]. If a similarly inhomogeneous distribution of free charge occurred in EuTiO₃, the most highly doped regions would recover centrosymmetry as predicted in Figure 5.1 while the less doped regions would persist and exhibit *mm2* symmetry. This may seem unlikely since photodoping is typically considered a homogeneous process. However, even in undoped EuTiO₃ on DyScO₃ there is evidence of inhomogeneity in the magnetic domain structure [144]. Although the FM phase is expected to be favored energetically, paramagnetic (PM) regions persist below the magnetic ordering temperature. Our SHG measurements occur well above the magnetic ordering temperature, but it has been shown that the structural distortion (which occurs at higher temperature) and magnetic ground state are fundamentally linked in EuTiO₃ [130, 134]. Therefore, a complex microstructure present prior to photodoping may facilitate an inhomogeneous charge distribution.

A final, and perhaps most likely, possibility is that photodoping promotes octahedral rotations in EuTiO₃ [145], which in turn could stabilize an improper polar distortion involving the Eu *A*-site. The origin for such *A*-site displacements is then geometric and therefore is resilient to photodoping

in similarity to the polar metal LiOsO_3 [11]. This hypothesis would fully account for the change in character. The polar distortion of EuTiO_3 on DyScO_3 would evolve from the SOJT-driven mechanism of a proper FE (sensitive to additional charge carriers) to a geometric improper polar metal-like mechanism (decoupled from changes at the Fermi level).

5.5 Conclusion

We presented a theoretical and experimental investigation of the evolution of the polar order in EuTiO_3 as a function of chemical doping and photodoping. It was found that at intermediate doping levels of 0.015 e/u.c. a polar metallic state could be stabilized within similar doping levels of other oxide based systems [85]. We further showed via SHG measurements that EuTiO_3 on DyScO_3 undergoes a change in character under photodoping, initially exhibiting a suppression of the polar order associated with doped FEs before saturating at higher doping levels in contrast with what is predicted by first principles calculations. We suggested several hypotheses for the origin of this transition from FE to polar metallic behavior and encourage further study of this metallic multiferroic.

Chapter 6: Designing an anti-Ruddlesden-Popper polar metal

6.1 Introduction

Polar metals combine properties that were previously thought to be contraindicated, namely metallic conductivity and broken inversion symmetry. Since the first unambiguous polar distortion in a metal was reported in LiOsO_3 in 2013 [2], the number of predicted and synthesized polar metals has steadily increased [14], encouraged by the discovery of a variety of useful properties, including unconventional superconductivity [19–23], giant non-linear optical response [16], skyrmions [146], and topological features [16]. The known polar metals follow a design principle known as the weak-coupling hypothesis, which states that the Fermi level and inversion-lifting mechanism should be decoupled in order for the metallic conductivity and polar distortions to coexist [10]. TiGaO_3 has been presented as a candidate material to violate the weak-coupling principle [12], but it is unlikely to be realized in experiment due to its large decomposition enthalpy (see Chapter 3).

Even as the number of predicted and synthesized polar metals increases, observation of a symmetry-lowering phase transition in a metal remains rare. LiOsO_3 and $\text{Pb}_2\text{CoOsO}_6$ are two of the few examples [2, 80]. So-called ‘distortive polar metals’ (see Chapter 3) are desirable because they present an opportunity to tune the formation of polar domains, which can be exploited for

device applications.

In the pursuit of designing a new class of distortive polar metals, with an eye toward testing the weak-coupling hypothesis, we focus on anti-structure types. Anti-structure types are derived from their more conventional analogs by swapping the positions of the cations and anions. Anti-perovskites are a well-studied example, with a unit cell featuring a cation octahedron surrounding an isolated anion in the center of the cell (opposite to the traditional perovskite structure type, which features TX_6 octahedra, where T=transition metal and X=anion, usually O or S. Perovskite and anti-perovskite examples are shown in Figure 6.1). Anti-perovskites are known to host numerous polar metals [79, 147–150] (though none are known to be distortive). The $n = 1$ layered anti-perovskite (anti-Ruddlesden-Popper) is much less well-studied. Analogous to the perovskite-derived Ruddlesden-Popper structure, there are only a handful of experimentally synthesized anti-Ruddlesden-Popper (Anti-RP) compounds [151–156], at least three of which are predicted to be ferroelectric: $\text{Ba}_4\text{Sb}_2\text{O}$, $\text{Ba}_4\text{As}_2\text{O}$, and $\text{Eu}_4\text{Sb}_2\text{O}$. Each compound is expected to undergo a phase transition from $I4/mmm$ to $I4mm$, driven by off-centering of O relative to the A-site octahedron [157, 158].

The presence of a polar instability (as well as known polar metals among anti-perovskites) make anti-RPs an attractive structure type for polar metals design. Although many structure types are known to exhibit inversion-lifting distortions—including, notably, perovskites [8, 73, 85]—the prevalence of transition metal cations in anti-structure types provides a pathway to unite polar distortions with metallic conductivity. In addition, whereas the O off-centering in Anti-RP FEs relative to the cation octahedron is attributed to a geometric mechanism rather than a bonding one, it seems possible to design a polar metallic Anti-RP compound such that the displacing ions contribute at the Fermi level, potentially testing the weak-coupling hypothesis.

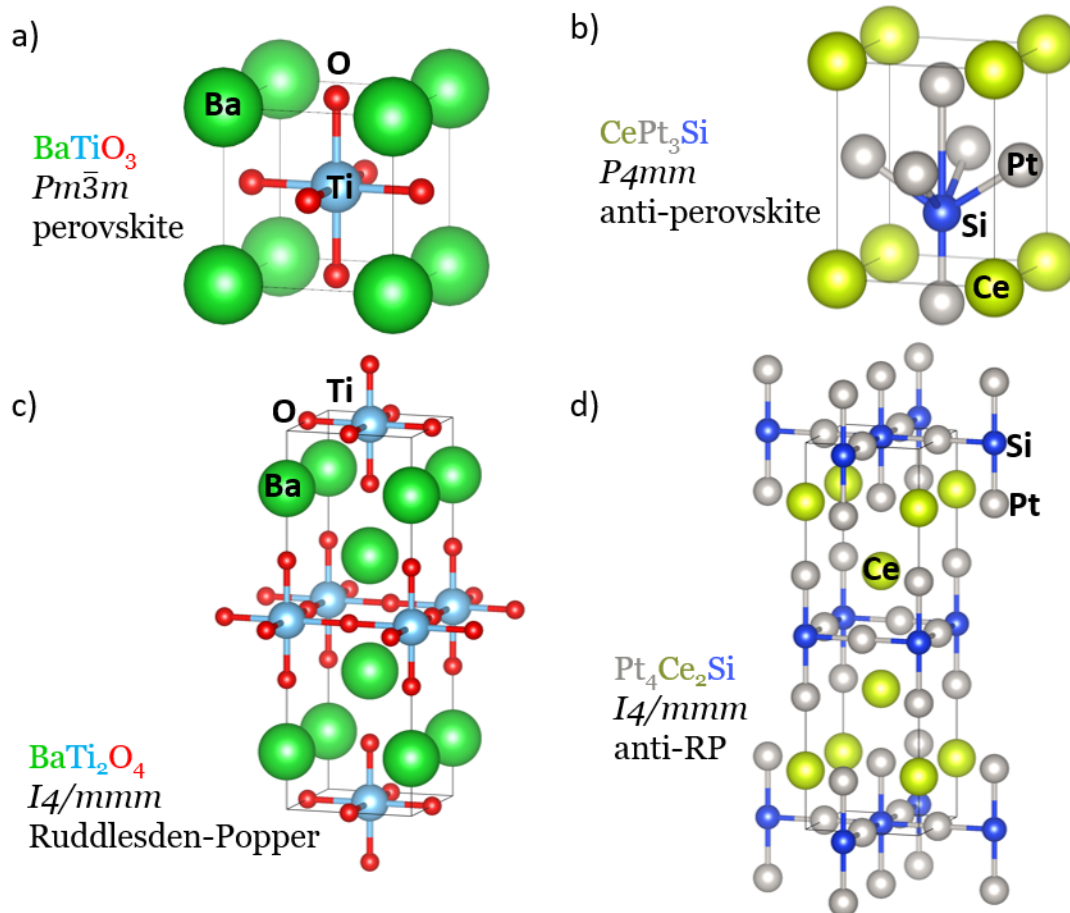


FIGURE 6.1: Comparison of (a) perovskite and (c) Ruddlesden-Popper structures with their (b,d) anti-structure analogs. In (a,c) the transition metal (Ti) is surrounded by an anion octahedron (O), whereas in (b,d) the anion (Si) is surrounded by a transition metal octahedron (Pt).

We identify two promising design routes for realization of an anti-RP polar metal: (1) A-site substitution of known anti-RPs with 5d transition metals or rare earth cations and (2) $n = 1$ layered analogs of known anti-perovskite polar metals. For strategy (1), 5d transition metals are desirable because of their relatively large ionic radius, enabling us to mimic the effective tolerance factor of the known Ba-based compounds. For the same purpose, we will restrict the B-site to As and P, rather than including larger pnictides. Among the 5d transition metals, we choose those that will lead to partial occupancy of the d -orbital manifold, assuming the B-site adopts a 3- valence state and O a 2- valence state, as observed in the known ferroelectric anti-RPs [157, 158]. This

leaves the A-site in a 2+ configuration (at least on average, we will discuss the possibility of charge disproportionation later). In order to achieve partial occupancy, we select 5d transition metals from W to Au. Rare earth cations are also good candidates both due to their large ionic radius and potential for partial filling of f -states. However, partially filled f -states are challenging to treat in density functional theory, so to limit the computational complexity and cost of this study we restrict ourselves to La as an A-site candidate, as La is expected to donate its f -electrons when it becomes 2+ while still producing a partially filled (d^1) d orbital.

For strategy (2), we consider $n = 1$ layered analogs of CePt_3Si . CePt_3Si is a known anti-perovskite polar metal exhibiting space group $P4mm$ [79]. The anti-RP derivative has the chemical formula $\text{Pt}_4\text{Ce}_2\text{Si}$. Determination of valence states is non-trivial in this compound, since both Pt and Ce are capable of donating electrons and hosting partially filled orbitals. However, it has been established that the electronic states at the Fermi level are predominantly contributed by Ce f -orbitals [159]. When converting between the anti-perovskite and anti-RP structure types, the ratio of cations to anions increases, so we expect fewer electrons donated from Ce and Pt, resulting in a similar if not slightly increased occupancy of the Ce f -states. In order to compensate for this change in orbital-filling, we also substitute La for Ce, expecting an empty $4f$ -shell and therefore partially occupied d -states at the Fermi level.

Between the two strategies, we have identified 19 candidate anti-RP polar metals. We relax each compound in the known anti-RP FE and PE phases ($I4mm$ and $I4/mmm$ respectively) and compute the electronic structure, crystal orbital Hamilton population (COHP), and lattice dynamics. We also use soft modes identified in the lattice dynamics simulations to generate candidate space groups, relaxing each chemistry in the various symmetries to identify likely ground states. We find that each compound is metallic, 3 demonstrate magnetic order, and 14 exhibit a

polar ground state. We assess the off-centering mechanism and find that, like their insulating FE counterparts, anion off-centering occurs primarily due to a geometric mechanism, although with the potential for indirect coupling to magnetic and mechanical perturbation.

6.2 Methods

We used density functional theory (DFT) as implemented in the Vienna Ab initio Simulation Package (VASP) [118, 119] to perform first principles calculations. We used a planewave basis set with a 600 eV energy cutoff and sampled the Brillouin zone with a sampling density of 2000 points per reciprocal atom in a Γ -centered mesh with Gaussian smearing (width of 0.1 eV). We selected the Perdew-Burke-Ernzerhof (PBE) exchange-correlation functional revised for solids (PBEsol) [34] and used the projector-augmented wave (PAW) method to treat the separation of the core and valence electrons [120]. Lattice parameters, volume, and atomic positions were relaxed such that the forces and stress tensor were converged to 5×10^{-4} eV \AA^{-1} and 2×10^{-3} eV \AA^{-2} , respectively. To treat the partially filled Ce $4f$ -states of $\text{Pt}_4\text{Ce}_2\text{Si}$, we followed the example of [160] and applied a Hubbard U of 8 eV. We compute the crystal orbital Hamilton population (COHP) using the LOBSTER software package to provide insight into the bond strength between ions across each chemistry [122–125].

6.3 Results and Discussion

6.3.1 Electronic structure

In each of the considered compounds, the Fermi level falls primarily among the partially occupied $5d$ states contributed by the A-site transition metal. Here we focus on $\text{Ta}_4\text{As}_2\text{O}$ as an example

Figure 6.2a; for electronic structure of other chemistries, see Appendix D. The A-site hybridizes with the B site, whose p states tend to be located anywhere from 1-7 eV below the Fermi level. Finally, we find the O (Si) p states at much lower energy, 8-10 eV below E_F . The precise location varies depending on the system. For example, the B-site p states in $\text{Au}_4\text{Pn}_2\text{O}$ (Pn = Pnictides) hybridize strongly with Au, spreading and stretching across E_F . The Si p states in $\text{Pt}_4\text{Ce}_2\text{Si}$ are similarly delocalized. We find that the most significant bonding occurs between A and B sites, perhaps intuitively due to their relative proximity in energy as shown in the COHP in Figure 6.2b. The A-site and the anion also exhibit significant bonding, but the strength is reduced as compared to the bond character between A-B due to the larger separation in energy.

When analyzing the electronic structure of the low-symmetry $I4mm$ phase (Figure 6.3a), the combination of a distorted crystal structure and clearly-defined bands suggests the utility of employing a Zintl model to describe charge-filling. Again using $\text{Ta}_4\text{As}_2\text{O}$ as an example, we can view the anti-RP structure as comprising three distinct moieties: Ta_2O and two TaAs clusters. Knowing that O and As will tend to fill their valence shells completely (via 2- and 3- valence states, respectively), we assume that optimizing those valence states and preserving charge balance will lead to Ta adopting a 2+ configuration, forming cationic $[\text{Ta}_2\text{O}]^{2+}$ and two anionic $[\text{TaAs}]^{1-}$ clusters. An analysis of the crystal orbital Hamilton population (COHP) for various atomic interactions confirms this assignment. The strongest Ta-As bonds occur within the two TaAs clusters, whereas the Ta atoms in the Ta_2O cluster bond more strongly with O than As. One of the two TaAs clusters is strongly bonded to Ta_2O via a Ta-O bond, while the other is only weakly bonded to the $[\text{Ta}_2\text{O}]\text{-}[\text{TaAs}]$ complex. Integrating the projected density of states (PDOS) for the d -orbital of each Ta site reveals that the two Ta associated with Ta_2O are $d^{2.4}$, or effectively in a 2.6+ valence state, as is the Ta in the strongly-bonded TaAs cluster. Meanwhile, the Ta in the weakly bonded

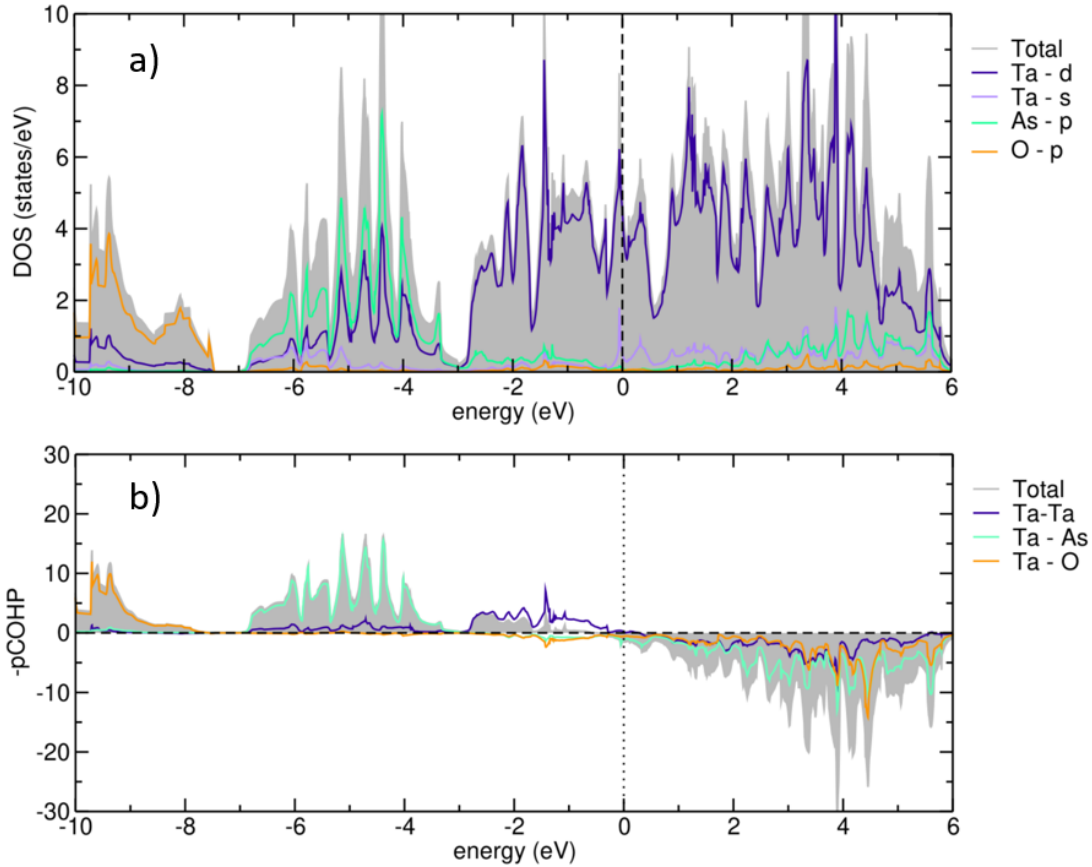


FIGURE 6.2: (a) Projected density of states (PDOS) and (b) projected crystal orbital Hamilton population (pCOHP) for $I4/mmm$ $\text{Ta}_4\text{As}_2\text{O}$. (a) Ta d -states dominate at the Fermi level, while As and O bands sit at lower energy. (b) Ta bonding interactions dominate, separating clearly into Ta-Ta, Ta-As, and Ta-O interactions. The Fermi level is located just above the transition from bonding to anti-bonding states, with a modest but non-negligible anti-bonding character at the Fermi level.

TaAs adopts a $d^{2.9}$ configuration. The difference in electron-filling between the Ta sites is primarily driven by their proximity to the O site. Three out of four Ta sites experience bonding with both As and O sites, whereas Ta in the weakly-bonded TaAs cluster only bonds with As. O is also more electronegative than As, further enhancing the difference between the Ta sites. The crystal chemical formula for $\text{Ta}_4\text{As}_2\text{O}$ is then approximately $[\text{Ta}_2\text{O}]^{2+}[\text{TaAs}-b]^{1-}[\text{TaAs}-u]^{1-}$, where $-b$ and $-u$ differentiate between the bonded and unbonded TaAs clusters respectively. We can think of $[\text{Ta}_2\text{O}]^{2+}$ and $[\text{TaAs}-b]^{1-}$ as forming a strong covalent bond via O, whereas $[\text{TaAs}-u]^{1-}$ forms

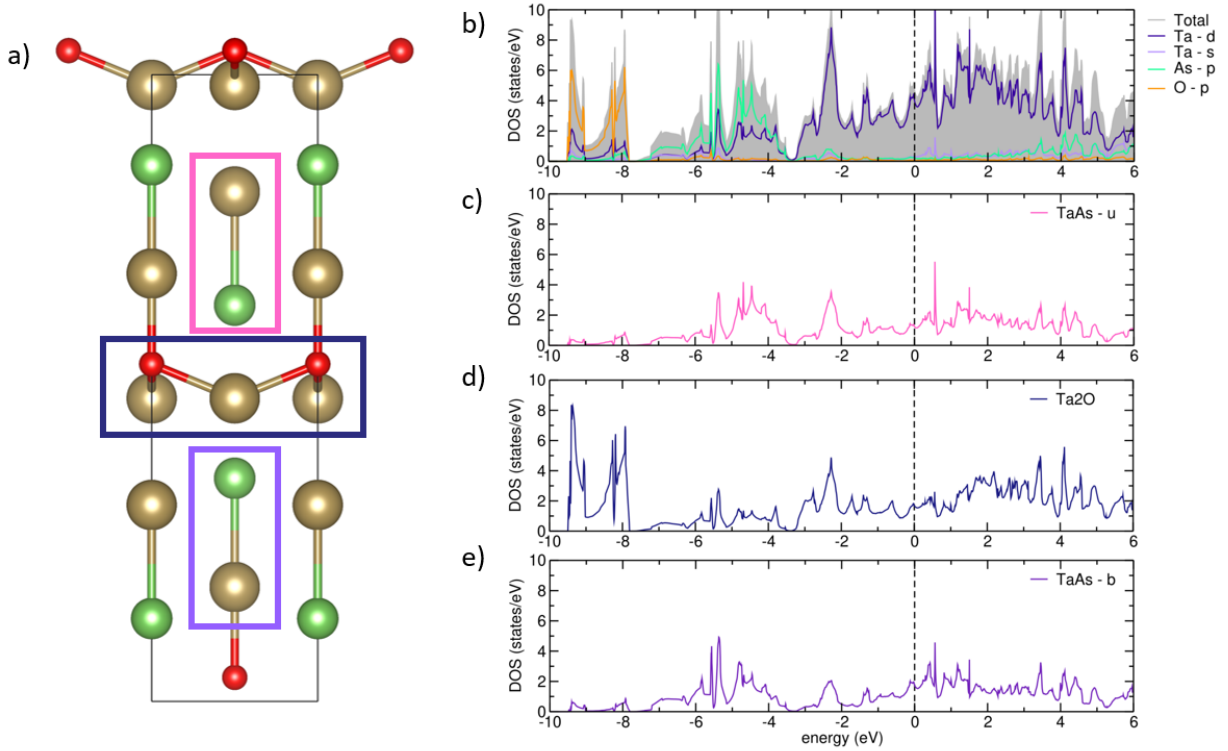


FIGURE 6.3: (a) $\text{Ta}_4\text{As}_2\text{O}$ $I4mm$ phase, with Zintl clusters highlighted. (b) Total and projected DOS for $I4mm$ $\text{Ta}_4\text{As}_2\text{O}$. (c-e) Projected DOS for each Zintl cluster highlighted in (a).

a more ionic bond with $[\text{Ta}_2\text{O}]^{2+}$ which results in the slightly higher d-orbital filling in $\text{TaAs}-u$ (Figure 6.3).

6.3.2 Magnetism

Three of the chemistries exhibit magnetic ordering: $\text{Pt}_4\text{Ce}_2\text{Si}$, $\text{Re}_4\text{As}_2\text{O}$, and $\text{Re}_4\text{P}_2\text{O}$. CePt_3Si is known to undergo an AFM transition at 2.2K [161] so a magnetic ground state is not unexpected in $\text{Pt}_4\text{Ce}_2\text{Si}$. However, in the layered anti-RP $I4/mmm$ structure, the magnetic ground state becomes FM, favored over AFM ordering by 57 meV/f.u. with an average local magnetic moment of $0.9\mu_B/\text{Ce}$ atom (while local moment is generally ill-defined in metallic systems, we can estimate by projecting onto the charge density within the Wigner-Seitz radius). The same energy difference

persists approximately in the lower symmetry structure (47 meV/f.u.), as does the local magnetic moment. Although, interestingly, in the $I4mm$ phase only every other Ce site exhibits a nonzero moment, with the local moment being extinguished for the Ce atoms more highly coordinated by Pt ions (i.e., equivalent of the Ta₂O cluster in Ta₄As₂O). This is compatible with observations of the magnetic phase in CePt₃Si under pressure, which showed that pressure extinguishes both the AFM order and the superconducting transition [162]. Although the precise mechanism behind AFM ordering in CePt₃Si is under debate, the magnetic ordering of Ce f states is clearly sensitive to changes in the local structural environment.

Both Re-based compounds exhibit itinerant ferromagnetism, although again the distribution and amplitude of the magnetic moment varies depending on the crystal structure. In the $I4/mmm$ phase, Re₄As₂O does not exhibit a magnetic moment, but Re₄P₂O exhibits a local moment of 0.12 μ_B /Re atom (only associated with the 50% of Re sites not in-plane with O). In the $I4mm$ phase, Re₄As₂O exhibits a local moment of 0.5 μ_B /Re atom, but only one Re atom per unit cell contributes; specifically, the free Re atom in the Zintl cluster model. $I4mm$ Re₄P₂O exhibits the same magnetic ordering pattern, but with a local moment of 0.37 μ_B /Re. Coupling between crystal structure and magnetic order in these three compounds bodes well for the realization of an anti-RP magnetic polar metal, analogous to the insulating multiferroic Eu₄Sb₂O [157].

6.3.3 Lattice dynamics and stability

All compounds were relaxed with $I4/mmm$ and $I4mm$ symmetry. Systems with A=La or Au relaxed back to $I4/mmm$ when subject to an $I4mm$ perturbation, whereas all others stabilized in the $I4mm$ space group. Computing the phonons for each chemistry revealed that none of the studied compounds except for La₄Sb₂O is dynamically stable in either $I4/mmm$ or $I4mm$ space

groups (see Figure 6.4a-c for example, and Appendix D for full set of $I4/mmm$ phonon dispersions). Investigation of the relationship between $I4/mmm$ and $I4mm$ space groups reveals that O (or Si) off-centering is the driver of broken inversion symmetry, which is consistent with the literature on anti-RP FEs. Using $\text{Ta}_4\text{As}_2\text{O}$ as an example, we can visualize the distortion pathway from high to low symmetry as a result of two distortion modes, Γ_3^- and Γ_1^+ . Γ_1^+ retains each symmetry element of the high symmetry phase, and therefore cannot be the primary distortion mode. If Γ_3^- drives the distortion, then O must be primarily responsible for lifting inversion since Γ_3^- is dominated by O off-centering. It would be intuitive to see the displacement of O as primarily driven by Pt-O hybridization. However, if we compare the projected DOS of the high and low symmetry structures (Figure 6.2a vs Figure 6.3b), we see the bandwidth of the O-dominated band decreases with symmetry-lowering—a more narrow bandwidth is typically associated with reduced hybridization. If we integrate the projected COHP for the Pt-O interaction in both $I4/mmm$ and $I4mm$, we find it actually slightly decreases after symmetry-lowering has occurred, indicating a reduction in overall Pt-O bond strength. This is not inconsistent with previous work on Ba-based anti-RP FEs, which noted that bonding was not a driving force in these compounds either [157]. Rather, more efficient packing is achieved by the displacement of the anion, also known as a geometric displacement mechanism.

To survey possible ground state structures, we examined the symmetries broken by the lattice instabilities of both $I4mm$ and $I4/mmm$ structures and identified 10 candidate ground state space groups. Each chemistry was relaxed in each space group, leading to identification of a candidate ground state for each composition (Table 6.1). Overall, 14 compounds were identified as likely to exhibit polar ground states, 1 was identified as nonpolar noncentrosymmetric, and 4 were identified as centrosymmetric. Alongside the space group we have also reported the energy per formula unit

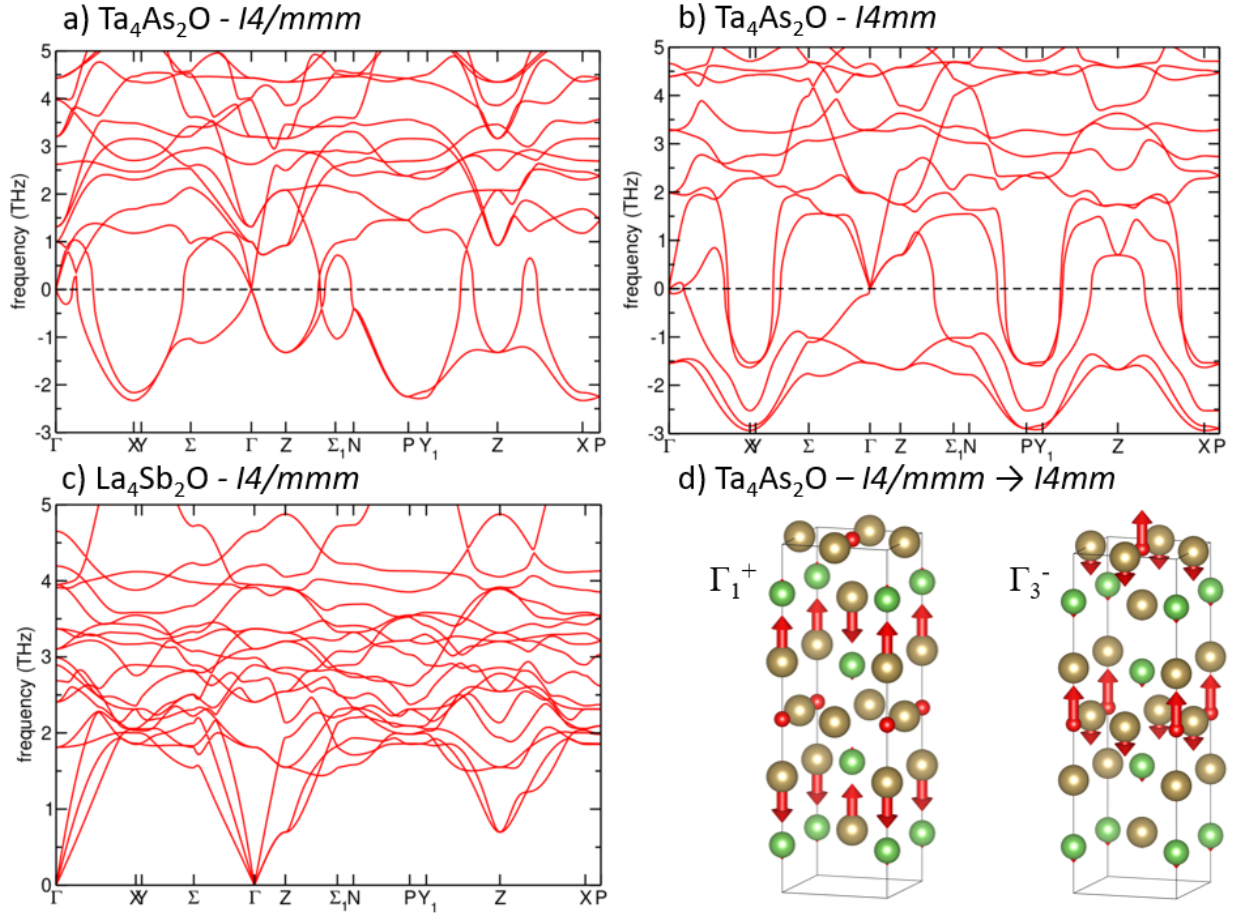


FIGURE 6.4: (a-c) Phonon dispersions as calculated for (a) $I4/mmm$ Ta₄As₂O, (b) $I4mm$ Ta₄As₂O, and (c) $I4/mmm$ La₄Sb₂O. (d) Distortion modes Γ_1^+ (strain mode, amplitude = 0.36 Å) and Γ_3^- (distortion mode, amplitude = 0.60 Å) relating $I4/mmm$ and $I4mm$ phases of Ta₄As₂O. Arrows denote atomic displacements associated with each distortion mode (amplitude of distortion is exaggerated for clarity). Note that although $I4mm$ Ta₄As₂O is -480 meV/f.u. lower in energy than the $I4/mmm$ phase, there is no Γ point instability in the $I4/mmm$ phase.

relative to the high symmetry $I4/mmm$ reference structure. Nearly all candidate ground states are at least 500 meV/f.u. lower in energy than $I4/mmm$, making the lower-symmetry phases likely stable above room temperature. However, for La₄Sb₂O and La₄As₂O, the $I4/mmm$ phase is less than 40 meV/f.u. higher in energy than the $I4mm$ potential ground state, making switching via $I4/mmm$ a possibility.

The majority of the polar candidate ground states are directly related to Γ -point instabilities in

TABLE 6.1: Candidate ground state symmetries as determined by relaxation along symmetry paths defined by lattice instabilities. Computed for A_4B_2X chemistries. The energy of each candidate ground state phase relative to the high symmetry $I4/mmm$ reference is also reported.

A	B	X	Space Group	meV/f.u. (vs $I4/mmm$)
Au	P	O	$Pmma$	-1.80×10^3
Pt	P	O	$C2$	-4.23×10^3
Ir	P	O	$I\bar{4}m2$	-5.20×10^3
Os	P	O	$Imm2$	-5.02×10^3
Re	P	O	$Pmn2_1$	-4.74×10^3
W	P	O	Cm	-3.14×10^3
Ta	P	O	$Ama2$	-9.91×10^2
Au	As	O	$Pmma$	-1.43×10^3
Pt	As	O	Cm	-3.67×10^3
Ir	As	O	Cm	-4.37×10^3
Os	As	O	$Pmn2_1$	-5.82×10^3
Re	As	O	$Imm2$	-4.07×10^3
W	As	O	Cm	-3.30×10^3
Ta	As	O	Cm	-1.13×10^3
La	P	O	$Cmce$	-5.34×10^2
La	As	O	$I4mm$	-3.60×10^1
La	Sb	O	$I4mm$	-2.95×10^1
Pt	Ce	Si	$Ama2$	-5.26×10^4
Pt	La	Si	$Pmmn$	-1.56×10^3

the phonon dispersion, a well known feature of the high symmetry phase in anti-RP FEs [157,158]. However, several of the compositions which appear to exhibit a polar ground state show more prominent instabilities at the zone boundary than the zone center. In addition, a few compounds (namely, $I4/mmm$ phases of Ta_4As_2O , La_4Sb_2O , and La_4P_2O) appear stable based on phonon frequencies at the Γ point and yet a polar space group is most favorable, generally by a significant reduction in energy (-36 meV/f.u., -30 meV/f.u., and -480 meV/f.u. for La_4P_2O , La_4Sb_2O , and Ta_4As_2O respectively).

Although more detailed study is warranted to ascertain the distortion pathway to these unanticipated polar ground states, it seems likely that strain plays a significant role. As noted above,

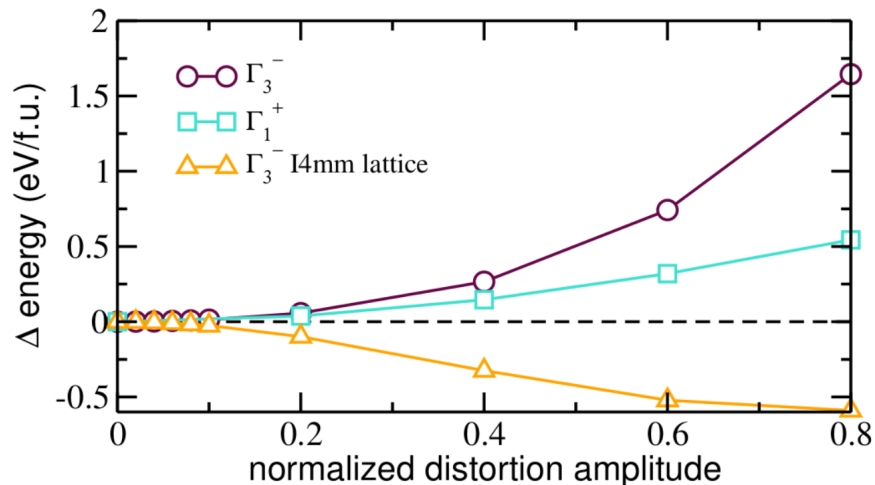


FIGURE 6.5: The change in energy as a result of applying the symmetry adapted distortion modes describing the relationship between $\text{Ta}_4\text{As}_2\text{O}$ $I4/mmm$ and $I4mm$ phases. The data labelled “ $I4mm$ lattice” applies the Γ_3^- distortion relative to an $I4/mmm$ crystal structure with the lattice constants of the $I4mm$ phase (so the 0 eV reference for that plot is an $I4/mmm$ structure with $I4mm$ lattice constants, not the fully relaxed $I4/mmm$ structure).

the Γ_1^+ mode is not capable of driving a symmetry-lowering transition, but its amplitude is considerable, changing lattice constants by more than 10% and contributing significant displacements of A and B sites relative to one another. Strain was shown to be a valuable tool in tuning the polar distortion in anti-RP FEs [157], and plays a similarly influential role here. The relationship between strain (Γ_1^+) and distortion (Γ_3^-) modes in $\text{Ta}_4\text{As}_2\text{O}$ is illustrated in Figure 6.5. Neither mode lowers the energy when applied alone to $I4/mmm$, but when the lattice distortion is enforced the Γ_3^- displacement becomes favorable.

6.3.4 Weak coupling

The predicted symmetry-lifting pathway from $I4/mmm$ to $I4mm$ in the anti-RP polar metals appears to follow the same mechanism observed in anti-RP FEs: a geometric mechanism derived from the size of the cation octahedron relative to the anion drives the change in symmetry [157,158].

A consistent off-centering mechanism between FE and polar metallic variants of a structure type

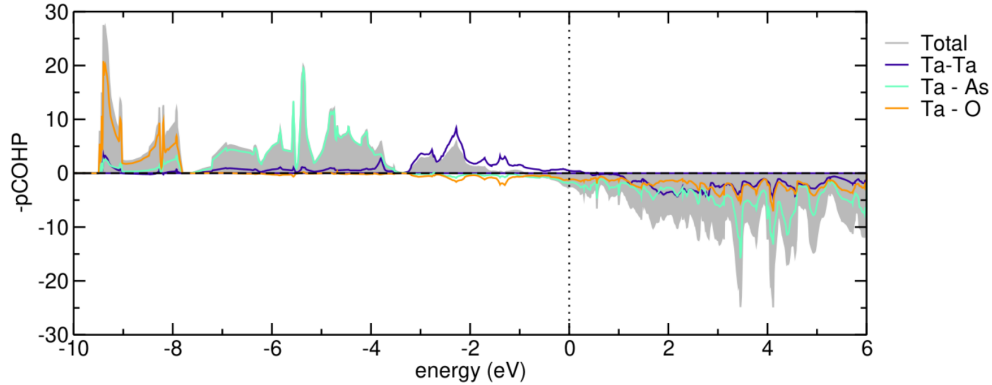


FIGURE 6.6: Projected COHP for the $\text{Ta}_4\text{As}_2\text{O}$ $I4mm$ phase.

would indicate that the distortion mechanism must be fully decoupled from the electronic structure. However, close examination of the COHP near the Fermi level reveals non-negligible antibonding character (Figure 6.2). Nature abhors occupying anti-bonding states, implying that the structure would seek a transition which pushes those states to higher energy. The anion optimizes its local environment in the transition from $I4/mmm$ to $I4mm$ but it does not contribute states at the Fermi level and therefore does not relieve the instability in the electronic structure. Antibonding states corresponding to A-B hybridization, however, do sit near E_F . Their displacement relative to one another as part of the Γ_1^+ mode does not reduce the concentration of anti-bonding states at E_F —it may even enhance it (Figure 6.6)—but this perhaps indicates that A-B interactions play a prominent role in stabilizing the eventual ground state. If true, this would be evidence of modest coupling between a distortion mechanism and the Fermi level.

The sensitivity of the magnetic order to symmetry changes also indicates modest coupling between the partially occupied d and f orbitals and the off-centering mechanism. Further work is needed to ascertain the nature of the magnetic interactions at play in both $\text{Pt}_4\text{Ce}_2\text{Si}$ and the Re-based polar metals.

6.4 Conclusion

In summary, we have designed a new class of polar metals in the anti-RP structure family, predicting band conductivity in 19 previously unstudied compositions and polar order in 14 of those 19 structures. Whereas direct coupling between the crystal structure and free charge carriers in anti-RP polar metals is unlikely, there is evidence of multiple indirect couplings between the polar structural distortion and secondary properties in the form of magnetic order, strain, and A-B hybridization. These findings speak to the potential for the anti-RP structure type to serve as a platform for generating tunable distortive polar metals. Further analysis of the distortion mechanism and the stability of the proposed ground state structures is warranted in order to provide sufficient motivation for experiment to attempt the synthesis of this new class of materials.

Chapter 7: Conclusions and Outlook

7.1 Summary and conclusions

In this dissertation, I examined the relationship between free charge carriers and inversion-lifting distortion patterns. Polar metals have been shown to host various desirable properties and recent work suggests they may be more common than previously thought, although the surge in interest has led to some confusion and gaps in our understanding of the fundamental relationships at play. In order to clarify the interplay between metallicity and inversion symmetry across materials platforms, I used first principles simulations to perform the following investigations:

In Chapter 4, I re-examined the effect of doping on the polar distortion in BaTiO_3 through the lens of changes in the second order Jahn-Teller (SOJT) effect, a local off-centering mechanism. I studied the charge density along the Ti-O bond, lattice dynamics of the cubic phase, shifting orbital energy levels, and multiple descriptions of covalent bonding under electron and hole doping using the compensating background charge approach. I discovered that the redistribution of charge under doping was well-described by a charge self-regulation model, relating changes in the electronic structure to the shifting real-space electron density. I also identified an asymmetrical response in the polar instability under negatively and positively charged dopants, which both underscored the

significance of short-range interactions as a driving force for local polar displacements in ferroelectrics and revealed the value of examining the bonding character of the occupied orbitals when attempting to predict the effect of doping on a covalently-driven distortion mechanism. Assessing changes in bonding character via both the projected crystal orbital Hamilton population (pCOHP) and projections of maximally localized Wannier functions (MLWFs) illustrated how charge carriers can disrupt the SOJT effect by prohibiting orbital overlap. This work explains why conductivity and acentricity appear to be contraindicated in SOJT-driven ferroelectrics, while still allowing that modest conductivity and polar order may coexist in these materials beyond the threshold for screening long-range Coulombic interactions. The tools and metrics developed in this work are equally applicable to other doped ferroelectric systems and should be capable of distinguishing between classes of polar metals as well.

In Chapter 5, I studied another doped ferroelectric system, photodoped EuTiO_3 deposited on DyScO_3 (DSO). I worked with experimental collaborators to understand how free charge carriers might affect a polar distortion stabilized by tensile strain. I developed an approximation for photodoping and predicted that strained EuTiO_3 , much like BaTiO_3 , should recover centrosymmetry in the presence of free charge carriers, as occupation of the Ti-dominated conduction band disrupts the SOJT-driven displacement of Ti. However, experimental results showed that after an initial decrease, the polar distortion stabilized at about 86% of its original amplitude. This led to a reconsideration of the mode dynamics, which revealed anomalously large A-site contributions and changing displacement pattern under both strain and doping. This observation, coupled with an assessment of the assumptions inherent to my simulation, developed into a hypothesis that strained EuTiO_3 undergoes a change in distortion character under photodoping, evolving from ferroelectric-like incompatibility between charge carriers and polar order to a polar metallic stability of the

polar distortion. My observations of changing mode dynamics under strain and under doping carry implications for other systems and should serve as a call both for further work investigating the changes in EuTiO_3 and a search for similar behavior in other systems. The potential mutability of mode dynamics has significant implications for engineering extrinsically metallic polar metals.

Finally, in Chapter 6, I predicted a new sub-class of polar metals in the anti-Ruddlesden-Popper (anti-RP) structure family (following the chemical formula $\text{A}_4\text{B}_2\text{O}$, where A and B are both cations). Observing that all of the experimentally synthesized anti-RPs undergo ferroelectric phase transitions, I also noted that inversion was broken by the relative motion of the anion relative to a cation cage, and hypothesized that engineering the cations to contribute free charges at the Fermi level might present a path toward the violation of weak-coupling in a polar metal. I developed two design strategies for introducing metallicity to this structure type: (1) $n = 1$ derivatives of metallic anti-perovskites (of which there are many known polar metals) and (2) transition metal or rare earth substitution for the A-site cation in order to induce partially occupied d - or f - orbitals. I simulated 19 different chemistries, including their structural relaxations, COHP projections, lattice dynamics, and performed an electronic structure analysis of each compound in the previously observed high and low-symmetry space groups of the ferroelectric anti-RPs. I found that each chemistry produced a band metal, and that all but 5 chemistries exhibited polar instabilities. A survey of candidate ground states derived from the lattice dynamics revealed that most of the studied compounds prefer either a monoclinic or orthorhombic space group (as opposed to the $I4mm$ ground states in observed Anti-RP FEs), with all but the aforementioned 5 compounds exhibiting a polar ground state. An investigation of the distortion dynamics also revealed that the polar displacement was not primarily driven by anion bonding within its cation cage, but rather a combination of A-B site bonding and geometric displacements. Investigations of the pCOHP confirmed that non-bonding

states tend to dominate the Fermi level, meaning that Anti-RP polar metals are unlikely to violate the weak-coupling principle. They represent a new platform for designing displacive polar metals, with the possibility of tuning properties by engineering the number of layers, as has been done in the Ruddelsden-Popper family.

7.2 Frontiers in polar metals research

The outlook for polar metals research has never held more possibility. The number of publications in the research space continues to climb and we have made great strides in determining the necessary relationship between electronic and crystallographic structure to enable their coexistence. Although there remain some unanswered questions (e.g. is ‘weak-coupling’ a necessary condition or merely a useful design principle?), there are also opportunities to significantly broaden the polar metallic design space. I highlight two such opportunities here: two-dimensional heterostructures and polar metallic pyrochlores.

7.2.1 Two-dimensional heterostructures

Accompanying the advent of 2D materials has been a recent interest in the emergent phenomena that occur when two sheets of material are stacked on top of one another; Moiré heterostructures like those in the famous “magic angle” graphene are being explored in a variety of van der Waals materials [94, 163–166]. However, work thus far has exclusively focused on small-bandgap semiconductors and semimetals. In addition, “twisting” typically occurs mechanically and continuously. Concurrently, in the past year we have seen a significant increase in the number of predicted and synthesized two-dimensional polar metals [15, 76, 167–170]. I see an opportunity to significantly

broaden the phase space of both topologically non-trivial materials and acentric conductors by considering two dimensional metals and scalable, discrete stacking mechanisms.

Metallic correlated transition metal dichalcogenides have yet to be investigated in Moiré heterostructures. Noting that interlayer twisting at most angles breaks inversion symmetry, this presents a pathway for a new class of noncentrosymmetric metals, which may facilitate the generation of tunable charge density waves as well as topological conduction mechanisms and create exotic opportunities to support new physics. However, the number of metallic 2D transition metal dichalcogenides is limited, motivating an interest in looking beyond van der Waals stacking (which requires mechanical stacking amidst a continuum of possible twist angles) toward coincident site lattices and stacking facilitated by interlayer organic complexes.

I recently collaborated with Prof. Efrain Rodriguez (University of Maryland), who has a track record of synthesizing layered tetrahedral transition metal chalcogenides (termed TTMCs, which also tend to be metallic), to demonstrate the utility of hybrid inorganic-organic layered materials as a platform for combining multiple properties in the first synthesized ferromagnetic polar metal [92]. Efrain and his team (namely Huafei Zheng and Brandon C. Wilfong) grew CoS TTMC layers intercalated by $\text{Co}(en)_3$ complexes (full structure name abbreviated to en-CoS, where en =ethylenediamine, see Figure 7.1a) and characterized their magnetic, transport, and structural properties with the help of Peter J. Zavalij (also at Maryland). I performed first principles simulations which confirmed their assessment that en-CoS is a metallic ferromagnet (Figure 7.1b-c), with a simulated magnetic moment of $0.7 \mu_B/\text{Co}$ (in reasonable agreement with a measured effective moment of $0.289 \mu_B/\text{Co}$). Comparing the experimentally solved low-symmetry structure ($Pca2_1$) to a hypothetical high-symmetry structure ($Pbcn$) and examining the location of the intercalates reveals that the polar order is likely driven by polar hydrogen bonding between

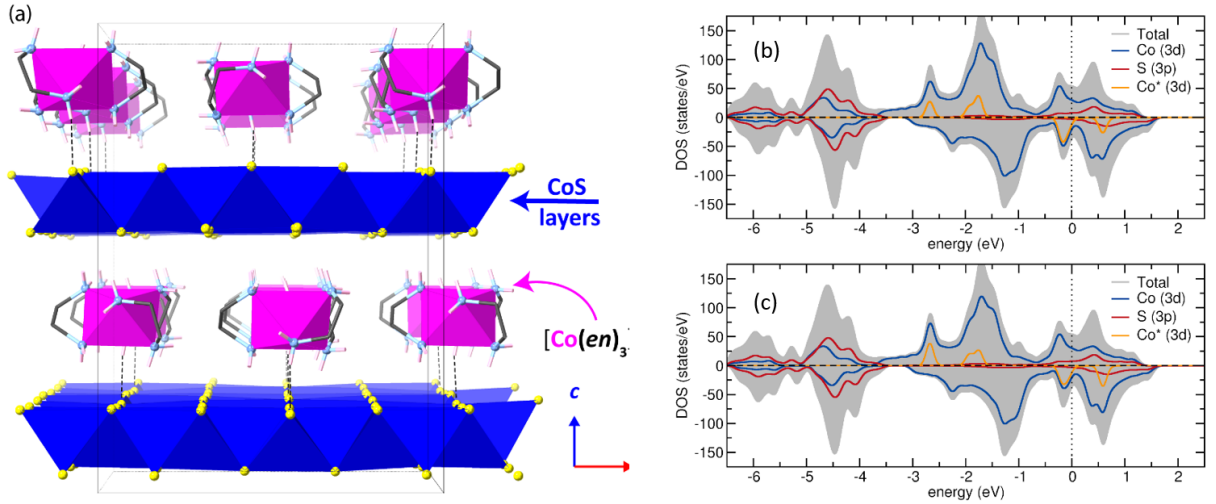


FIGURE 7.1: (a) Single crystal structure of $[\text{Co}(\text{en})_3](\text{CoS})_{12}\cdot\text{en}$ where en = ethylenediamine. The $[010]$ view of the orthorhombic unit cell with the $[\text{Co}(\text{en})_3]^{2+}$ octahedral complexes closer to the lower CoS layer by $0.135(5)\text{\AA}$ than they are to the upper CoS layer as indicated by the dashed lines. Hydrogens of $\text{C}-2\text{H}_4$ -backbone of en left out for clarity. (b-c) Electronic density of states (DOS) for (b) model high symmetry structure with $Pbcn$ symmetry and (c) experimental low symmetry structure with $Pca2_1$ symmetry. Co^* denotes the intercalate Co atoms.

the $\text{Co}(\text{en})_3$ complexes and the metallic CoS layers.

This hydrogen bonding present in this modality (rather than the comparatively weaker van der Waals interactions present in known Moire heterostructures) enforces twist angles which can be tuned to align layers such that a coincident site superlattice emerges from the heterostructure [171,172]. Discrete angles enforced via hydrogen bonding result in a more scalable, higher fidelity process than mechanical, continuum twisting. In fact, to date, one of the main problems is the omnipresence of twist-angle disorder that results from the manufacture of the devices. Small angular fluctuations often result in different physical properties with the result that no two identical results have yet been reported. This poses a serious obstacle to elucidating and establishing a unified understanding of the underlying physical mechanism.

Within these two potential thrusts, there are opportunities to couple to additional degrees of freedom. I identify at least three possible inversion-symmetry breaking mechanisms (bilayer

twisting, polar hydrogen bonding by intercalate organic complexes, and intrinsically polar layers), representing three potential sub-classes of polar metal. It is also possible to modulate the degree of correlation by choice of anion, and magnitude of spin orbit coupling and magnetic ordering by choice of cation. The rich phase space of layered two-dimensional metals is currently poorly understood, but we expect it to contain many new polar metallic materials with exotic properties.

7.2.2 Polar metallic pyrochlore

Pyrochlores have been shown to host diverse properties, largely as a result of their geometrically frustrated interpenetrating sublattices (Figure 7.2). These properties include ferroelectricity [173–175], superconductivity [20], and NCSM behavior [176,177]. However, a polar metallic pyrochlore has yet to be predicted or synthesized. This is a non-trivial challenge, as the lattice dynamics of pyrochlores are highly complex. For example, the relaxor ferroelectric $\text{Cd}_2\text{Nb}_2\text{O}_7$ exhibits two competing unstable polar phonon modes which cooperate to drive a phase transition from cubic $Fd\bar{3}m$ to the polar $Ima2$ phase (and subsequently a monoclinic phase at lower temperature) [178–181]. In a collaboration with Geneva Laurita and Samra Husremovic from Bates College, along with Jun Li, Arthur W. Sleight, and Mas A. Subramanian from Oregon State University and Robin Macaluso from the University of Texas from Arlington, we showed that while this phase transition is dominated by the SOJT-active displacement of the Nb atoms, changes in the covalent bond strength of the Cd sublattice—induced by S substitution for O—dramatically changed the nature of the phase transition from proper to improper to eliminating the polar instability entirely (Figure 7.2).

Predicting how perturbations to one sublattice will impact the mode dynamics of the other sublattice is far from trivial, which makes the design of a polar metallic pyrochlore a significant

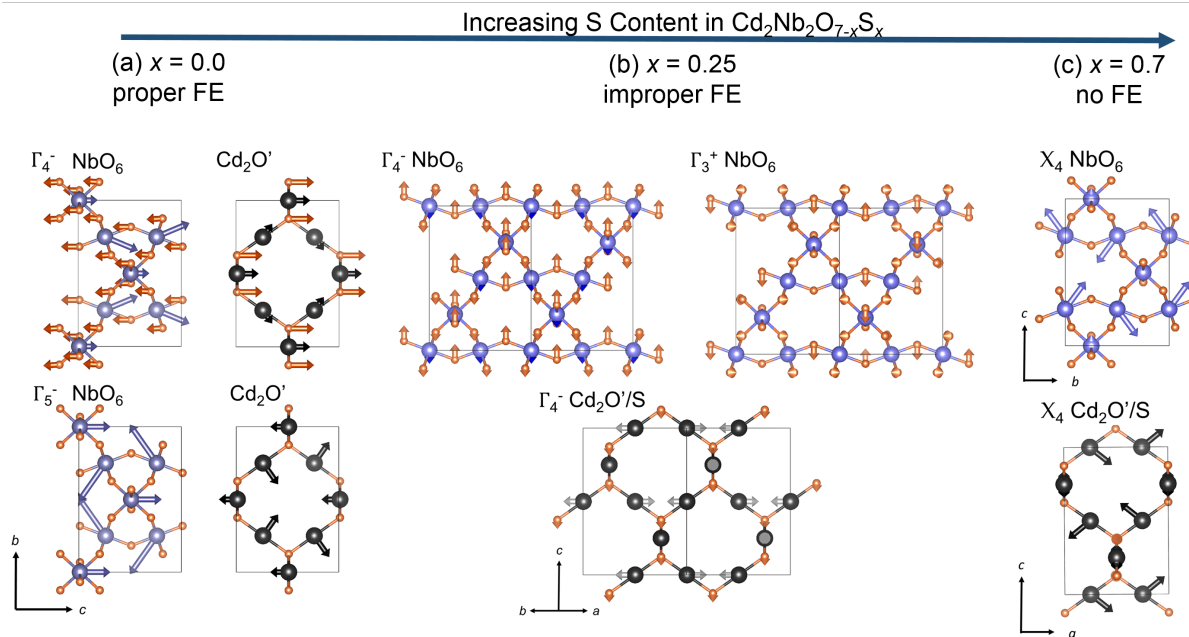


FIGURE 7.2: Comparison of the distortion modes of the solid solution reveals that sulfur substitution not only alters the observed low temperature structure, but additionally changes the nature of the phase transition from (a) proper ferroelectric (FE) in the $x = 0.0$ sample, (b) to improper ferroelectric in the $x = 0.25$ sample, to (c) proper noncentrosymmetric (not ferroelectric) in the $x = 0.7$ sample.

challenge. The most straightforward design strategy may be to begin with a noncentrosymmetric metallic pyrochlore (e.g. $\text{Cd}_2\text{Re}_2\text{O}_7$ [20,176] or $\text{Pb}_2\text{Re}_2\text{O}_7$ [182]) and explore perturbations to their respective off-centering mechanisms that may preserve metallic conductivity but induce coordinated polar off-centering. If successful, the design of a polar metallic pyrochlore would be significant for several reasons. First, the total number of displacive polar metals is relatively low, and a “relaxor-type” polar phase transition (like the one in $\text{Cd}_2\text{Nb}_2\text{O}_7$) has yet to be observed in a polar metal. An extended regime of gradually ordering polar distortions vs temperature would allow for new insights into the dynamics that allow for long-range coordinated off-centering in metallic systems. A polar metallic pyrochlore is also an interesting candidate to violate the weak-coupling hypothesis. Since the two sublattices are fundamentally linked [82,178], there is the potential that the inversion-lifting mechanism could be fully decoupled from the Fermi level. The characteristics which make a polar

metallic pyrochlore desirable of course may also ultimately prevent its realization (e.g. if weak-coupling is a necessity). However, an investigation into such a compound would be informative regardless of the outcome, and if successful it would be an opportunity to observe the behavior of a geometrically frustrated polar metal.

These are far from the only two important research directions for the field of polar metals. As evidenced by Table A.1, there are a great many predicted compounds; experimental verification of predicted polar metallic dynamics is a pressing need. In addition, the search for compounds that violate weak-coupling continues to be of interest and may require expanding the field into new structure families. Finally, the properties and applications of polar metals are not yet fully appreciated. Recent work on topological phonons indicates that polar metals are ideal candidates to host this recently described phenomenon [183], while the potential for polar metals to impact the fields of photovoltaics, energy storage, and quantum computing systems remains largely untapped. I believe that my work clarifying and classifying acentric conductors has helped lay the foundation for these and other investigations. I look forward to seeing how this field will continue to develop in the future.

Bibliography

- [1] P. W. Anderson and E. I. Blount. Symmetry considerations on martensitic transformations: ‘ferroelectric’ metals? *Physical Review Letters*, 14(7):217–219, February 1965.
- [2] Youguo Shi, Yanfeng Guo, Xia Wang, Andrew J. Princep, Dmitry Khalyavin, Pascal Manuel, Yuichi Michiue, Akira Sato, Kenji Tsuda, Shan Yu, Masao Arai, Yuichi Shirako, Masaki Akaogi, Nanlin Wang, Kazunari Yamaura, and Andrew T. Boothroyd. A ferroelectric-like structural transition in a metal. *Nature Materials*, 12(11):1024–1027, September 2013.
- [3] J. Hwang, T. Kolodiazhnyi, J. Yang, and M. Couillard. Doping and temperature-dependent optical properties of oxygen-reduced $\text{BaTiO}_{3-\delta}$. *Physical Review B - Condensed Matter and Materials Physics*, 82(21):1–8, 2010.
- [4] J. Hlinka, J. Petzelt, S. Kamba, D. Noujni, and T. Ostapchuk. Infrared dielectric response of relaxor ferroelectrics. *Phase Transitions*, 79(1-2):41–78, January 2006.
- [5] L. R. Testardi and T. B. Bateman. Lattice instability of high-transition-temperature superconductors. II. single-crystal V_3Si results. *Physical Review*, 154(2):402–410, February 1967.

- [6] P J Brown, K-U Neumann, and K R A Ziebeck. A polarized neutron investigation of the martensitic phase transition in V_3Si : evidence for a band Jahn-Teller mechanism. *Journal of Physics: Condensed Matter*, 13(5):1111–1117, January 2001.
- [7] C. Paduani and C. A. Kuhnen. Martensitic phase transition from cubic to tetragonal V_3Si : an electronic structure study. *The European Physical Journal B*, 66(3):353–359, November 2008.
- [8] Ronald E. Cohen. Origin of ferroelectricity in perovskite oxides. *Nature*, 358(6382):136–138, July 1992.
- [9] Yoshiyuki Yoshida, Shin-Ichi Ikeda, Hirofumi Matsuhata, Naoki Shirakawa, C. H. Lee, and Susumu Katano. Crystal and magnetic structure of $Ca_3Ru_2O_7$. *Physical Review B*, 72(5), August 2005.
- [10] Danilo Puggioni and James M. Rondinelli. Designing a robustly metallic noncentrosymmetric ruthenate oxide with large thermopower anisotropy. *Nature Communications*, 5(1), March 2014.
- [11] Nicole A. Benedek and Turan Birol. ‘Ferroelectric’ metals reexamined: Fundamental mechanisms and design considerations for new materials. *Journal of Materials Chemistry C*, 4:4000–4015, 2016.
- [12] H. J. Xiang. Origin of polar distortion in $LiNbO_3$ -type “ferroelectric” metals: Role of A-site instability and short-range interactions. *Physical Review B*, 90(9), September 2014.

- [13] Hong Jian Zhao, Alessio Filippetti, Carlos Escorihuela-Sayalero, Pietro Delugas, Enric Canadell, L. Bellaiche, Vincenzo Fiorentini, and Jorge Íñiguez. Meta-screening and permanence of polar distortion in metallized ferroelectrics. *Physical Review B*, 97(5), February 2018.
- [14] W. X. Zhou and A. Ariando. Review on ferroelectric/polar metals. *Japanese Journal of Applied Physics*, 59(SI):SI0802, May 2020.
- [15] Zaiyao Fei, Wenjin Zhao, Tauno A. Palomaki, Bosong Sun, Moira K. Miller, Zhiying Zhao, Ji-aqiang Yan, Xiaodong Xu, and David H. Cobden. Ferroelectric switching of a two-dimensional metal. *Nature*, 560(7718):336–339, July 2018.
- [16] Liang Wu, S. Patankar, T. Morimoto, N. L. Nair, E. Thewalt, A. Little, J. G. Analytis, J. E. Moore, and J. Orenstein. Giant anisotropic nonlinear optical response in transition metal monpnictide Weyl semimetals. *Nature Physics*, 13(4):350–355, December 2016.
- [17] Mandvi Saxena, Pinku Roy, Megha Acharya, Imon Bose, Khagesh Tanwar, and Tanmoy Maiti. Enhanced thermoelectric figure-of-merit in environmentally benign $\text{Ba}_x\text{Sr}_{2-x}\text{TiCoO}_6$ double perovskites. *Applied Physics Letters*, 109(26):263903, December 2016.
- [18] Hideaki Sakai, Koji Ikeura, Mohammad Saeed Bahramy, Naoki Ogawa, Daisuke Hashizume, Jun Fujioka, Yoshinori Tokura, and Shintaro Ishiwata. Critical enhancement of thermopower in a chemically tuned polar semimetal MoTe_2 . *Science Advances*, 2(11):e1601378, November 2016.

- [19] Masaaki Isobe, Hiroyuki Yoshida, Koji Kimoto, Masao Arai, and Eiji Takayama-Muromachi. SrAuSi₃: A noncentrosymmetric superconductor. *Chemistry of Materials*, 26(6):2155–2165, 2014.
- [20] Hironori Sakai, Kazuyoshi Yoshimura, Hiroyuki Ohno, Harukazu Kato, Shinsaku Kambe, Russell E. Walstedt, Tatsuma D. Matsuda, Yoshinori Haga, and Yoshichika Onuki. Superconductivity in a pyrochlore oxide, Cd₂Re₂O₇. *Journal of Physics: Condensed Matter*, 13:L785–L790, 2001.
- [21] Takeshi Shibayama, Minoru Nohara, Hiroko Aruga Katori, Yoshihiko Okamoto, Zenji Hiroi, and Hidenori Takagi. Superconductivity in Rh₂Ga₉ and Ir₂Ga₉ without Inversion Symmetry. *Journal of the Physical Society of Japan*, 76(7):073708, 2007.
- [22] K. Dunnett, Awadhesh Narayan, N. A. Spaldin, and A. V. Balatsky. Strain and ferroelectric soft-mode induced superconductivity in strontium titanate. *Physical Review B*, 97(14), April 2018.
- [23] E. Bauer, G. Rogl, Xing Qiu Chen, R. T. Khan, H. Michor, G. Hilscher, E. Royanian, K. Kumagai, D. Z. Li, Y. Y. Li, R. Podloucky, and P. Rogl. Unconventional superconducting phase in the weakly correlated noncentrosymmetric Mo₃Al₂C compound. *Physical Review B - Condensed Matter and Materials Physics*, 82(6):064511, 2010.
- [24] Carl Willem Rischau, Xiao Lin, Christoph P. Grams, Dennis Finck, Steffen Harms, Johannes Engelmayer, Thomas Lorenz, Yann Gallais, Benoît Fauqué, Joachim Hemberger, and Kamran Behnia. A ferroelectric quantum phase transition inside the superconducting dome of Sr_{1-x}Ca_xTiO_{3-δ}. *Nature Physics*, 13(7):643–648, April 2017.

- [25] Changjiang Liu, Xi Yan, Dafei Jin, Yang Ma, Haw-Wen Hsiao, Yulin Lin, Terence M. Bretz-Sullivan, Xianjing Zhou, John Pearson, Brandon Fisher, J. Samuel Jiang, Wei Han, Jian-Min Zuo, Jianguo Wen, Dillon D. Fong, Jirong Sun, Hua Zhou, and Anand Bhattacharya. Two-dimensional superconductivity and anisotropic transport at KTaO_3 (111) interfaces. *Science*, 371(6530):716–721, January 2021.
- [26] K. Ueno, S. Nakamura, H. Shimotani, H. T. Yuan, N. Kimura, T. Nojima, H. Aoki, Y. Iwasa, and M. Kawasaki. Discovery of superconductivity in KTaO_3 by electrostatic carrier doping. *Nature Nanotechnology*, 6(7):408–412, May 2011.
- [27] Dániel Varjas, Adolfo G. Grushin, Roni Ilan, and Joel E. Moore. Dynamical piezoelectric and magnetopiezoelectric effects in polar metals from Berry phases and orbital moments. *Physical Review Letters*, 117:257601, 2016.
- [28] Heng Gao, Youngkuk Kim, Jörn W. F. Venderbos, C. L. Kane, E. J. Mele, Andrew M. Rappe, and Wei Ren. Dirac-Weyl semimetal: Coexistence of Dirac and Weyl fermions in polar hexagonal ABC crystals. *Physical Review Letters*, 121(10), September 2018.
- [29] John Edward Lennard-Jones. On the forces between atoms and ions. *Proceedings of the Royal Society of London. Series A, Containing Papers of a Mathematical and Physical Character*, 109(752):584–597, December 1925.
- [30] Philip M. Morse. Diatomic molecules according to the wave mechanics. II. vibrational levels. *Physical Review*, 34(1):57–64, July 1929.
- [31] Max Born and Joseph E. Mayer. Zur gittertheorie der ionenkristalle. *Zeitschrift für Physik*, 75(1-2):1–18, January 1932.

- [32] P. Hohenberg and W. Kohn. Inhomogeneous electron gas. *Physical Review*, 136(3B):B864–B871, November 1964.
- [33] W. Kohn and L. J. Sham. Self-consistent equations including exchange and correlation effects. *Physical Review*, 140(4A):A1133–A1138, November 1965.
- [34] John P. Perdew, Adrienn Ruzsinszky, Gábor I. Csonka, Oleg A. Vydrov, Gustavo E. Scuseria, Lucian A. Constantin, Xiaolan Zhou, and Kieron Burke. Restoring the density-gradient expansion for exchange in solids and surfaces. *Physical Review Letters*, 100(13), April 2008.
- [35] Felix Bloch. über die quantenmechanik der elektronen in kristallgittern. *Zeitschrift für Physik*, 52(7-8):555–600, July 1929.
- [36] Yong Wang, Xiaohui Liu, J. D. Burton, Sitaram S. Jaswal, and Evgeny Y. Tsymbal. Ferroelectric instability under screened Coulomb interactions. *Physical Review Letters*, 109(24), December 2012.
- [37] Daniel Hickox-Young, Danilo Puggioni, and James M. Rondinelli. Persistent polar distortions from covalent interactions in doped BaTiO₃. *Physical Review B*, 102(1), July 2020.
- [38] Fabien Bruneval, Céline Varvenne, Jean-Paul Crocombette, and Emmanuel Clouet. Pressure, relaxation volume, and elastic interactions in charged simulation cells. *Physical Review B*, 91(2), January 2015.
- [39] Veronica F. Michel, Tobias Esswein, and Nicola A. Spaldin. Interplay between ferroelectricity and metallicity in BaTiO₃. *Journal of Materials Chemistry C*, 2021.
- [40] Xu He and Kui juan Jin. Persistence of polar distortion with electron doping in lone-pair driven ferroelectrics. *Physical Review B*, 94(22), December 2016.

- [41] Yoshiki Iwazaki, Toshimasa Suzuki, Youichi Mizuno, and Shinji Tsuneyuki. Doping-induced phase transitions in ferroelectric BaTiO₃ from first-principles calculations. *Physical Review B*, 86(21), December 2012.
- [42] J. Serre and A. Ghazali. From band tailing to impurity-band formation and discussion of localization in doped semiconductors: A multiple-scattering approach. *Physical Review B*, 28(8):4704–4715, October 1983.
- [43] A L Efros, Nguyen Van Lien, and B I Shklovskii. Impurity band structure in lightly doped semiconductors. *Journal of Physics C: Solid State Physics*, 12(10):1869–1881, May 1979.
- [44] Santosh Raghavan, Jack Y. Zhang, Omor F. Shoron, and Susanne Stemmer. Probing the metal-insulator transition in BaTiO₃ by electrostatic doping. *Physical Review Letters*, 117(3), July 2016.
- [45] J. Fujioka, A. Doi, D. Okuyama, D. Morikawa, T. Arima, K. N. Okada, Y. Kaneko, T. Fukuda, H. Uchiyama, D. Ishikawa, A. Q. R. Baron, K. Kato, M. Takata, and Y. Tokura. Ferroelectric-like metallic state in electron doped BaTiO₃. *Scientific Reports*, 5(1):13207, 2015.
- [46] T. Kolodiaznyy, M. Tachibana, H. Kawaji, J. Hwang, and E. Takayama-Muromachi. Persistence of ferroelectricity in BaTiO₃ through the insulator-metal transition. *Physical Review Letters*, 104(14):147602, 2010.
- [47] Katharine Page, Taras Kolodiaznyy, Thomas Proffen, Anthony K. Cheetham, and Ram Seshadri. Local structural origins of the distinct electronic properties of Nb-substituted SrTiO₃ and BaTiO₃. *Physical Review Letters*, 101(20), November 2008.

- [48] Aron Walsh and Alex Zunger. Instilling defect tolerance in new compounds. *Nature Materials*, 16(10):964–967, September 2017.
- [49] Augusto Marcelli, Marcello Coreno, Matus Stredansky, Wei Xu, Chongwen Zou, Lele Fan, Wangsheng Chu, Shiqiang Wei, Albano Cossaro, Alessandro Ricci, Antonio Bianconi, and Alessandro D’Elia. Nanoscale phase separation and lattice complexity in VO₂: The metal–insulator transition investigated by XANES via auger electron yield at the vanadium L₂₃-edge and resonant photoemission. *Condensed Matter*, 2(4):38, December 2017.
- [50] Salva Salmani-Rezaie, Kaveh Ahadi, and Susanne Stemmer. Polar nanodomains in a ferroelectric superconductor. *Nano Letters*, 20(9):6542–6547, August 2020.
- [51] P. P. Edwards, M. T.J. Lodge, F. Hensel, and R. Redmer. ... a metal conducts and a non-metal doesn’t. *Philosophical Transactions of the Royal Society A: Mathematical, Physical and Engineering Sciences*, 368(1914):941–965, 2010.
- [52] P. P. Edwards. *Nevill Mott: reminiscences and appreciations*. CRC Press, 1998.
- [53] K. S. Takahashi, Y. Matsubara, M. S. Bahramy, N. Ogawa, D. Hashizume, Y. Tokura, and M. Kawasaki. Polar metal phase stabilized in strained La-doped BaTiO₃ films. *Scientific Reports*, 7(1), July 2017.
- [54] T. Kolodiaznyi. Insulator-metal transition and anomalous sign reversal of the dominant charge carriers in perovskite BaTiO_{3- δ} . *Physical Review B*, 78(4), July 2008.
- [55] Walter Kohn. Theory of the insulating state. *Physical Review*, 133(1A), 1964.
- [56] Douglas J. Scalapino, Steven R. White, and Shoucheng Zhang. Insulator, metal, or superconductor: The criteria. *Phys. Rev. B*, 47:7995–8007, Apr 1993.

- [57] Raffaele Resta. Why are insulators insulating and metals conducting? *Journal of Physics Condensed Matter*, 14(20), 2002.
- [58] A. J. Millis and S. N. Coppersmith. Variational wave functions and the Mott transition. *Physical Review B*, 43(16):13770, 1991.
- [59] C. C. Homes, T. Timusk, R. Liang, D. A. Bonn, and W. N. Hardy. Optical conductivity of c axis oriented $\text{YBa}_2\text{Cu}_3\text{O}_{6.70}$: Evidence for a pseudogap. *Physical Review Letters*, 71(10):1645–1648, September 1993.
- [60] Cyrus E. Dreyer, Sinisa Coh, and Massimiliano Stengel. Nonadiabatic Born effective charges in metals and the Drude weight. arXiv:2103.04425[cond-mat.mtrl-sci], 2021.
- [61] William E. Anderson, Ralph W. Alexander, and Robert J. Bell. Surface plasmons and the reflectivity of n-type InSb. *Physical Review Letters*, 27(16):1057–1060, October 1971.
- [62] C Z Bi, J Y Ma, J Yan, X Fang, B R Zhao, D Z Yao, and X G Qiu. Electron–phonon coupling in Nb-doped SrTiO_3 single crystal. *Journal of Physics: Condensed Matter*, 18(8):2553–2561, February 2006.
- [63] I. Lo Vecchio, G. Giovannetti, M. Autore, P. Di Pietro, A. Perucchi, Jianfeng He, K. Yamaura, M. Capone, and S. Lupi. Electronic correlations in the ferroelectric metallic state of LiOsO_3 . *Physical Review B*, 93(16), April 2016.
- [64] Isaac B. Bersuker. Pseudo-Jahn–Teller effect—A two-state paradigm in formation, deformation, and transformation of molecular systems and solids. *Chemical Reviews*, 113(3):1351–1390, January 2013.

- [65] Ph Ghosez, X Gonze, and J.-P Michenaud. Coulomb interaction and ferroelectric instability of BaTiO₃. *Europhysics Letters (EPL)*, 33(9):713–718, March 1996.
- [66] Danilo Puggioni and James M. Rondinelli. Designing a robustly metallic noncentrosymmetric ruthenate oxide with large thermopower anisotropy. *Nat. Commun.*, 5:3432, 2013.
- [67] An american national standard IEEE standard definitions of terms associated with ferroelectric and related materials. *IEEE Transactions on Ultrasonics, Ferroelectrics and Frequency Control*, 50(12):1–32, December 2003.
- [68] V K Wadhawan. Ferroelasticity. *Bulletin of Materials Science*, 6(4):733–753, September 1984.
- [69] G Slosarek, A Heuer, H Zimmermann, and U Haebleren. A study of the paraelectric-ferroelectric phase transition of triglycine sulphate by deuteron nuclear magnetic resonance and relaxation. *Journal of Physics: Condensed Matter*, 1(34):5931–5954, August 1989.
- [70] Venkatraman Gopalan, Volkmar Dierolf, and David A. Scrymgeour. Defect–domain wall interactions in trigonal ferroelectrics. *Annual Review of Materials Research*, 37(1):449–489, August 2007.
- [71] K. Shapovalov, P. V. Yudin, A. K. Tagantsev, E. A. Eliseev, A. N. Morozovska, and N. Setter. Elastic coupling between nonferroelastic domain walls. *Physical Review Letters*, 113(20), November 2014.
- [72] J. F. Scott. Ferroelectrics go bananas. *Journal of Physics Condensed Matter*, 20(2):18–20, 2008.

- [73] Jun xing Gu, Kui juan Jin, Chao Ma, Qing hua Zhang, Lin Gu, Chen Ge, Jie su Wang, Can Wang, Hai zhong Guo, and Guo zhen Yang. Coexistence of polar distortion and metallicity in $\text{PbTi}_{1-x}\text{Nb}_x\text{O}_3$. *Physical Review B*, 96(16), October 2017.
- [74] Feng Jin, Le Wang, Anmin Zhang, Jianting Ji, Youguo Shi, Xiaoqun Wang, Rong Yu, Jiandi Zhang, E. W. Plummer, and Qingming Zhang. Raman interrogation of the ferroelectric phase transition in polar metal LiOsO_3 . *Proceedings of the National Academy of Sciences*, 116(41):20322–20327, September 2019.
- [75] Shiming Lei, Mingqiang Gu, Danilo Puggioni, Greg Stone, Jin Peng, Jianjian Ge, Yu Wang, Baoming Wang, Yakun Yuan, Ke Wang, Zhiqiang Mao, James M. Rondinelli, and Venkatesan Gopalan. Observation of quasi-two-dimensional polar domains and ferroelastic switching in a metal, $\text{Ca}_3\text{Ru}_2\text{O}_7$. *Nano Letters*, 18(5):3088–3095, 2018.
- [76] Alessio Filippetti, Vincenzo Fiorentini, Francesco Ricci, Pietro Delugas, and Jorge Íñiguez. Prediction of a native ferroelectric metal. *Nature Communications*, 7(1), April 2016.
- [77] Yue-Wen Fang and Hanghui Chen. Design of a multifunctional polar metal via first-principles high-throughput structure screening. *Communications Materials*, 1(1), February 2020.
- [78] Hikaru Watanabe and Youichi Yanase. Magnetic hexadecapole order and magnetopiezoelectric metal state in $\text{Ba}_{1-x}\text{K}_x\text{Mn}_2\text{As}_2$. *Physical Review B*, 96(6), August 2017.
- [79] E. Bauer, G. Hilscher, H. Michor, Ch. Paul, E. W. Scheidt, A. Griбанov, Yu. Seropegin, H. Noël, M. Sigrist, and P. Rogl. Heavy fermion superconductivity and magnetic order in noncentrosymmetric CePt_3Si . *Physical Review Letters*, 92(2), January 2004.

- [80] Yuanyuan Jiao, Yue-Wen Fang, Jianping Sun, Pengfei Shan, Zhenhai Yu, Hai L. Feng, Bosen Wang, Hanming Ma, Yoshiya Uwatoko, Kazunari Yamaura, Yanfeng Guo, Hanghui Chen, and Jinguang Cheng. Coupled magnetic and structural phase transitions in the antiferromagnetic polar metal $\text{Pb}_2\text{CoOsO}_6$ under pressure. *Physical Review B*, 102(14), October 2020.
- [81] Haricharan Padmanabhan, Yoonsang Park, Danilo Puggioni, Yakun Yuan, Yanwei Cao, Lev Gasparov, Youguo Shi, Jak Chakhalian, James M. Rondinelli, and Venkatraman Gopalan. Linear and nonlinear optical probe of the ferroelectric-like phase transition in a polar metal, LiOsO_3 . *Applied Physics Letters*, 113(12):122906, September 2018.
- [82] N. J. Laurita, A. Ron, Jun-Yi Shan, D. Puggioni, N. Z. Koocher, K. Yamaura, Y. Shi, J. M. Rondinelli, and D. Hsieh. Evidence for the weakly coupled electron mechanism in an Anderson-Blount polar metal. *Nature Communications*, 10(1), July 2019.
- [83] Feng Jin, Anmin Zhang, Jianting Ji, Kai Liu, Le Wang, Youguo Shi, Yong Tian, Xiaoli Ma, and Qingming Zhang. Raman phonons in the ferroelectric-like metal LiOsO_3 . *Physical Review B*, 93(6), February 2016.
- [84] Y. Pan, A. M. Nikitin, T. V. Bay, Y. K. Huang, C. Paulsen, B. H. Yan, and A. de Visser. Superconductivity and magnetic order in the noncentrosymmetric half-Heusler compound ErPdBi . *EPL (Europhysics Letters)*, 104(2):27001, October 2013.
- [85] Kaveh Ahadi, Luca Galletti, Yuntian Li, Salva Salmani-Rezaie, Wangzhou Wu, and Susanne Stemmer. Enhancing superconductivity in SrTiO_3 films with strain. *Science advances*, 5(4):eaaw0120, 2019.

- [86] J. F. Schooley, W. R. Hosler, and Marvin L. Cohen. Superconductivity in semiconducting SrTiO_3 . *Physical Review Letters*, 12(17):474–475, April 1964.
- [87] Shutong Li and Turan Birol. Free carrier induced ferroelectricity in layered perovskites, 2021.
- [88] Jun Jiang, Zi Long Bai, Zhi Hui Chen, Long He, David Wei Zhang, Qing Hua Zhang, Jin An Shi, Min Hyuk Park, James F. Scott, Cheol Seong Hwang, and An Quan Jiang. Temporary formation of highly conducting domain walls for non-destructive read-out of ferroelectric domain-wall resistance switching memories. *Nature Materials*, 17(1):49–56, November 2017.
- [89] T. Choi, Y. Horibe, H. T. Yi, Y. J. Choi, Weida Wu, and S.-W. Cheong. Insulating interlocked ferroelectric and structural antiphase domain walls in multiferroic YMnO_3 . *Nature Materials*, 9(3):253–258, February 2010.
- [90] Kai Jiang, Run Zhao, Peng Zhang, Qinglin Deng, Jinzhong Zhang, Wenwu Li, Zhigao Hu, Hao Yang, and Junhao Chu. Strain and temperature dependent absorption spectra studies for identifying the phase structure and band gap of EuTiO_3 perovskite films. *Physical Chemistry Chemical Physics*, 17(47):31618–31623, 2015.
- [91] Greg Stone, Danilo Puggioni, Shiming Lei, Mingqiang Gu, Ke Wang, Yu Wang, Jianjian Ge, Xue-Zeng Lu, Zhiqiang Mao, James M. Rondinelli, and Venkatraman Gopalan. Atomic and electronic structure of domains walls in a polar metal. *Physical Review B*, 99(1), January 2019.
- [92] Huafei Zheng, Brandon C. Wilfong, Daniel Hickox-Young, James M. Rondinelli, Peter Y. Zavalij, and Efrain E. Rodriguez. Polar ferromagnetic metal by intercalation of metal–amine complexes. *Chemistry of Materials*, 33(13):4936–4947, June 2021.

- [93] Hai L. Feng, Chang-Jong Kang, Pascal Manuel, Fabio Orlandi, Yu Su, Jie Chen, Yoshihiro Tsujimoto, Joke Hadermann, Gabriel Kotliar, Kazunari Yamaura, Emma E. McCabe, and Martha Greenblatt. Antiferromagnetic order breaks inversion symmetry in a metallic double perovskite, $\text{Pb}_2\text{NiOsO}_6$. *Chemistry of Materials*, 33(11):4188–4195, May 2021.
- [94] Yuan Cao, Valla Fatemi, Shiang Fang, Kenji Watanabe, Takashi Taniguchi, Efthimios Kaxiras, and Pablo Jarillo-Herrero. Unconventional superconductivity in magic-angle graphene superlattices. *Nature*, 556(7699):43–50, March 2018.
- [95] Salva Salmani-Rezaie, Luca Galletti, Timo Schumann, Ryan Russell, Hanbyeol Jeong, Yuntian Li, John W. Harter, and Susanne Stemmer. Superconductivity in magnetically doped SrTiO_3 . *Applied Physics Letters*, 118(20):202602, May 2021.
- [96] Henrik Jacobsen, Hai L. Feng, Andrew J. Princep, Marein C. Rahn, Yanfeng Guo, Jie Chen, Yoshitaka Matsushita, Yoshihiro Tsujimoto, Masahiro Nagao, Dmitry Khalyavin, Pascal Manuel, Claire A. Murray, Christian Donnerer, James G. Vale, Marco Moretti Sala, Kazunari Yamaura, and Andrew T. Boothroyd. Magnetically induced metal-insulator transition in $\text{Pb}_2\text{CaOsO}_6$. *Physical Review B*, 102(21), December 2020.
- [97] M. Zhu, J. Peng, W. Tian, T. Hong, Z. Q. Mao, and X. Ke. Tuning the competing phases of bilayer ruthenate $\text{Ca}_3\text{Ru}_2\text{O}_7$ via dilute Mn impurities and magnetic field. *Physical Review B*, 95(14), April 2017.
- [98] Shiming Lei, Shalinee Chikara, Danilo Puggioni, Jin Peng, Mengze Zhu, Mingqiang Gu, Weiwei Zhao, Yu Wang, Yakun Yuan, Hirofumi Akamatsu, Moses H. W. Chan, Xianglin Ke, Zhiqiang Mao, James M. Rondinelli, Marcelo Jaime, John Singleton, Franziska Weickert,

- Vivien S. Zapf, and Venkatraman Gopalan. Comprehensive magnetic phase diagrams of the polar metal $\text{Ca}_3(\text{Ru}_{0.95}\text{Fe}_{0.05})_2\text{O}_7$. *Physical Review B*, 99(22), June 2019.
- [99] S. Tsuda, N. Kikugawa, K. Sugii, S. Uji, S. Ueda, M. Nishio, and Y. Maeno. Mott transition extremely sensitive to impurities in $\text{Ca}_3\text{Ru}_2\text{O}_7$ revealed by hard x-ray photoemission studies. *Physical Review B*, 87(24), June 2013.
- [100] Gianluca Giovannetti, Danilo Puggioni, James M. Rondinelli, and Massimo Capone. Interplay between electron correlations and polar displacements in metallic $\text{SrEuMo}_2\text{O}_6$. *Physical Review B*, 93(11), March 2016.
- [101] Danilo Puggioni, Gianluca Giovannetti, Massimo Capone, and James M. Rondinelli. Design of a Mott multiferroic from a nonmagnetic polar metal. *Physical Review Letters*, 115(8), August 2015.
- [102] Oleksandr I. Malyi, Gustavo M. Dalpian, Xin-Gang Zhao, Zhi Wang, and Alex Zunger. Realization of predicted exotic materials: The burden of proof. *Materials Today*, 32:35–45, January 2020.
- [103] Daniel Hickox-Young, Danilo Puggioni, and James M. Rondinelli. Persistent polar distortions from covalent interactions in doped BaTiO_3 . *Physical Review B*, 102(1), July 2020.
- [104] T. H. Kim, D. Puggioni, Y. Yuan, L. Xie, H. Zhou, N. Campbell, P. J. Ryan, Y. Choi, J.-W. Kim, J. R. Patzner, S. Ryu, J. P. Podkaminer, J. Irwin, Y. Ma, C. J. Fennie, M. S. Rzchowski, X. Q. Pan, V. Gopalan, J. M. Rondinelli, and C. B. Eom. Polar metals by geometric design. *Nature*, 533(7601):68–72, April 2016.

- [105] Hu Zhang, Bei Deng, Wei Chao Wang, and Xing Qiang Shi. Parity-breaking in single-element phases: Ferroelectric-like elemental polar metals. *Journal of Physics Condensed Matter*, 30(415504), 2018.
- [106] F. Cordero, F. Trequattrini, F. Craciun, H. T. Langhammer, D. A. B. Quiroga, and P. S. Silva. Probing ferroelectricity in highly conducting materials through their elastic response: Persistence of ferroelectricity in metallic $\text{BaTiO}_{3-\delta}$. *Phys. Rev. B*, 99:064106, Feb 2019.
- [107] Hong Jian Zhao, Alessio Filippetti, Carlos Escorihuela-Sayalero, Pietro Delugas, Enric Canadell, L. Bellaiche, Vincenzo Fiorentini, and Jorge Íñiguez. Meta-screening and permanence of polar distortion in metallized ferroelectrics. *Physical Review B*, 97(5):054107, 2018.
- [108] Isaac Bersuker. *The Jahn-Teller effect and vibronic interactions in modern chemistry*. Springer Science & Business Media, 2013.
- [109] Jeremy K. Burdett. Use of the Jahn-Teller theorem in inorganic chemistry. *Inorganic Chemistry*, 20(7):1959–1962, 1981.
- [110] Nicola Marzari, Arash A. Mostofi, Jonathan R. Yates, Ivo Souza, and David Vanderbilt. Maximally localized Wannier functions: Theory and applications. *Reviews of Modern Physics*, 84(4):1419–1475, October 2012.
- [111] R. H. Buttner and E. N. Maslen. Structural parameters and electron difference density in BaTiO_3 . *Acta Crystallographica Section B Structural Science*, 48(6):764–769, December 1992.
- [112] M.E. Lines and A.M. Glass. *Principles and Applications of Ferroelectrics and Related Materials*. Clarendon, Oxford, 1977.

- [113] Y. Luspin, J .L. Servoin, and F. Gervais. Soft mode spectroscopy in barium titanate. *Journal of Physics C: Solid State Physics*, 13:3761–3773, 1980.
- [114] Robert A. Evarestov and Andrei V. Bandura. First-principles calculations on the four phases of BaTiO₃. *Journal of Computational Chemistry*, 33(11):1123–1130, February 2012.
- [115] Yubo Zhang, Jianwei Sun, John P. Perdew, and Xifan Wu. Comparative first-principles studies of prototypical ferroelectric materials by LDA, GGA, and SCAN meta-GGA. *Physical Review B*, 96(3), July 2017.
- [116] V. Polinger, P. Garcia-Fernandez, and I.B. Bersuker. Pseudo Jahn–Teller origin of ferroelectric instability in BaTiO₃ type perovskites: The Green’s function approach and beyond. *Physica B: Condensed Matter*, 457:296–309, January 2015.
- [117] T. Ishidate, S. Abe, H. Takahashi, and N. Môri. Phase diagram of BaTiO₃. *Physical Review Letters*, 78(12):2397–2400, March 1997.
- [118] G. Kresse and J. Furthmüller. Efficient iterative schemes for ab initio total-energy calculations using a plane-wave basis set. *Physical Review B*, 54(16):11169–11186, October 1996.
- [119] G. Kresse and D. Joubert. From ultrasoft pseudopotentials to the projector augmented-wave method. *Physical Review B*, 59(3):1758–1775, January 1999.
- [120] P. E. Blöchl. Projector augmented-wave method. *Physical Review B*, 50(24):17953–17979, December 1994.
- [121] Atsushi Togo and Isao Tanaka. First principles phonon calculations in materials science. *Scripta Materialia*, 108:1–5, November 2015.

- [122] Volker L. Deringer, Andrei L. Tchougréeff, and Richard Dronskowski. Crystal orbital hamilton population (COHP) analysis as projected from plane-wave basis sets. *The Journal of Physical Chemistry A*, 115(21):5461–5466, June 2011.
- [123] Stefan Maintz, Volker L. Deringer, Andrei L. Tchougréeff, and Richard Dronskowski. LOBSTER: A tool to extract chemical bonding from plane-wave based DFT. *Journal of Computational Chemistry*, 37(11):1030–1035, February 2016.
- [124] Stefan Maintz, Marc Esser, and Richard Dronskowski. Efficient rotation of local basis functions using real spherical harmonics. *Acta Physica Polonica B*, 47(4), 2016.
- [125] Stefan Maintz, Volker L. Deringer, Andrei L. Tchougréeff, and Richard Dronskowski. Analytic projection from plane-wave and PAW wavefunctions and application to chemical-bonding analysis in solids. *Journal of Computational Chemistry*, 34(29):2557–2567, September 2013.
- [126] Giovanni Pizzi, Valerio Vitale, Ryotaro Arita, Stefan Blügel, Frank Freimuth, Guillaume Géranton, Marco Gibertini, Dominik Gresch, Charles Johnson, Takashi Koretsune, Julen Ibañez-Azpiroz, Hyungjun Lee, Jae-Mo Lihm, Daniel Marchand, Antimo Marrazzo, Yuriy Mokrousov, Jamal I Mustafa, Yoshiro Nohara, Yusuke Nomura, Lorenzo Paulatto, Samuel Poncé, Thomas Ponweiser, Junfeng Qiao, Florian Thöle, Stepan S Tsirkin, Małgorzata Wierzbowska, Nicola Marzari, David Vanderbilt, Ivo Souza, Arash A Mostofi, and Jonathan R Yates. Wannier90 as a community code: new features and applications. *Journal of Physics: Condensed Matter*, 32(16):165902, January 2020.
- [127] Arash A. Mostofi, Jonathan R. Yates, Giovanni Pizzi, Young-Su Lee, Ivo Souza, David Vanderbilt, and Nicola Marzari. An updated version of wannier90: A tool for obtaining

- maximally-localised Wannier functions. *Computer Physics Communications*, 185(8):2309–2310, August 2014.
- [128] Hannes Raebiger, Stephan Lany, and Alex Zunger. Charge self-regulation upon changing the oxidation state of transition metals in insulators. *Nature*, 453(7196):763–766, June 2008.
- [129] Renu Kumari, Pawan Kumar Kulriya, Surubala Mishra, Vasundhara Kotari, Srungarpu N. Achary, Avesh K. Tyagi, and Devesh K. Avasthi. Phase-dependent radiation-resistant behavior of BaTiO₃: An in situ x-ray diffraction study. *Journal of the American Ceramic Society*, 100(9):4263–4269, May 2017.
- [130] Craig J. Fennie and Karin M. Rabe. Magnetic and electric phase control in epitaxial EuTiO₃ from first principles. *Physical Review Letters*, 97(26), December 2006.
- [131] June Hyuk Lee, Lei Fang, Eftihia Vlahos, Xianglin Ke, Young Woo Jung, Lena Fitting Kourkoutis, Jong-Woo Kim, Philip J Ryan, Tassilo Heeg, Martin Roeckerath, et al. A strong ferroelectric ferromagnet created by means of spin–lattice coupling. *Nature*, 466(7309):954, 2010.
- [132] Hirofumi Akamatsu, Yu Kumagai, Fumiyasu Oba, Koji Fujita, Hideo Murakami, Katsuhisa Tanaka, and Isao Tanaka. Antiferromagnetic superexchange via 3 *d* states of titanium in EuTiO₃ as seen from hybrid Hartree-Fock density functional calculations. *Physical Review B*, 83(21):214421, 2011.
- [133] A. I. Liechtenstein, V. I. Anisimov, and J. Zaanen. Density-functional theory and strong interactions: Orbital ordering in Mott-Hubbard insulators. *Physical Review B*, 52(8):R5467–R5470, August 1995.

- [134] June Hyuk Lee, Lei Fang, Eftihia Vlahos, Xianglin Ke, Young Woo Jung, Lena Fitting Kourkoutis, Jong-Woo Kim, Philip J. Ryan, Tassilo Heeg, Martin Roeckerath, Veronica Goian, Margitta Bernhagen, Reinhard Uecker, P. Chris Hammel, Karin M. Rabe, Stanislav Kamba, Jürgen Schubert, John W. Freeland, David A. Muller, Craig J. Fennie, Peter Schiffer, Venkatesan Gopalan, Ezekiel Johnston-Halperin, and Darrell G. Schlom. A strong ferroelectric ferromagnet created by means of spin–lattice coupling. *Nature*, 466(7309):954–958, August 2010.
- [135] Yurong Yang, Wei Ren, Dawei Wang, and L. Bellaiche. Understanding and revisiting properties of EuTiO_3 bulk material and films from first principles. *Physical Review Letters*, 109(26), December 2012.
- [136] J. C. Slater. The Lorentz correction in barium titanate. *Physical Review*, 78(6):748–761, June 1950.
- [137] Kaveh Ahadi, Luca Galletti, and Susanne Stemmer. Evidence of a topological Hall effect in $\text{Eu}_{1-x}\text{Sm}_x\text{TiO}_3$. *Applied Physics Letters*, 111(17):172403, October 2017.
- [138] Bharat Jalan, Roman Engel-Herbert, Nicholas J Wright, and Susanne Stemmer. Growth of high-quality SrTiO_3 films using a hybrid molecular beam epitaxy approach. *Journal of Vacuum Science & Technology A: Vacuum, Surfaces, and Films*, 27(3):461–464, 2009.
- [139] P. A. Franken, A. E. Hill, C. W. Peters, and G. Weinreich. Generation of optical harmonics. *Physical Review Letters*, 7(4):118–119, August 1961.

- [140] Stefan W Hell and Jan Wichmann. Breaking the diffraction resolution limit by stimulated emission: stimulated-emission-depletion fluorescence microscopy. *Optics letters*, 19(11):780–782, 1994.
- [141] E Beaurepaire, J-C Merle, A Daunois, and J-Y Bigot. Ultrafast spin dynamics in ferromagnetic nickel. *Physical review letters*, 76(22):4250, 1996.
- [142] Salva Salmani-Rezaie, Kaveh Ahadi, William M. Strickland, and Susanne Stemmer. Order-disorder ferroelectric transition of strained SrTiO₃. *Physical Review Letters*, 125(8), August 2020.
- [143] I.-K. Jeong, Seunghun Lee, Se-Young Jeong, C. J. Won, N. Hur, and A. Llobet. Structural evolution across the insulator-metal transition in oxygen-deficient BaTiO_{3-δ} studied using neutron total scattering and rietveld analysis. *Physical Review B*, 84(6), August 2011.
- [144] Yanan Geng, J. H. Lee, D. G. Schlom, J. W. Freeland, and Weida Wu. Magnetic inhomogeneity in a multiferroic EuTiO₃ thin film. *Physical Review B*, 87(12), March 2013.
- [145] Michael Porer, Michael Fechner, Martin Kubli, Martin J Neugebauer, Sergii Parchenko, Vincent Esposito, Awadhesh Narayan, Nicola A Spaldin, Rupert Huber, Milan Radovic, et al. Ultrafast transient increase of oxygen octahedral rotations in a perovskite. *Physical Review Research*, 1(1):012005, 2019.
- [146] S Muhlbauer, B Binz, F Jonietz, C Pfleiderer, A Rosch, A Neubauer, R Georgii, and P Boni. Skyrmion lattice in a chiral magnet. *Science*, 323(5916):915–919, 2009.

- [147] E. Bauer, R. T. Khan, H. Michor, E. Royanian, A. Grytsiv, N. Melnychenko-Koblyuk, P. Rogl, D. Reith, R. Podloucky, E.-W. Scheidt, W. Wolf, and M. Marsman. BaPtSi₃: A noncentrosymmetric BCS-like superconductor. *Physical Review B*, 80(6), August 2009.
- [148] Yoshichika Ōnuki, Yuuichiro Miyauchi, Masahiko Tsujino, Yuki Ida, Rikio Settai, Tetsuya Takeuchi, Naoyuki Tateiwa, Tatsuma D. Matsuda, Yoshinori Haga, and Hisatomo Harima. Superconducting properties of CePt₃Si and CeIrSi₃ without inversion symmetry in the crystal structure. *Journal of the Physical Society of Japan*, 77(Suppl.A):37–42, January 2008.
- [149] Noriaki Kimura, Yuji Muro, and Haruyoshi Aoki. Normal and superconducting properties of noncentrosymmetric heavy fermion CeRhSi₃. *Journal of the Physical Society of Japan*, 76(5):051010, May 2007.
- [150] Y. Okuda, I. Sugitani, H. Shishido, T. Yamada, A. Thamizhavel, E. Yamamoto, T.D. Matsuda, Y. Haga, T. Takeuchi, R. Settai, and Y. Ōnuki. Magnetic and superconducting properties of and without inversion symmetry. *Journal of Magnetism and Magnetic Materials*, 310(2):563–565, March 2007.
- [151] H. Schaal, J. Nuss, W. Hönle, Yu. Grin, and H. G. von Schnering. Crystal structure of tetraeuropium diantimonide oxide, Eu₄Sb₂O. *Zeitschrift für Kristallographie - New Crystal Structures*, 213(1-4):15, April 1998.
- [152] C. Röhr and R. George. Crystal structure of barium antimonide oxide, Ba₄Sb₂O. *Zeitschrift für Kristallographie - Crystalline Materials*, 211(7):478–478, July 1996.

- [153] Jürgen Nuss, Ulrich Wedig, and Martin Jansen. Geometric variations and electron localizations in intermetallics: The case of La_2Sb type compounds. *Zeitschrift für anorganische und allgemeine Chemie*, 637(13):1975–1981, October 2011.
- [154] U. Burkhardt, M. Wied, W. Höhle, Yu. Grin, and H. G. von Schnering. Crystal structure of tetraytterbium diarsenide oxide, $\text{Yb}_4\text{As}_2\text{O}$. *Zeitschrift für Kristallographie - New Crystal Structures*, 213(1-4):13, April 1998.
- [155] W. Höhle, H. Schaal, and H. G. von Schnering. Crystal structure of tetraeuropium dibismuthide oxide, $\text{Eu}_4\text{Bi}_2\text{O}$. *Zeitschrift für Kristallographie - New Crystal Structures*, 213(1-4):16, April 1998.
- [156] Y. Wang, L. D. Calvert, E. J. Gabe, and J. B. Taylor. Europium arsenic oxide $\text{Eu}_4\text{As}_2\text{O}$: a filled La_2Sb structure and its relation to the K_2NiF_4 and GeTeU types. *Acta Crystallographica Section B Structural Crystallography and Crystal Chemistry*, 33(10):3122–3125, October 1977.
- [157] Maxime Markov, Louis Alaerts, Henrique Pereira Coutada Miranda, Guido Petretto, Wei Chen, Janine George, Eric Bousquet, Philippe Ghosez, Gian-Marco Rignanese, and Geoffroy Hautier. Ferroelectricity and multiferroicity in anti-Ruddlesden-Popper structures. *Proceedings of the National Academy of Sciences*, 118(17):e2026020118, April 2021.
- [158] Youngho Kang and Seungwu Han. Antiperovskite oxides as promising candidates for high-performance ferroelectric photovoltaics: First-principles investigation on $\text{Ba}_4\text{As}_2\text{O}$ and $\text{Ba}_4\text{Sb}_2\text{O}$. *ACS Applied Materials & Interfaces*, 12(39):43798–43804, September 2020.
- [159] K. V. Samokhin, E. S. Zijlstra, and S. K. Bose. CePt_3Si : An unconventional superconductor without inversion center. *Physical Review B*, 69(9), March 2004.

- [160] G Rogl, D Legut, R Sýkora, P Müller, H Müller, E Bauer, S Puchegger, M Zehetbauer, and P Rogl. Mechanical properties of non-centrosymmetric CePt₃Si and CePt₃B. *Journal of Physics: Condensed Matter*, 29(18):185402, April 2017.
- [161] N Metoki, K Kaneko, T D Matsuda, A Galatanu, T Takeuchi, S Hashimoto, T Ueda, R Settai, Y nuki, and N Bernhoeft. Magnetic structure and the crystal field excitation in heavy-fermion antiferromagnetic superconductor CePt₃Si. *Journal of Physics: Condensed Matter*, 16(15):L207–L212, April 2004.
- [162] Tetsuya Takeuchi, Masato Shiimoto, Hisanori Kohara, Takashi Yasuda, Shin Hashimoto, Rikio Settai, and Yoshichika Ōnuki. Magnetism and superconductivity in CePt₃Si under pressure. *Journal of the Physical Society of Japan*, 75(Suppl):170–173, January 2006.
- [163] Dante M. Kennes, Martin Claassen, Lede Xian, Antoine Georges, Andrew J. Millis, James Hone, Cory R. Dean, D. N. Basov, Abhay N. Pasupathy, and Angel Rubio. Moiré heterostructures as a condensed-matter quantum simulator. *Nature Physics*, 17(2):155–163, February 2021.
- [164] Michael A. Susner, Marius Chyasnovichyus, Michael A. McGuire, Panchapakesan Ganesh, and Petro Maksymovych. Metal thio- and selenophosphates as multifunctional van der Waals layered materials. *Advanced Materials*, 29(38):1602852, August 2017.
- [165] Kin Fai Mak, Jie Shan, and Daniel C. Ralph. Probing and controlling magnetic states in 2d layered magnetic materials. *Nature Reviews Physics*, 1(11):646–661, September 2019.
- [166] Cheng Gong and Xiang Zhang. Two-dimensional magnetic crystals and emergent heterostructure devices. *Science*, 363(6428):eaav4450, February 2019.

- [167] Tao Xu, Jingtong Zhang, Yuquan Zhu, Jie Wang, Takahiro Shimada, Takayuki Kitamura, and Tong-Yi Zhang. Two-dimensional polar metal of a PbTe monolayer by electrostatic doping. *Nanoscale Horizons*, 5(10):1400–1406, 2020.
- [168] Mao Ye, Songbai Hu, Shanming Ke, Yuanmin Zhu, Yubo Zhang, Lin Xie, Yuan Zhang, Dongwen Zhang, Zhenlin Luo, Meng Gu, Jiaqing He, Peihong Zhang, Wenqing Zhang, and Lang Chen. Observation of a room temperature two-dimensional ferroelectric metal. arXiv:1908.08726[cond-mat.mtrl-sci], 2019.
- [169] Wei Luo, Ke Xu, and Hongjun Xiang. Two-dimensional hyperferroelectric metals: A different route to ferromagnetic-ferroelectric multiferroics. *Physical Review B*, 96(23), December 2017.
- [170] Jinlian Lu, Gong Chen, Wei Luo, Jorge Íñiguez, Laurent Bellaiche, and Hongjun Xiang. Ferroelectricity with asymmetric hysteresis in metallic LiOsO₃ ultrathin films. *Physical Review Letters*, 122(22), June 2019.
- [171] S. Ranganathan. On the geometry of coincidence-site lattices. *Acta Crystallographica*, 21(2):197–199, August 1966.
- [172] Jos E. Boschker, Lauren A. Galves, Timur Flissikowski, Joao Marcelo J. Lopes, Henning Riechert, and Raffaella Calarco. Coincident-site lattice matching during van der Waals epitaxy. *Scientific Reports*, 5(1), December 2015.
- [173] D Bernard, J Lucas, and L Rivoallan. Les pyrochlores ferroelectriques derives de Cd₂Nb₂O₆S: mise en evidence des transitions de phase par des techniques d’optique non lineaire. *Solid State Communications*, 18:927–930, 1976.

- [174] Sébastien Saitzek, Zhenmian Shao, Alexandre Bayart, Anthony Ferri, Marielle Huvé, Pascal Roussel, and Rachel Desfeux. Ferroelectricity in $\text{La}_2\text{Zr}_2\text{O}_7$ thin films with a frustrated pyrochlore-type structure. *Journal of Materials Chemistry C*, 2(20):4037–4043, 2014.
- [175] X. W. Dong, K. F. Wang, S. J. Luo, J. G. Wan, and J. M. Liu. Coexistence of magnetic and ferroelectric behaviors of pyrochlore $\text{Ho}_2\text{Ti}_2\text{O}_7$. *Journal of Applied Physics*, 106(10), 2009.
- [176] Jesse C. Petersen, Michael D. Caswell, J. Steven Dodge, Ivan A. Sergienko, Jian He, Rongying Jin, and David Mandrus. Nonlinear optical signatures of the tensor order in $\text{Cd}_2\text{Re}_2\text{O}_7$. *Nature Physics*, 2(9):605–608, 2006.
- [177] Yasuyuki Hirata, Makoto Nakajima, Yusuke Nomura, Hiroyuki Tajima, Yoshitaka Matsushita, Keiko Asoh, Yoko Kiuchi, Adolfo G. Eguiluz, Ryotaro Arita, Tohru Suemoto, and Kenya Ohgushi. Mechanism of enhanced optical second-harmonic generation in the conducting pyrochlore-type $\text{Pb}_2\text{Ir}_2\text{O}_{7-x}$ oxide compound. *Physical Review Letters*, 110(18):187402, 2013.
- [178] Geneva Laurita, Daniel Hickox-Young, Samra Husremovic, Jun Li, Arthur W. Sleight, Robin Macaluso, James M. Rondinelli, and Mas A. Subramanian. Covalency-driven structural evolution in the polar pyrochlore series $\text{Cd}_2\text{Nb}_2\text{O}_{7-x}\text{S}_x$. *Chemistry of Materials*, 31(18):7626–7637, August 2019.
- [179] Makoto Tachibana, Hitoshi Kawaji, and Tooru Atake. Calorimetric investigation of successive phase transitions in $\text{Cd}_2\text{Nb}_2\text{O}_7$. *Physical Review B*, 70(6), August 2004.

- [180] E. Buixaderas, S. Kamba, J. Petzelt, M. Savinov, and N.N. Kolpakova. Phase transitions sequence in pyrochlore $\text{Cd}_2\text{Nb}_2\text{O}_7$ studied by IR reflectivity. *The European Physical Journal B*, 19(1):9–16, January 2001.
- [181] T Malcherek, U Bismayer, and C Paulmann. The crystal structure of $\text{Cd}_2\text{Nb}_2\text{O}_7$: symmetry mode analysis of the ferroelectric phase. *Journal of Physics: Condensed Matter*, 22(20):205401, April 2010.
- [182] Kenya Ohgushi, Jun ichi Yamaura, Masaki Ichihara, Yoko Kiuchi, Takashi Tayama, Toshiro Sakakibara, Hirotada Gotou, Takehiko Yagi, and Yutaka Ueda. Structural and electronic properties of pyrochlore-type $\text{A}_2\text{Re}_2\text{O}_7$ (A=Ca, Cd, and Pb). *Physical Review B*, 83(12), March 2011.
- [183] Bo Peng, Yuchen Hu, Shuichi Murakami, Tiantian Zhang, and Bartomeu Monserrat. Topological phonons in oxide perovskites controlled by light. *Science Advances*, 6(46):eabd1618, November 2020.

Appendix A: Clarifying the intersection between acentricity and metallicity

TABLE A.1: Table of all published polar compounds exhibiting metallic conductivity. Columns denote space group (SG), presence of a polar structural phase transition (T_c), presence of a superconducting transition (T_{sc}), and presence of a magnetic ordering transition (T_N), respectively. Under SG: * = only the point group is known; “unknown” = the specific symmetry elements are unknown but there is evidence of broken inversion symmetry. Under T_c : P = compound is predicted but has not yet been synthesized. Under Class, the following abbreviations are in use: FE=ferroelectric; E=extrinsic; D=distortive; and A=anisotropic.

Composition	SG	T_c	T_{sc}	T_N	Class	DOI
BaTiO ₃ (La-doped)	<i>P4mm</i>	yes			doped FE	DOI:10.1038/s41598-017-04635-3
BaTiO _{3-d}	<i>P4mm</i>	yes			doped FE	10.1103/PhysRevLett.104.147602
PbTiO _{3-d}	<i>P4mm</i>	P			E polar metal	10.1103/PhysRevB.94.224107
PbTi _{1-x} Nb _x O ₃	<i>P4mm</i>				E polar metal	10.1103/PhysRevB.96.165206
BiFeO _{3-d}	<i>R3c</i>	P		yes	E polar metal	10.1103/PhysRevB.93.174110
Sr _{1-x} Ca _x TiO _{3-d}	<i>P4mm</i>	yes	yes		D polar metal	10.1038/NPHYS4085
BaMnO ₃ (n-doped)	<i>Amm2</i>	P			E polar metal	10.1103/PhysRevB.97.054107
BiAlO ₃ (n-doped)	<i>P4mm</i>	P			E polar metal	10.1103/PhysRevB.97.054107
BaTiO ₃ /SrTiO ₃ /LaTiO ₃	<i>mm4*</i>				AE polar metal	10.1038/s41467-018-03964-9
LaAlO ₃ /BaSr _{0.8} TiO ₃ /SrTiO ₃	<i>unknown</i>				AE polar metal	10.1038/s42005-019-0227-4
LaFeO ₃ /YFeO ₃ (n-doped)	<i>Pmc2₁</i>	P			E polar metal	10.1103/PhysRevB.97.054107
NdNiO ₃	<i>Pc</i>				polar metal	10.1038/nature17628
LaNiO ₃	<i>Pc</i>				polar metal	10.1038/nature17628
LiOsO ₃	<i>R3c</i>	yes			D polar metal	10.1038/NMAT3754
LiNbO ₃ (n-doped)	<i>R3c</i>	P			doped FE	10.1103/PhysRevMaterials.3.054405
MgReO ₃	<i>R3c</i>	P			polar metal	10.1103/PhysRevB.90.094108
TiGaO ₃	<i>R3c</i>	P			polar metal	10.1103/PhysRevB.90.094108
Ca ₃ Ru ₂ O ₇	<i>Bb2₁m</i>			yes	polar metal	10.1021/acs.nanolett.8b00633
(Sr,Ca)Ru ₂ O ₆	<i>Pmc2₁</i>	P		yes	polar metal	10.1088/0953-8984/26/26/265501
Bi ₅ Ti ₅ O ₁₇	<i>Pm2₁n</i>	P			A polar metal	10.1038/ncomms11211
BiPbTi ₂ O ₆	<i>Pmm2</i>	P			polar metal	10.1038/s43246-019-0005-6
La ₂ Ti ₂ O ₇ (n-doped)	<i>P2₁</i>	P			E polar metal	10.1103/PhysRevB.97.054107
Sr ₂ Nb ₂ O ₇ (n-doped)	<i>Cmc2₁</i>	P			E polar metal	10.1103/PhysRevB.97.054107
MgCNi ₃	<i>P4mm</i>	P			polar metal	10.1103/PhysRevMaterials.2.125004
ZnCNi ₃	<i>P4mm</i>	P			polar metal	10.1103/PhysRevMaterials.2.125004
CdCNi ₃	<i>P4mm</i>	P			polar metal	10.1103/PhysRevMaterials.2.125004
CeSiPt ₃	<i>P4mm</i>		yes	yes	polar metal	10.1103/PhysRevLett.92.027003
LiGaGe	<i>P6₃mc</i>				polar metal	10.1103/PhysRevB.99.195154

SrHgPb	$P6_3mc$	P			polar metal	10.1103/PhysRevLett.121.106404
SrHgSn	$P6_3mc$	P			polar metal	10.1103/PhysRevLett.121.106404
CaHgSn	$P6_3mc$	P			polar metal	10.1103/PhysRevLett.121.106404
KMgSb _{0.2} Bi _{0.8}	$P6_3mc$	P			polar metal	10.1103/PhysRevLett.117.076401
CaAgBi	$P6_3mc$	P			polar metal	10.1103/PhysRevMaterials.1.044201
LiZnBi	$P6_3mc$	P			polar metal	10.1103/PhysRevB.96.115203
LaAuGe	$P6_3mc$				polar metal	10.1063/1.5132339
LaPtSb	$P6_3mc$				polar metal	10.1063/1.5132339
WTe ₂	$Pnm2_1$	yes	yes		A polar metal	10.1038/s41586-018-0336-3
MoTe ₂	$Pnm2_1$	yes			polar metal	10.1126/sciadv.1601378
CrN	$6mm^*$			yes	A polar metal	10.1103/PhysRevB.96.235415
CrB ₂	$6mm^*$	P		yes	A polar metal	10.1103/PhysRevB.96.235415
FeB ₂	$6mm^*$				A polar metal	10.1021/acs.nanolett.6b02335
P	$P6_3mc$	P			polar metal	10.1088/1361-648X/aadeaa
As	$P6_3mc$	P			polar metal	10.1088/1361-648X/aadeaa
Sb	$P6_3mc$	P			polar metal	10.1088/1361-648X/aadeaa
Bi	$P6_3mc$	P			polar metal	10.1088/1361-648X/aadeaa
SnP	$I4mm$	yes	yes		D polar metal	10.1103/PhysRevLett.119.207001
PdBi	$P2_1$		yes		polar metal	10.1016/j.phpro.2013.04.062
UIr	$P2_1$		yes	yes	polar metal	10.1007/978-3-642-24624-1_2
LaNiC ₂	$Amm2$		yes	yes	polar metal	10.1016/j.physc.2014.01.008
NdRhC ₂	$Amm2$			yes	polar metal	10.1021/cm00006a007
PrRhC ₂	$Amm2$			yes		10.1021/cm00006a007
LnSr ₂ Cu ₂ GaO ₇ (Ln=La-Yb and Y)	$Ima2$		yes	yes	polar metal	10.1021/cm00017a032
V ₂ Hf	$Imm2$	yes	yes		D polar metal	10.1103/PhysRevB.17.1136
Li ₂ IrSi ₃	$P3_1c$			yes	polar metal	10.7566/JPSJ.83.093706
Mg ₂ Al ₃	$R3m$	yes	yes		D polar metal	10.1103/PhysRevB.76.014528
La ₅ B ₂ C ₆	$P4$			yes	polar metal	10.1016/0022-5088(83)90520-9
BaPtSi ₃	$I4mm$			yes	polar metal	10.1103/PhysRevB.80.064504
CeIrSi ₃	$I4mm$		yes	yes	polar metal	10.1143/JPSJS.77SA.37
CeRhSi ₃	$I4mm$		yes	yes	polar metal	10.1143/JPSJ.76.051010
LaPtSi ₃	$I4mm$			yes	polar metal	10.1103/PhysRevB.89.094509
LaPdSi ₃	$I4mm$			yes	polar metal	10.1103/PhysRevB.89.094509

CeIrGe ₃	<i>I4mm</i>	yes	yes	polar metal	10.1016/j.jmmm.2006.10.151
EuNiGe ₃	<i>I4mm</i>		yes	polar metal	10.1103/PhysRevB.87.064406
LaRhGe ₃	<i>I4mm</i>			polar metal	10.1063/5.0042924
IrRhGe ₃	<i>I4mm</i>			polar metal	10.1063/5.0042924
PdRhGe ₃	<i>I4mm</i>			polar metal	10.1063/5.0042924
SrPdGe ₃	<i>I4mm</i>	yes		polar metal	10.1088/1742-6596/273/1/012078
SrPtGe ₃	<i>I4mm</i>	yes		polar metal	10.1088/1742-6596/273/1/012078
PrPdIn ₂	<i>I4mm</i>		yes	polar metal	10.1021/cm031139m
CePt ₃ Si	<i>I4mm</i>	yes	yes	polar metal	10.1103/PhysRevLett.92.027003
Li ₂ (Pd _{1-x} Pt _x) ₃ B	<i>I4mm</i>	yes	yes	polar metal	10.1088/1742-6596/400/2/022096
KCu ₇ P ₃	<i>P3₁m</i>			polar metal	10.1021/acs.inorgchem.9b01336
Bi ₂ FeCrO ₆	<i>R3</i>	P	yes	polar metal	10.1103/PhysRevLett.123.107201
CeAuGe	<i>P6₃mc</i>		yes	polar metal	10.1016/0304-8853(95)00430-0
LuAuGe	<i>P6₃mc</i>			polar metal	10.1016/0925-8388(95)02069-1
ScAuGe	<i>P6₃mc</i>			polar metal	10.1016/0925-8388(95)02069-1
HoAuGe	<i>P6₃mc</i>		yes	polar metal	10.1088/0953-8984/13/11/315
CeCuSn	<i>P6₃mc</i>			polar metal	10.1016/j.jallcom.2004.09.086
La ₁₅ Ge ₉ C	<i>P6₃mc</i>			polar metal	10.1016/j.jallcom.2011.03.092
La ₁₅ Ge ₉ Fe	<i>P6₃mc</i>		yes	polar metal	10.1021/ic9515158
La ₁₅ Ge ₉ Co	<i>P6₃mc</i>			polar metal	10.1021/ic9515158
La ₁₅ Ge ₉ Ni	<i>P6₃mc</i>			polar metal	10.1021/ic9515158
Sr ₃ Cu ₈ Sn ₄	<i>P6₃mc</i>			polar metal	10.1016/j.intermet.2011.02.018
IrMg _{2.03} In _{.97}	<i>P6₃mc</i>			polar metal	10.1016/j.intermet.2003.12.001
IrMg _{2.20} In _{.80}	<i>P6₃mc</i>			polar metal	10.1016/j.intermet.2003.12.001
CaAlSi	<i>P6₃</i>	yes		polar metal	10.1143/JPSJ.75.043713
TlV ₆ S ₈	<i>P6₃</i>	yes		polar metal	10.1016/S0038-1098(01)00333-7
KV ₆ S ₈	<i>P6₃</i>	yes		polar metal	10.1016/S0038-1098(01)00333-7
RbV ₆ S ₈	<i>P6₃</i>	yes		polar metal	10.1016/S0038-1098(01)00333-7
CsV ₆ S ₈	<i>P6₃</i>	yes		polar metal	10.1016/S0038-1098(01)00333-7
LaPt ₃ B	<i>P4mm</i>		yes	polar metal	10.1016/S0925-8388(03)00373-6
PrPt ₃ B	<i>P4mm</i>		yes	polar metal	10.1016/S0925-8388(03)00373-6
NdPt ₃ B	<i>P4mm</i>		yes	polar metal	10.1016/S0925-8388(03)00373-6
LaRhSi ₃	<i>I4mm</i>	yes		polar metal	10.1016/0025-5408(84)90017-5
LaIrSi ₃	<i>I4mm</i>	yes		polar metal	10.1016/0025-5408(84)90017-5

CeCoGe ₃	<i>I4mm</i>	yes	yes	polar metal	10.1016/j.jmmm.2006.10.717
LaCoGe ₃	<i>I4mm</i>		yes	polar metal	10.1143/JPSJ.75.044711
CeRhGe ₃	<i>I4mm</i>	yes	yes	polar metal	10.1143/JPSJ.77.064716
CeRuSi ₃	<i>I4mm</i>			polar metal	10.1143/JPSJ.77.064716
LaIrGe ₃	<i>I4mm</i>			polar metal	10.1143/JPSJ.77.064717
LaFeGe ₃	<i>I4mm</i>			polar metal	10.1143/JPSJ.77.064717
PrCoGe ₃	<i>I4mm</i>			polar metal	10.1143/JPSJ.77.064717
CaIrSi ₃	<i>I4mm</i>	yes		polar metal	10.1016/j.physc.2009.10.120
CaPtSi ₃	<i>I4mm</i>	yes		polar metal	10.1134/S0021364010170157
SrAuSi ₃	<i>I4mm</i>	yes		polar metal	10.1021/cm500032u
EuPdGe ₃	<i>I4mm</i>		yes	polar metal	10.1016/j.ssc.2012.02.022
EuPtSi ₃	<i>I4mm</i>		yes	polar metal	10.1103/PhysRevB.81.144414
NdPdIn ₂	<i>I4mm</i>			polar metal	10.1021/cm031139m
SmPdIn ₂	<i>I4mm</i>			polar metal	10.1021/cm031139m
GdPdIn ₂	<i>I4mm</i>			polar metal	10.1021/cm031139m
ErPdIn ₂	<i>I4mm</i>			polar metal	10.1021/cm031139m
TmPdIn ₂	<i>I4mm</i>			polar metal	10.1021/cm031139m
LuPdIn ₂	<i>I4mm</i>			polar metal	10.1021/cm031139m
La ₂ NiAl ₇	<i>I4mm</i>			polar metal	10.1021/cm050513a
SnP	<i>I4mm</i>			polar metal	10.1021/ic50084a032
GeP	<i>I4mm</i>	yes		polar metal	10.1016/0022-4596(70)90005-8
Ir ₉ Al ₂₈	<i>P3₁c</i>			polar metal	10.1016/j.jallcom.2005.06.027
γ-Bi ₂ Pt	<i>P3₁m</i>			polar metal	10.1002/zaac.201400331
Au _{6.05} Zn _{12.51}	<i>P3₁m</i>			polar metal	10.1021/ic301933a
Ba ₂₁ Al ₄₀	<i>P3₁m</i>			polar metal	10.1021/ic0400235
Li ₁₇ Ag ₃ Sn ₆	<i>P3₁m</i>			polar metal	10.1021/ja038868n
Cr ₅ Al ₈	<i>R3m</i>			polar metal	10.1107/S0567740874004997
Mn ₅ Al ₈	<i>R3m</i>	yes		D polar metal	10.1007/BF02672582
Cu _{7.8} Al ₅	<i>R3m</i>			polar metal	10.1107/S0108768191005694
Cu ₇ Hg ₆	<i>R3m</i>			polar metal	10.3891/acta.chem.scand.23-1181
NbS ₂	<i>R3m</i>	yes		polar metal	10.1107/S0567740874003220
Pr ₂ Fe ₁₇	<i>R3m</i>		yes	polar metal	10.1103/PhysRevB.68.054424
Pr ₂ Co ₁₇	<i>R3m</i>			polar metal	10.1103/PhysRevB.68.054424
Sn ₄ As ₃	<i>R3m</i>	yes		polar metal	10.1002/zaac.19683630102

Sn ₄ P ₃	<i>R3m</i>		yes	polar metal	10.1002/zaac.19683630102
LiOsO ₃	<i>R3c</i>	yes		D polar metal	10.1038/NMAT3754 A
La ₄ Mg ₅ Ge ₆	<i>Cmc2₁</i>			polar metal	10.1021/ic2014732
La ₄ Mg ₇ Ge ₆	<i>Cmc2₁</i>			polar metal	10.1021/ic2014732
Yb ₂ Ga ₄ Ge ₆	<i>Cmc2₁</i>			polar metal	10.1002/chem.200305755
Ce ₂ Rh ₃ (Pb,Bi) ₅	<i>Cmc2₁</i>		yes	polar metal	10.1016/j.jssc.2007.06.012
Eu ₂ Pt ₃ Sn ₅	<i>Cmc2₁</i>		yes	polar metal	10.1524/zkri.2009.1160
Lu ₄ Zn ₅ Ge ₆	<i>Cmc2₁</i>			polar metal	10.1016/j.intermet.2013.02.018
Hg ₃ Te ₂ Br ₂	<i>R3</i>	yes		polar metal	10.1038/s41467-021-21836-7
In ₂ S ₃	<i>R3m</i>	P		A polar metal	arXiv:2102.11508 [cond-mat.mtrl-sci]
In ₂ Se ₃	<i>R3m</i>	P		A polar metal	arXiv:2102.11508 [cond-mat.mtrl-sci]
In ₂ Te ₃	<i>R3m</i>	P		A polar metal	arXiv:2102.11508 [cond-mat.mtrl-sci]
NaYMnReO ₃	<i>P2₁</i>	P	yes	polar metal	10.1021/acs.chemmater.0c02976
NaYFeReO ₃	<i>P2₁</i>	P	yes	polar metal	10.1021/acs.chemmater.0c02976
NaYCoReO ₃	<i>P2₁</i>	P	yes	polar metal	10.1021/acs.chemmater.0c02976
NaYNiReO ₃	<i>P2₁</i>	P	yes	polar metal	10.1021/acs.chemmater.0c02976
NaYMnOsO ₃	<i>P2₁</i>	P	yes	polar metal	10.1021/acs.chemmater.0c02976
NaYCoOsO ₃	<i>P2₁</i>	P	yes	polar metal	10.1021/acs.chemmater.0c02976
NaYNiOsO ₃	<i>P2₁</i>	P	yes	polar metal	10.1021/acs.chemmater.0c02976
NaYFeWO ₃	<i>P2₁</i>	P	yes	polar metal	10.1021/acs.chemmater.0c02976
YAl ₂	<i>P6mm</i>	P		A polar metal	10.1021/acs.jpcclett.0c03136
CaRh ₂	<i>P6mm</i>	P		A polar metal	10.1021/acs.jpcclett.0c03136
doped SiGe	<i>P3m1</i>	P		A polar metal	10.1088/1361-648X/abdce9/pdf
doped SiSn	<i>P3m1</i>	P		A polar metal	10.1088/1361-648X/abdce9/pdf
doped GeSn	<i>P3m1</i>	P		A polar metal	10.1088/1361-648X/abdce9/pdf
KNbO ₃ /BaTiO ₃	<i>P4mm</i>	P	yes	A polar metal	10.1016/j.commatsci.2020.110235
(SrRuO ₃) ₁ /(BaTiO ₃) ₁₀	<i>mm2*</i>		yes	A polar metal	10.1021/acs.nanolett.0c03417
strained EuTiO _{3-x} H _x	<i>Pmm2</i>	P	yes	E polar metal	10.1103/PhysRevB.102.224102
ATiO ₂ H (A=K, Rb, Cs)	<i>unknown</i>	P	yes	doped FE	10.1103/PhysRevMaterials.5.054802
doped PbZrO ₃	<i>unknown</i>	P		doped FE	10.1103/PhysRevB.102.134118
LaFeAsO _{1-x} H _x	<i>mm2*</i>		yes	yes polar metal	10.21203/rs.3.rs-77544/v1
Pb ₂ CoOsO ₆	<i>Pc</i>	yes	yes	D polar metal	10.1103/PhysRevB.102.144418
PrAlGe	<i>I4₁md</i>		yes	polar metal	10.1038/s41467-020-16879-1
doped PbTe monolayer	<i>P3m1</i>	P		E A polar metal	10.1039/d0nh00188k

en-CoS

*Pca2*₁

yes polar metal

10.1021/acs.chemmater.1c00540

Appendix B: Persistent polar distortions from covalent interactions in doped BaTiO₃

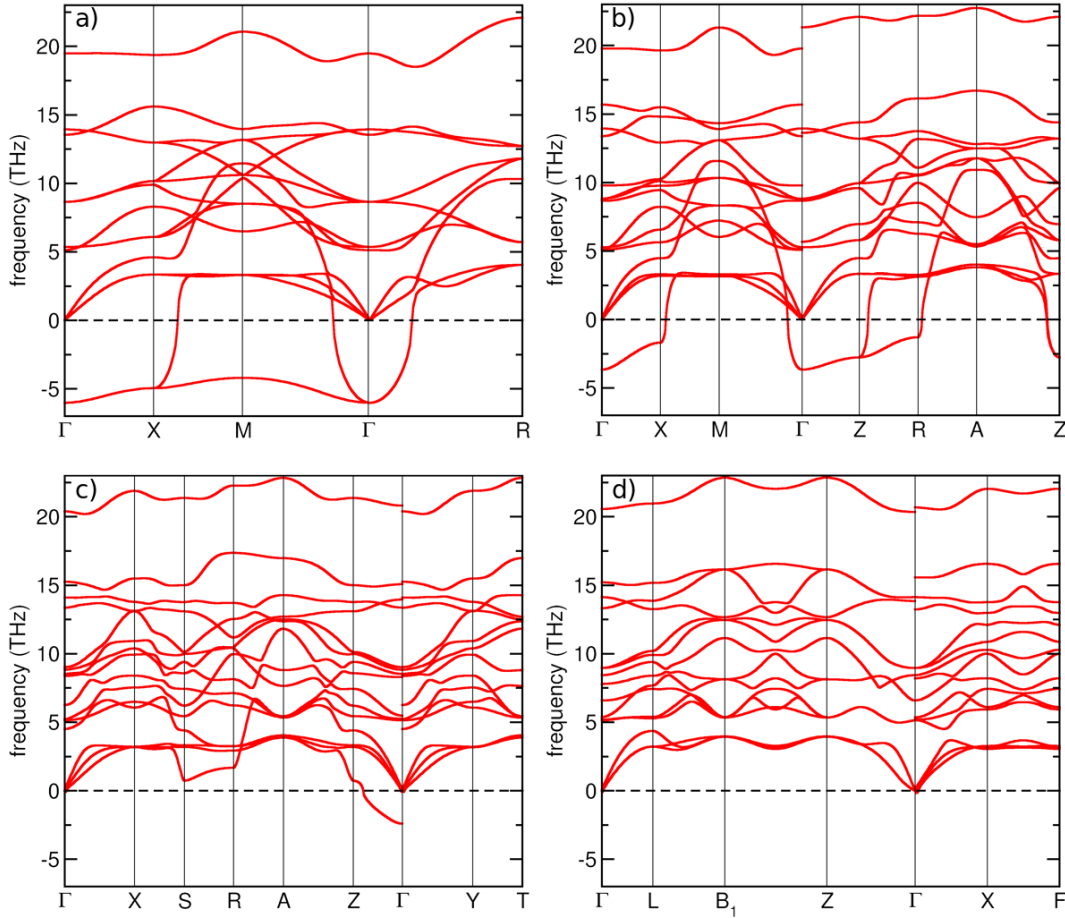


FIGURE B.1: Theoretical phonon dispersion curves for the different polymorphs of BaTiO_3 , after applying the non-analytical correction to account for LO-TO splitting. The panels are presented in order of appearance with decreasing temperature: (a) Cubic ($Pm\bar{3}m$) (b) tetragonal ($P4mm$) (c) orthorhombic ($Amm2$) and (d) rhombohedral ($R3m$). After each phase transition, the number of unstable phonon modes decreases. There are three unstable phonon modes in the cubic phase (at least two are always degenerate), two unstable modes in the tetragonal phase, followed by one in the orthorhombic phase and eventually none in the dynamically stable rhombohedral phase.

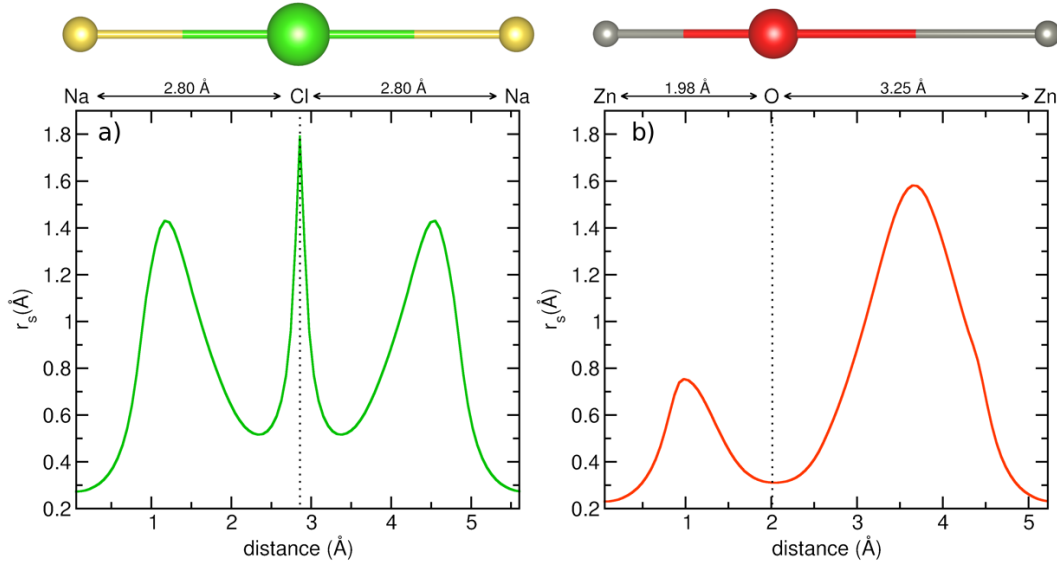


FIGURE B.2: Comparison of Wigner-Seitz radius (r_s) along representative bonds in (a) NaCl and (b) ZnO. The bond between Na and Cl (a) is predominantly ionic; the elements involved are best described as exhibiting a transfer rather than a sharing of electrons between ions. This is evident from the large peaks in r_s along the Na-Cl bond, indicative of a significant decrease in the charge density. The short bond between Zn and O (b), however, shows a reduced r_s peak, indicative of electron sharing within a covalent bond. The large peak corresponds to a non-bonding interaction between O and the Zn of the next unit cell. Note that the height of the non-bonding (tall) peak in ZnO is similar to that of the ionic bond in NaCl, whereas the height of the covalent-bonding (short) peak in ZnO is comparable to that of the peak between Ti and O in BaTiO₃ (see Fig. 3a in the main text). As mentioned in the main text, we find r_s to be preferable to charge density for the analysis of changes in bonding character. With charge density, the assignment of charge to a particular point or path in space is somewhat arbitrary. Contour plots avoid this assignment but as a result lead to more qualitative analysis. Wigner-Seitz radius, on the other hand, provides a well-defined quantitative method for examining charge density along paths in real space. It allows for clear comparison of materials with different bonding character (as shown above) and under different doping configurations (as shown in the manuscript). For these reasons, we believe r_s provides a useful qualitative description of bond character.

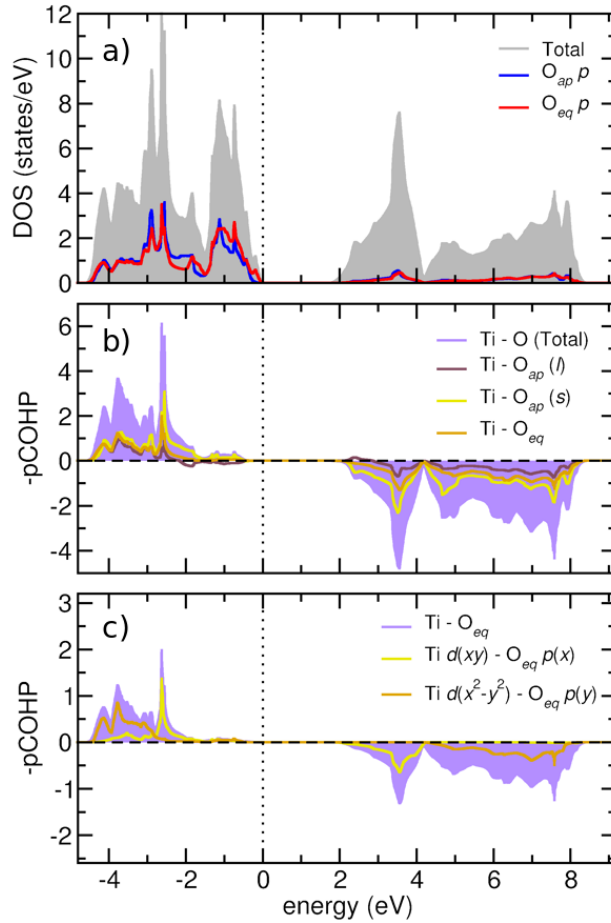


FIGURE B.3: (a) Electronic density of states (DOS) for tetragonal BaTiO_3 , with partial DOS projected showing the contributions from apical and equatorial oxygen atoms, respectively. Note that in each panel O_{eq} refers to the contribution from a single equatorial oxygen atom, not the combined contribution from the two symmetry-equivalent sites. Although the main text focuses primarily on the role of covalent bonding between Ti and O_{ap} , the Ti - O_{eq} interaction also affects the polar distortion. Panels (b) and (c) show the Crystal Orbital Hamilton Population (COHP) as projected onto (b) the three different Ti–O interactions (long/short Ti- O_{ap} and Ti- O_{eq}) as well as (c) the dominant orbital interactions between Ti and O_{eq} in particular. Note, only the contribution from a single Ti- O_{eq} interaction is shown, highlighting that while the combined Ti- O_{ap} degree of hybridization is certainly of greater magnitude than a single Ti- O_{eq} interaction, the combined effect of both equatorial oxygen sites will produce a comparable contribution.

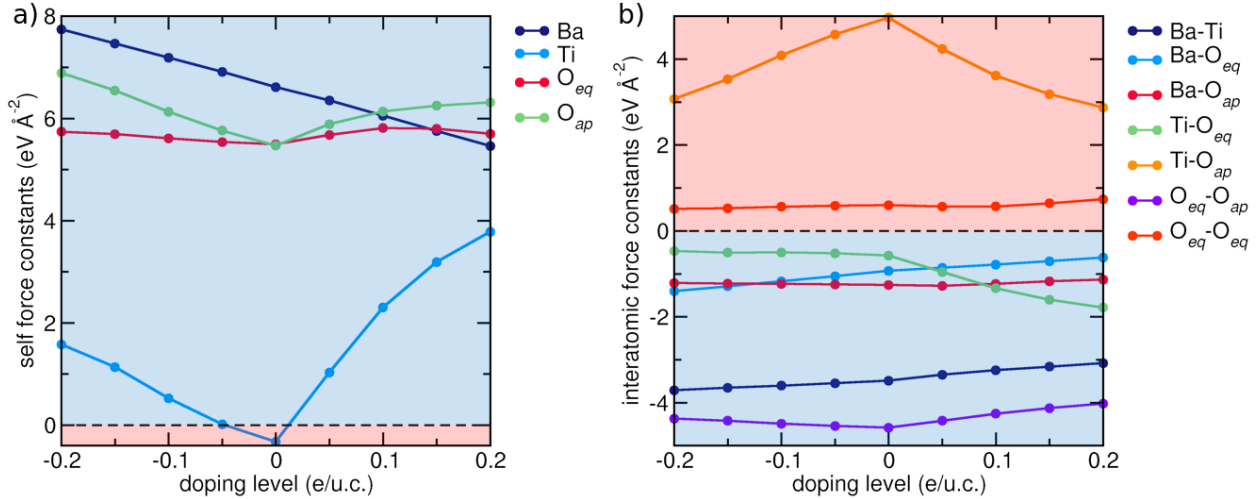


FIGURE B.4: Evolution of (a) self force constants (SFCs) and (b) interatomic force constants (IFCs) under electron and hole doping in fully relaxed cubic BaTiO₃. Red shading indicates the displacement is more energetically favorable, whereas blue shading indicates enhanced stability of the the high symmetry structure. These trends occur with opposite signs for SFCs and IFCs. However, it should be noted that neither SFCs nor IFCs explicitly describe the degree of bonding, nor does an unstable element of the force constant matrix necessarily imply that a polar distortion is favorable (that can only be determined by considering the full force constant matrix, from which a phonon dispersion can be derived). Despite these limitations, the force constants of BaTiO₃ provide insight into the relative strength of driving forces behind the polar distortion and illustrate a sign-dependent perturbation of the Ti-O bond strength under doping. As we might expect from the Slater mode displacement pattern, the most unstable SFC is Ti, while the most unstable IFC describes the relative motion of Ti and O_{ap} (apical O atom). Similarly, these are the elements most affected (both strongly stabilized) by electron doping. Hole doping also has a strong stabilizing effect but, as with our findings from the phonon mode analysis, the stabilization is more gradual than in the *n*-type case and the results are also impacted by volume relaxation. This behavior is clearly discernible for the Ti SFC. Meanwhile, the other SFCs and IFCs are both more stable and exhibit only modest changes with doping. These sites are not expected to contribute strongly based on the first principles prediction of the pattern of local off-centering reflected by the Slater mode. They are likewise expected not to be greatly affected by doping since the strength of their out-of-plane interaction does not involve electronic states near the Fermi level.

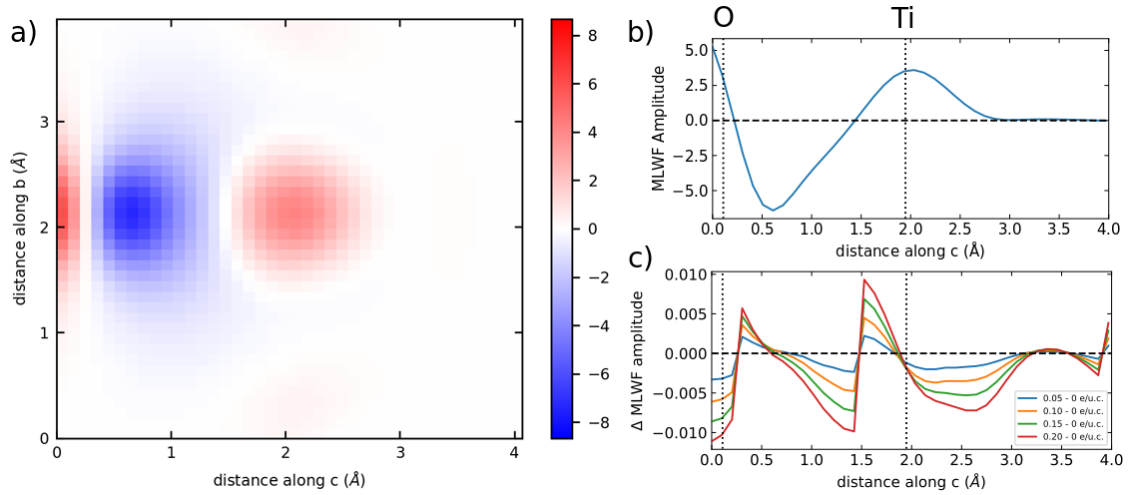


FIGURE B.5: (a) Two-dimensional slice of the MLWF associated with the $O_{ap-p}(z)$ orbital, taken perpendicular to the a axis so that it cuts through the Ti and apical oxygen bond. (b) MLWF amplitude along the apical Ti-O bond. (c) Change in MLWF amplitude as a function of electron doping taken along the same path through the apical Ti-O bond. Similar to the patterns seen for Ti- $d(z^2)$ in Fig. 8 of the main text, we see that electron doping appears to result in a net shift of the orbital lobes away from Ti and towards O.

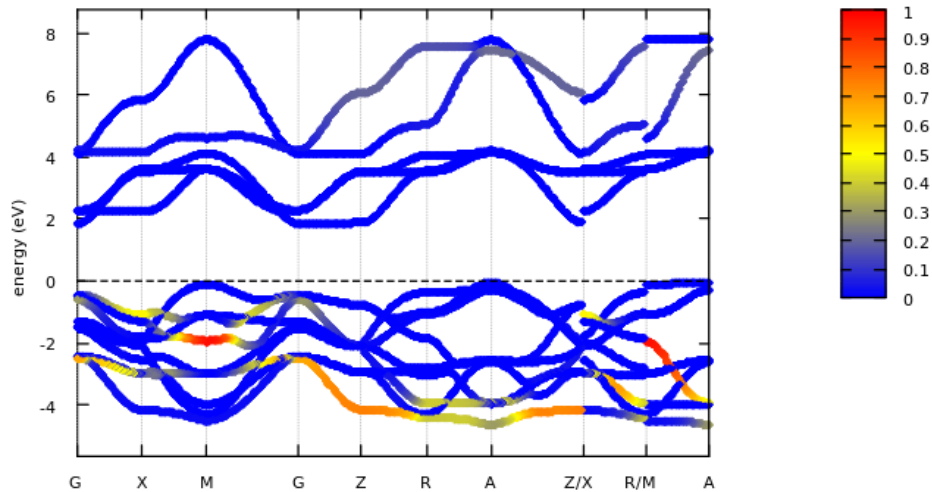


FIGURE B.6: Electronic band structure for undoped tetragonal ($P4mm$) BaTiO_3 , highlighting the projection of the maximally localized Wannier function (MLWF) associated with the $\text{O}_{ap-p}(z)$ orbital. Although the vast majority of bands with $\text{O}_{ap-p}(z)$ character are located in the valence band, some of the states traditionally associated with the $\text{Ti-}d(e_g)$ orbitals exhibit non-negligible $\text{O}_{ap-p}(z)$, evidence of the hybridization (bonding state) between Ti and O_{ap} . To generate the Wannier function projection data for Fig. 7 in the main text, we integrated the projection of $\text{O}_{ap-p}(z)$ onto the $\text{Ti-}d(e_g)$ states (as shown here) at each doping level.

Appendix C: Transforming a strain-stabilized ferroelectric into an intrinsic polar metal via photodoping

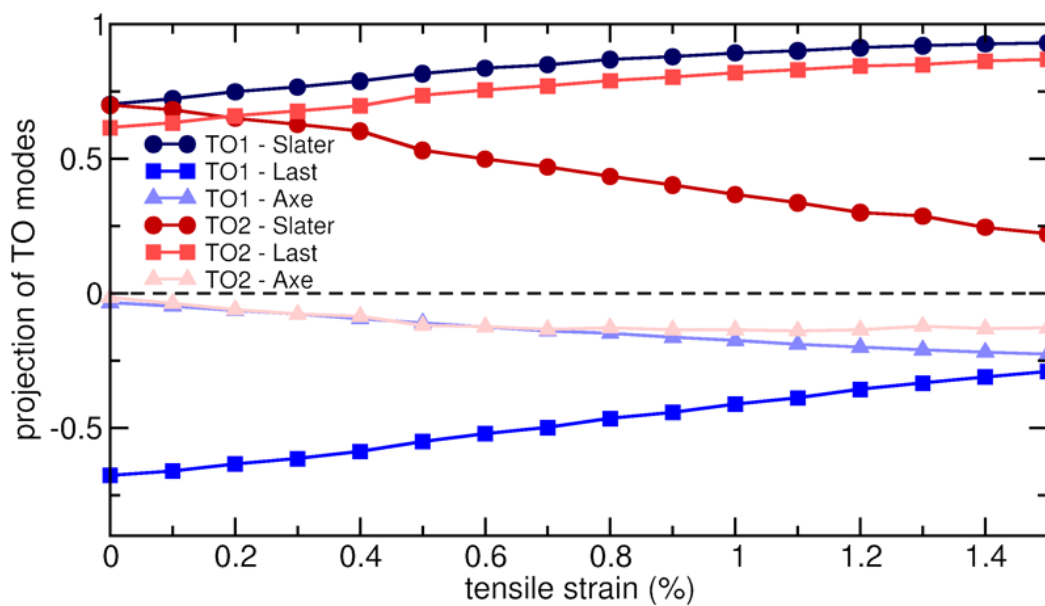


FIGURE C.1: Mode character projections were performed at each strain level by performing a dot product of the calculated eigendisplacement vector (mass-reduced and normalized) with the canonical perovskite displacement patterns from [4].

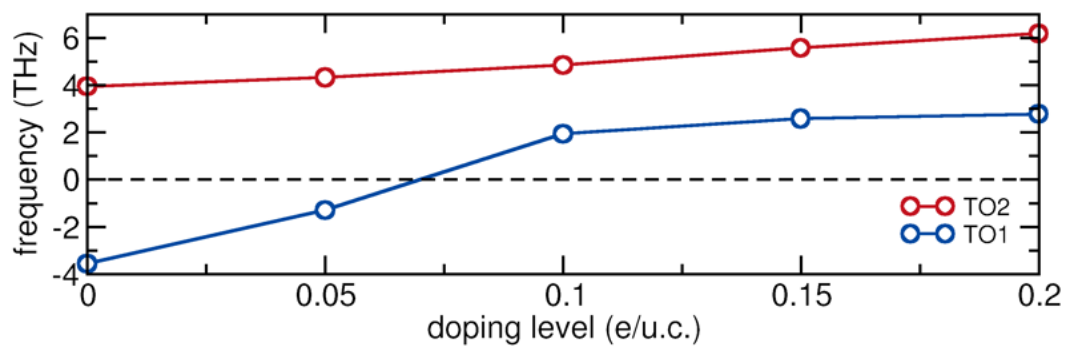


FIGURE C.2: The two lowest-lying Γ -centered transverse optical modes for high symmetry $P4/mmm$ EuTiO_3 at 1.5% strain under added electrons compensated by a neutralizing background charge (i.e. no hole generation).

Appendix D: Designing an anti-Ruddlesden-Popper polar metal

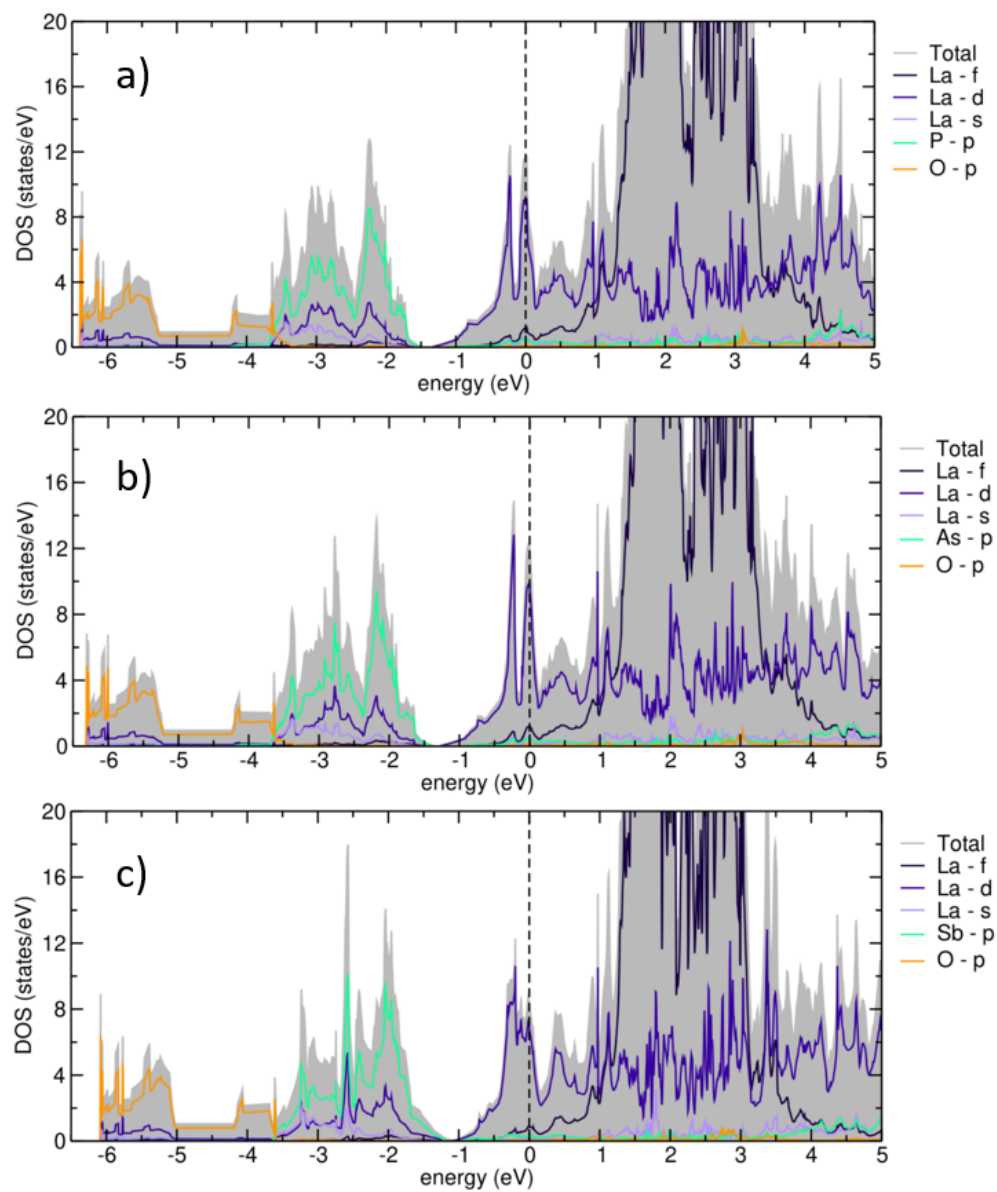


FIGURE D.1: Projected density of states for the $I4/mmm$ phase of (a) $\text{La}_4\text{P}_2\text{O}$ (b) $\text{La}_4\text{As}_2\text{O}$ and (c) $\text{La}_4\text{Sb}_2\text{O}$.

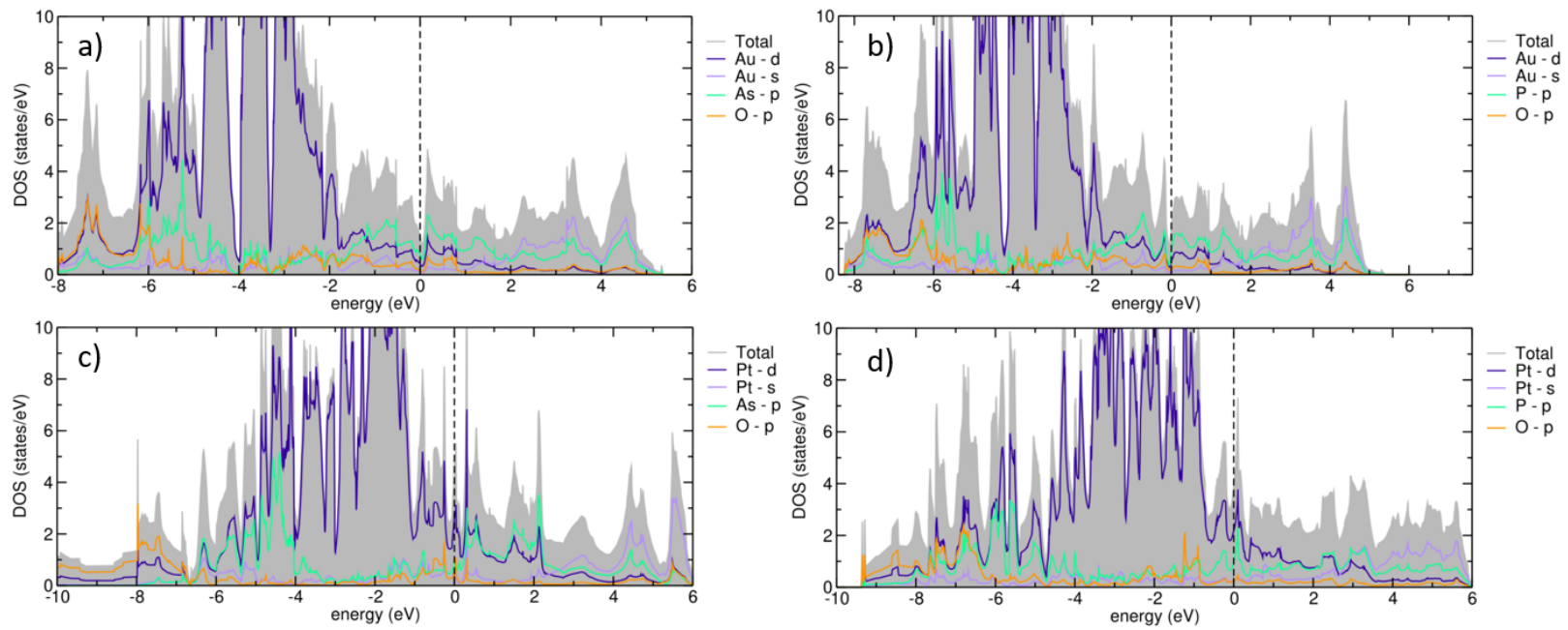


FIGURE D.2: Projected density of states for the $I4/mmm$ phase of (a) $\text{Au}_4\text{As}_2\text{O}$ (b) $\text{Au}_4\text{P}_2\text{O}$ (c) $\text{Pt}_4\text{As}_2\text{O}$ and (d) $\text{Pt}_4\text{P}_2\text{O}$.

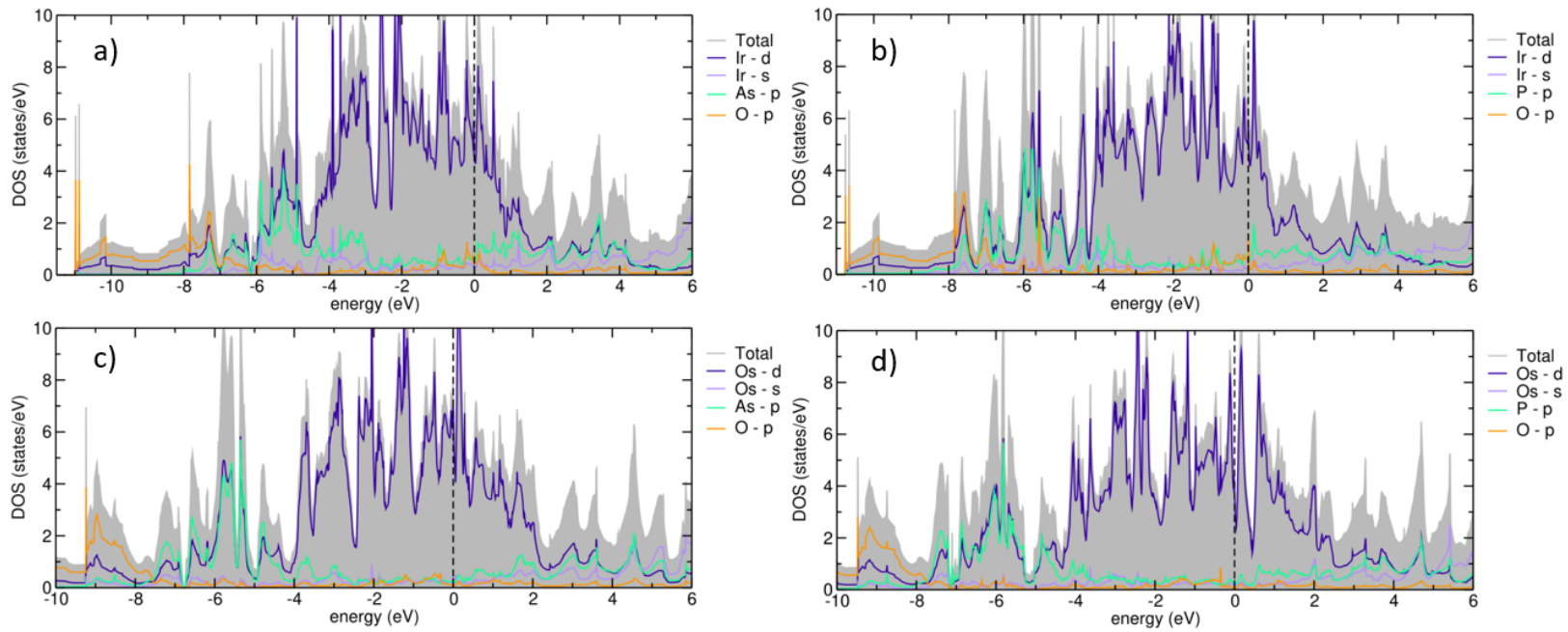


FIGURE D.3: Projected density of states for the $I4/mmm$ phase of (a) $\text{Ir}_4\text{As}_2\text{O}$ (b) $\text{Ir}_4\text{P}_2\text{O}$ (c) $\text{Os}_4\text{As}_2\text{O}$ and (d) $\text{Os}_4\text{P}_2\text{O}$.

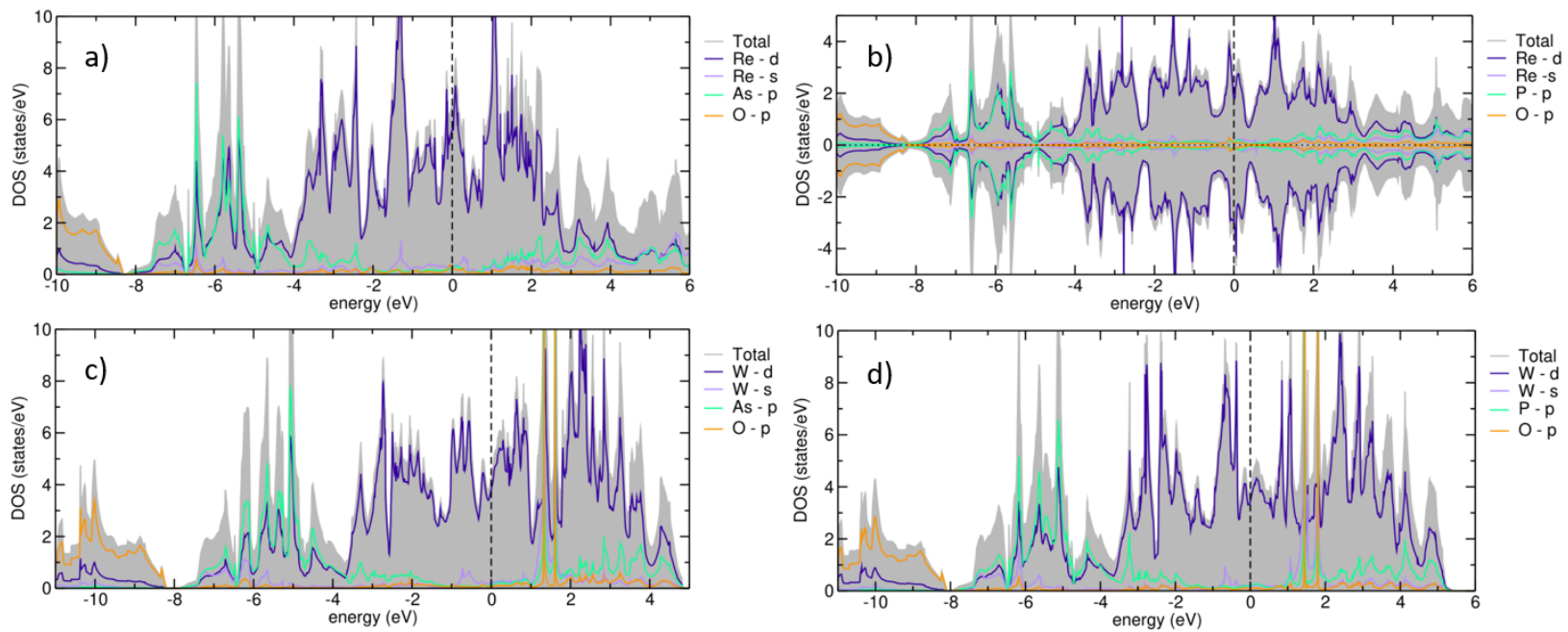


FIGURE D.4: Projected density of states for the $I4/mmm$ phase of (a) $\text{Re}_4\text{As}_2\text{O}$ (b) $\text{Re}_4\text{P}_2\text{O}$ (c) $\text{W}_4\text{As}_2\text{O}$ and (d) $\text{W}_4\text{P}_2\text{O}$.

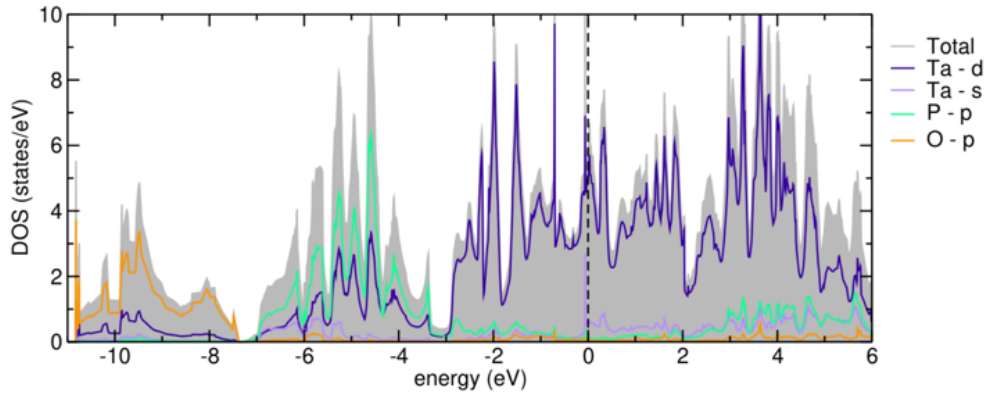


FIGURE D.5: Projected density of states for the $I4/mmm$ phase of $\text{Ta}_4\text{P}_2\text{O}$.

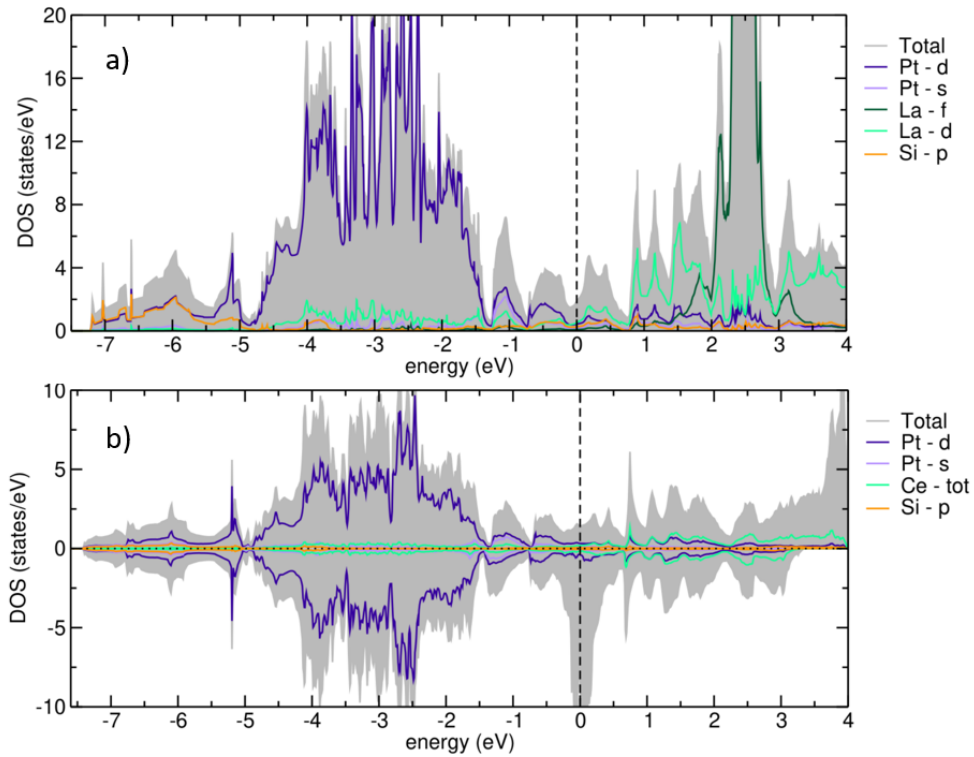


FIGURE D.6: Projected density of states for the $I4/mmm$ phase of (a) $\text{Pt}_4\text{La}_2\text{Si}$ and (b) $\text{Pt}_4\text{Ce}_2\text{Si}$. Ce f states are not shown because VASP struggles to project f states accurately. f orbitals in other PDOS plots are projected using LOBSTER. However, this requires running a DFT calculation with no symmetry, under which conditions the $\text{Pt}_4\text{Ce}_2\text{Si}$ simulation struggles to converge. However, the total DOS near E_F can reasonably be expected to be dominated by Ce f states.

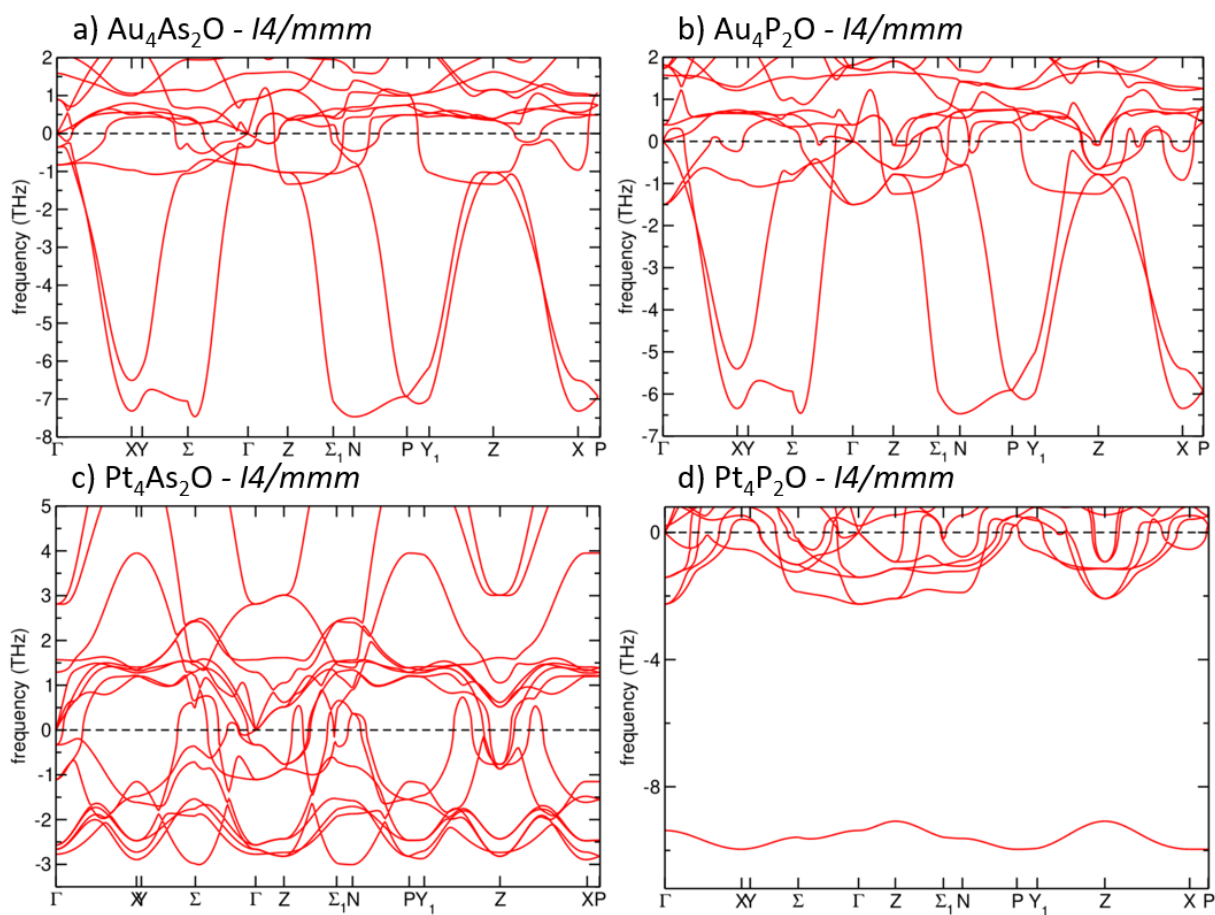


FIGURE D.7: Phonon dispersions as calculated for $I4/mmm$ (a) $\text{Au}_4\text{As}_2\text{O}$ (b) $\text{Au}_4\text{P}_2\text{O}$ (c) $\text{Pt}_4\text{As}_2\text{O}$ and (d) $\text{Pt}_4\text{P}_2\text{O}$

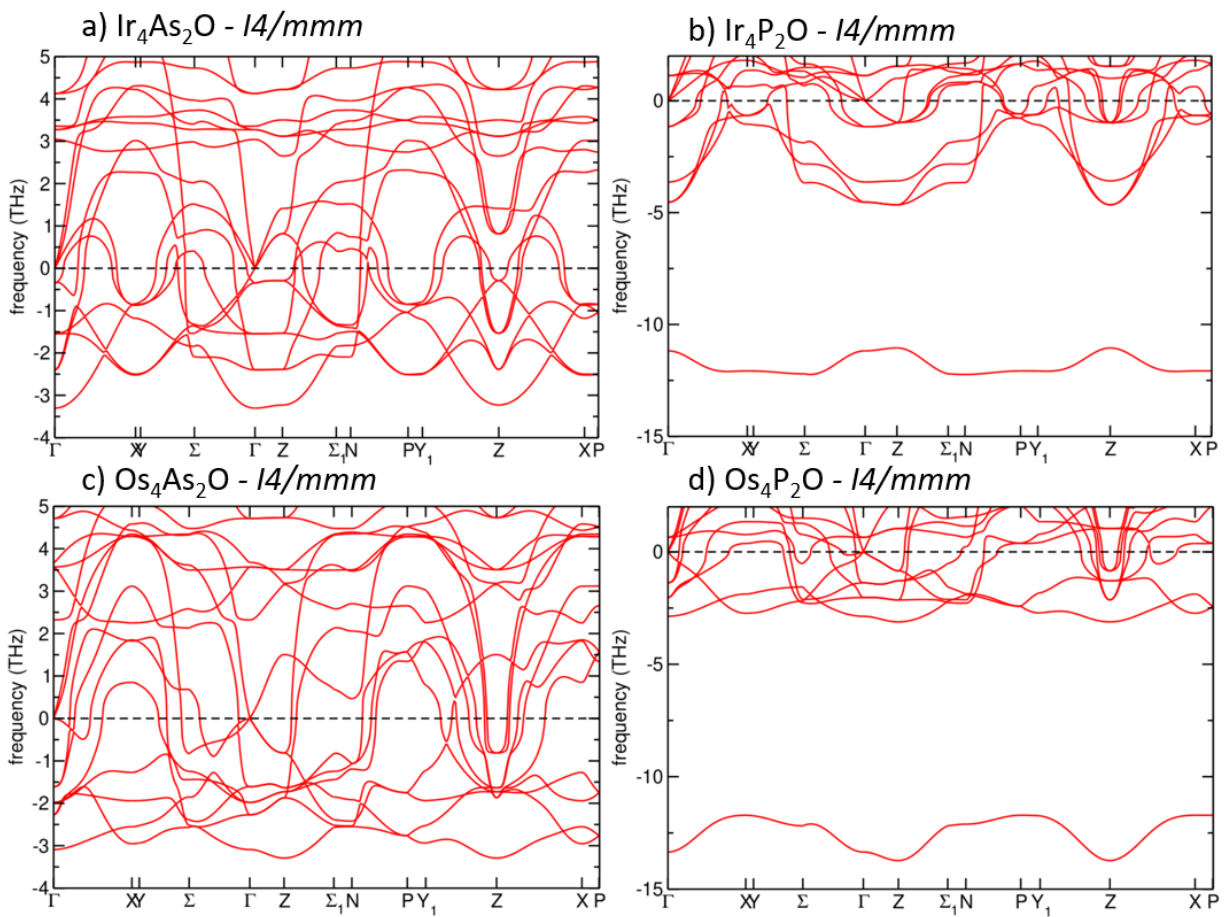


FIGURE D.8: Phonon dispersions as calculated for $I4/mmm$ (a) Ir_4As_2O (b) Ir_4P_2O (c) Os_4As_2O and (d) Os_4P_2O

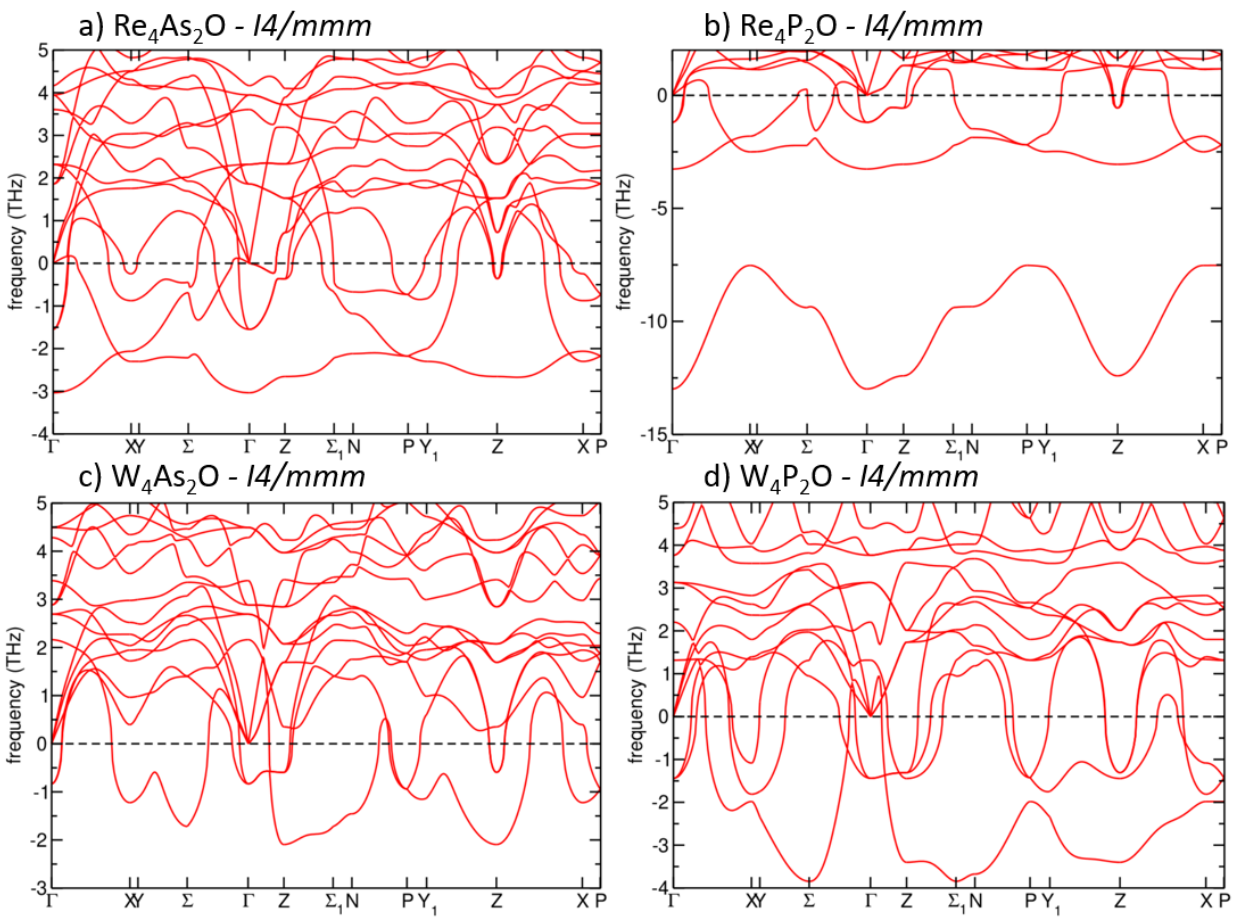


FIGURE D.9: Phonon dispersions as calculated for $I4/mmm$ (a) $\text{Re}_4\text{As}_2\text{O}$ (b) $\text{Re}_4\text{P}_2\text{O}$ (c) $\text{W}_4\text{As}_2\text{O}$ and (d) $\text{W}_4\text{P}_2\text{O}$

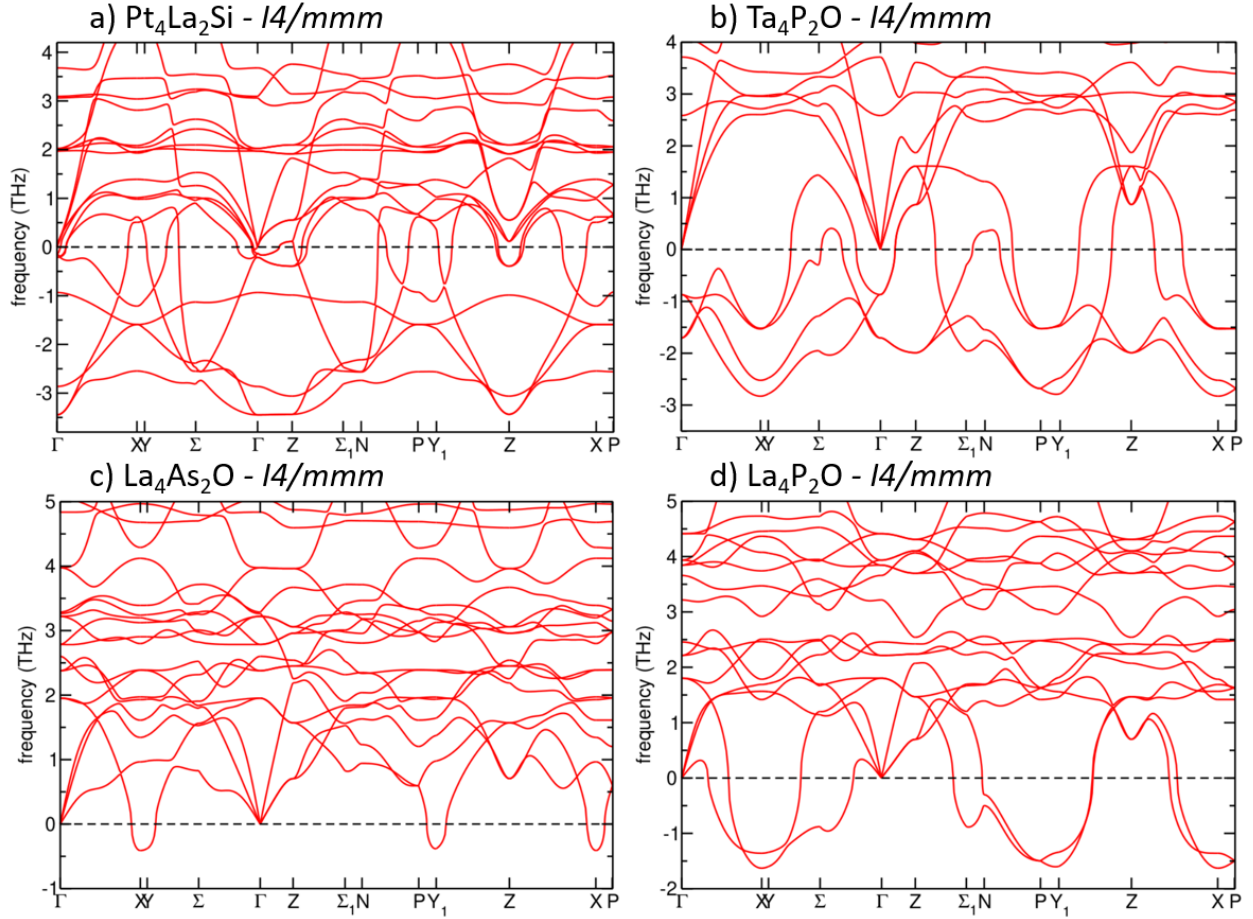


FIGURE D.10: Phonon dispersions as calculated for $I4/mmm$ (a) Pt_4La_2Si (b) Ta_4P_2O (c) La_4As_2O and (d) La_4P_2O . Phonon dispersion for Pt_4Ce_2Si is not included, due to challenges converging simulations of the low-symmetry structural modulations required for the frozen-phonon method. However, structural relaxations in candidate ground state space groups were successfully performed, identifying $Ama2$ as the likely ground state structure.

Vita

Publications before PhD

1. S. Bittner, C. Lafargue, I. Gozhyk, N. Djellali, L. Milliet, **D. T. Hickox-Young**, C. Ulysse, D. Bouche, R. Dubertrand, E. Bogomolny, J. Zyss, M. Lebental. Origin of emission from square-shaped organic microlasers. *Europhys. Lett.* 118 (2016) 54002. [doi]

Publications during PhD

1. G. Laurita, **D. Hickox-Young**, S. Husremovic, J. Li, A. W. Sleight, R. Macaluso, J. M. Rondinelli, M. A. Subramanian. Covalency-driven Structural Evolution in the Polar Pyrochlore Series $\text{Cd}_2\text{Nb}_2\text{O}_{7-x}\text{S}_x$. *Chem. Mater.* 31, 18 (2019) 7626–7637. [doi]
2. G. Laurita, D. Puggioni, **D. Hickox-Young**, J. M. Rondinelli, M. W. Gaultois, K. Page, L. K. Lamontagne, R. Seshadri. Uncorrelated Bi off-centering and the insulator-to-metal transition in ruthenium $\text{A}_2\text{Ru}_2\text{O}_7$ pyrochlores. *Phys. Rev. Materials.* 3 (2019) 095003. [doi]
3. **D. Hickox-Young**, D. Puggioni, J. M. Rondinelli. Persistent polar distortions from covalent interactions in doped BaTiO_3 . *Phys. Rev. B.* 102, 1 (2020) 014108. [doi]
4. H. Zheng, B. C. Wilfong, **D. Hickox-Young**, J. M. Rondinelli, P. Y. Zavalij, E. E. Rodriguez. Polar Ferromagnetic Metal by Intercalation of Metal–Amine Complexes. *Chem. Mater.* 33, 13 (2021) 4936–4947. [doi]
5. Q. N. Meier, **D. Hickox-Young**, G. Laurita, N. A. Spaldin, J. M. Rondinelli, M. R. Norman. Leggett Modes Accompanying Crystallographic Phase Transitions. *arXiv:2107.11332 [cond-mat.mtrl-sci]* (2021)